Super-long single-molecule tracking reveals dynamic-anchorage-induced integrin function

（超長時間１分子追跡法の開発による

インテグリンの動的接着機構の解明）

角山　貴昭

Super-long single-molecule tracking reveals dynamic-anchorage-induced integrin function

Taka A. Tsunoyama [1], Yusuke Watanabe[2], Junri Goto[2], Kazuma Naito[2], Rinshi S. Kasai[3], Kenichi G. N. Suzuki[2,4], Takahiro K. Fujiwara[2] and Akihiro Kusumi[1,2,3]*

Single-fluorescent-molecule imaging tracking (SMT) is becoming an important tool to study living cells. However, photobleaching and photoblinking (hereafter referred to as photobleaching/photoblinking) of the probe molecules strongly hamper SMT studies of living cells, making it difficult to observe in vivo molecular events and to evaluate their lifetimes (e.g., off rates). The methods used to suppress photobleaching/photoblinking in vitro are difficult to apply to living cells because of their toxicities. Here using 13 organic fluorophores we found that, by combining low concentrations of dissolved oxygen with a reducing-plus-oxidizing system, photobleaching/photoblinking could be strongly suppressed with only minor effects on cells, which enabled SMT for as long as 12,000 frames (~7 min at video rate, as compared to the general 10-s-order durations) with ~22-nm single-molecule localization precisions. SMT of integrins revealed that they underwent temporary (<80-s) immobilizations within the focal adhesion region, which were responsible for the mechanical linkage of the actin cytoskeleton to the extracellular matrix.

Fluorescence microscopy is extensively used in biomedical research with living cells. In particular, SMT of fluorescent molecules at work in living cells is now providing researchers with the unprecedented ability to directly observe molecular dynamics and interactions. However, SMT and fluorescence microscopy are greatly hampered by photobleaching/photoblinking of the fluorescent probe molecules[1–6]. For example, the durations of molecular events, such as transient immobilizations, could in principle be directly measured by SMT; however, photobleaching/photoblinking make such measurements quite difficult.

Numerous methods have been devised to reduce photobleaching/photoblinking, including deoxygenation[7,8], the addition of reducing reagents and the addition of both reducing and oxidizing reagents, which is referred to as the reducing-plus-oxidizing system (ROXS)[9,10] (Supplementary Fig. 1); however, these methods are generally quite difficult to apply to living cells because of their toxicity. Therefore, here our aim was to develop (i) a method to suppress photobleaching/photoblinking of fluorescent organic molecules and (ii) a theory to determine the lifetimes of molecular events by SMT in the presence of photobleaching/photoblinking during the limited observation period (Supplementary Fig. 2). The method developed, super-long imaging-tracking of single individual molecules, was applied to investigate how β_1 and β_3 integrins, which are transmembrane receptors for the extracellular matrix (ECM) in focal adhesions (FAs), mechanically link the ECM and actin filaments in the cytoplasm, at the level of single molecules.

Results

ROXS and lower oxygen concentrations used in this research. The photobleaching rates of nine fluorescent organic compounds, as well as four organic fluorophores that were conjugated to the synthetic antioxidant trolox, were examined at the single-molecule level at 37 °C in living cells. Each of these was covalently linked to a tag protein (acyl carrier protein (ACP) or Halo) that was fused to the five-path transmembrane protein CD47 at its N-terminal

extracellular domain or its C-terminal cytoplasmic domain (only for the Halo-tagged protein) and was expressed in the plasma membrane (PM) of T24 human epithelial cells.

Molecular oxygen is completely removed in many photobleaching- and photoblinking-suppression methods. However, here we optimized the concentration of molecular oxygen, as molecular oxygen is essential for cell survival and might be useful for shortening the triplet-state lifetime (see Supplementary Fig. 3 and the Methods for the method used to control or measure the concentrations of dissolved oxygen in the medium). In the following part of this report, we describe the molecular oxygen concentrations in the cell culture medium as the percentages (partial pressure) of the molecular oxygen in the equilibrating gas mixture when its pressure was 760 mm Hg, and we express them in the manner '2%O$_2$' (no space between % and O$_2$) to indicate that the partial oxygen pressure was normalized to that under the 760 mm Hg atmosphere.

At the same time, we used ROXS. ROXS induces the transitions of fluorescent molecules in the triplet state to the ground state by way of the ion states by consecutive reduction (oxidation) and oxidation (reduction) reactions, thus effectively suppressing photobleaching/photoblinking (Supplementary Fig. 1). We used the less toxic compounds trolox, a vitamin E derivative, as a reducer and troloxquinone, a trolox derivative, as an oxidizer[11] at a fixed total concentration of 1 mM. The ROXS conditions used throughout are described as TX (1 mM trolox), TQ20 (0.8 mM trolox + 0.2 mM troloxquinone) and TQ40 (0.6 mM trolox + 0.4 mM troloxquinone) (Supplementary Fig. 4). The 'control' experiments were always performed in the absence of ROXS under 21%O$_2$.

ROXS + lower oxygen concentrations improves photostability. First, we describe the results obtained with tetramethylrhodamine (TMR) and SeTau647 (ST647), as these resulted in the largest improvements among the membrane-permeable and membrane-impermeable dyes, respectively. TMR and ST647 were conjugated to
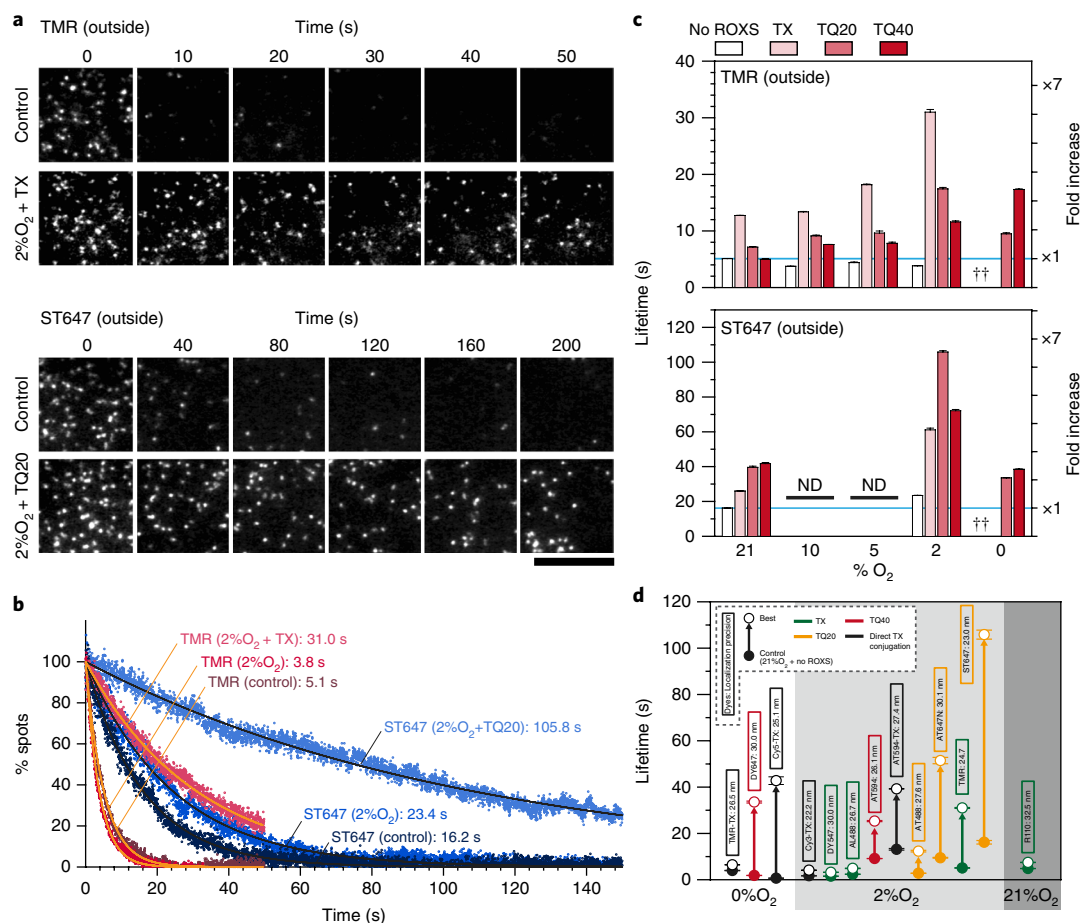
Fig. 1 | Photobleaching lifetimes in single-fluorescent-molecule imaging are prolonged under the conditions of low O2+ROXS. a, Representative total internal reflection fluorescence (TIRF) microscopic images (among six independent experiments) of a time series for TMR bound to Halo-CD47 (top) and ST647 bound to ACP-CD47 (bottom) (fluorophores located on the outer surface of a T24 epithelial cell). Note that the time scale for ST647 is lengthened by a factor of 4 from that for TMR. Scale bar, 10 µm. **b**, Time-dependent reductions of the numbers of fluorescence spots found in each 33-ms frame for TMR and ST647 on the extracellular surface (for the number of points, n, see Supplementary Table 1). Orange and black curves represent the best-fit single-exponential functions for TMR and ST647, respectively. The exponential decay time constants are shown in the figure. **c**, The photobleaching lifetime (exponential decay time constant) obtained by fitting with a single exponential function (Methods) under various %O2 and ROXS conditions for TMR (top) and ST647 (bottom) located outside the cell. Data are means ± s.e.m. (for the number of points, n, see Supplementary Table 1). A dagger symbol indicates that we were unable to determine these values owing to extensive blinking, which provided trajectories mostly as short as 1 or 2 frames (33 and 66 ms) that could not be distinguished from the noise signal. ND, not done. **d**, Summary of photobleaching lifetimes (exponential decay time constants) under control conditions and conditions for the slowest photobleaching (see Supplementary Table 1 for a comprehensive list, including the numbers of examined fluorescence spots and the degree of freedom for curve fitting; also see Supplementary Fig. 7). Most dyes exhibited the longest photobleaching time at 2%O2, but some dyes did so at 0%O2 and only the R110 dye exhibited the best performance under the control conditions (21%O2), with various ROXS conditions. All dyes were located on the outer surface of the cell. Data are means ± s.e.m.

Halo-CD47 and ACP-CD47, respectively (the comparison between Halo and ACP will be discussed later).

Typical time series analyses of single-molecule images of TMR and ST647 (Fig. 1a and Supplementary Videos 1 and 2) indicated that, when the ROXS and oxygen concentrations were adjusted, photobleaching could be greatly suppressed. The number of fluorescence spots found in each video frame plotted against time could be fitted by single-exponential functions (Fig. 1b and Supplementary Fig. 5). The exponential lifetimes evaluated under various O2+ ROXS conditions (at the same excitation laser power) are summarized in Fig. 1c (number counting photobleaching lifetime, which is almost the same as the lifetime evaluated by the bulk intensity measurements). In the case of TMR (or ST647), under the optimal conditions of 2%O2+TX (2%O2+TQ20 for ST647), the photobleaching lifetime was prolonged up to 31.0 s (105.8 s for ST647), an increase in the lifetime by a factor of 6.1 (6.5 for ST647), at

single-molecule localization precisions of 24.7 nm (control) and 25.8 nm (2%O2+TX) (23.0 nm (control) and 21.5 nm (2%O2+TQ20) for ST647) (Supplementary Fig. 6a–c (in which the signal intensities largely remained the same)). The photobleaching lifetime, fluorescence intensity and single-molecule localization precisions obtained under the control and optimized conditions are summarized in Table 1 (see also Supplementary Fig. 7 and Supplementary Table 1 (in which an extensive summary is provided)). Note that, for ease of the experiment, we kept the excitation laser intensity the same for the same dye molecule and that when we report the photobleaching lifetime we always specify the single-molecule localization precisions (21.5–32.5 nm, depending on the dye).

TMR attached to CD47-Halo, where the Halo-tagged protein is located in the cytoplasm, showed photobleaching lifetimes and signal intensities very similar to those of TMR bound to Halo-CD47 in the extracellular space (Supplementary Fig. 8). These results indicate

Table 1 | Photobleaching lifetimes using single-molecule imaging

Tag dye	Outside or inside the cell	Live or fixed cells	O$_2$ (%)	ROXS	Photobleaching lifetime (s) (by number counting)[a]	Relative prolongation (fold)[a]	Tracking lifetime (s)[b]	Relative intensity (fold)[c]	Localization precision (nm)
Halo-TMR	Outside	Live	21	–	5.1 ± 0.03	1.0 ± 0.01	–	1.0 ± 0.02	24.7
			21	TX	12.7 ± 0.04	2.5 ± 0.02	–	1.0 ± 0.01	–
			2	TX	31.0 ± 0.47	6.1 ± 0.10	–	0.9 ± 0.01	25.8
			0	TX	NA[d]		–	NA[d]	–
Halo-TMR	Outside	Fixed	21	–	4.6 ± 0.11	1.0 ± 0.03	4.3 ± 0.1	1.0 ± 0.01	24.7
			21	TX	12.2 ± 0.27	2.6 ± 0.05	10.7 ± 0.3	1.0 ± 0.01	–
			2	TX	29.1 ± 0.50	6.3 ± 0.19	23.7 ± 0.7	0.9 ± 0.01	25.8
			0	TX	NA[d]		0.9 ± 0.1	NA[d]	–
Halo-TMR	Inside	Live	21	–	5.3 ± 0.02	1.0 ± 0.01	–	1.0 ± 0.01	24.7
			21	TX	6.5 ± 0.09	1.4 ± 0.02		1.0 ± 0.01	–
			2	TX	32.4 ± 0.37	7.0 ± 0.08	–	0.9 ± 0.02	27.0
			0	TX	NA[d]		–	NA[d]	–
ACP-ST647	Outside	Live	21	–	16.2 ± 0.06	1.0 ± 0.01	–	1.0 ± 0.02	23.0
			21	TQ20	39.6 ± 0.69	2.4 ± 0.04	–	1.1 ± 0.03	–
			2	TQ20	105.8 ± 0.78	6.5 ± 0.05	–	1.4 ± 0.01	21.5
			0	TQ20	33.5 ± 0.12	2.1 ± 0.01	–	1.3 ± 0.01	–
ACP-ST647	Outside	Fixed	21	–	15.5 ± 0.11	1.0 ± 0.01	10.9 ± 0.2	1.0 ± 0.01	23.0
			21	TQ20	42.1 ± 0.66	2.7 ± 0.05	38.4 ± 1.3	1.1 ± 0.01	–
			2	TQ20	99.0 ± 1.57	6.4 ± 0.11	83.4 ± 2.1	1.4 ± 0.01	21.5
			0	TQ20	47.2 ± 1.30	3.0 ± 0.09	30.9 ± 0.8	1.3 ± 0.02	–

Photobleaching lifetimes obtained by counting the number of fluorescence spots in each image (number counting lifetime) and those obtained by tracking each individual molecule (tracking lifetime, which is affected by photoblinking) of TMR and ST647 under representative oxygen and ROXS conditions using single-molecule imaging are shown. For the number of points for estimation of the photobleaching lifetime by number counting, see Supplementary Table 1. [a]Exponential-decay time constant (means ± s.e.m.) (Methods). [b]Exponential-decay time constant (means ± s.e.m.). Single molecules blink, and therefore the duration from the initiation of the observation until the beginning of the first dark period for each molecule was measured. The determination of the single-molecule tracking lifetime was performed for only fixed cells for which CD47 was immobilized on the cell surface, to avoid possible complexity due to intermixing of blinking with other tracking problems. The numbers of molecules examined (in fixed cells, for the estimation of single-molecule tracking lifetimes) were as follows: 1,209, 988, 2,446, and 313 for TMR under control conditions, 21%O$_2$+TX, 2%O$_2$+TX, and 0%O$_2$+TX, and 750, 1,603, 1,884, and 1,741 for ST647 under control conditions, 21%O$_2$+TQ20, 2%O$_2$+TQ20, and 0%O$_2$+TQ20, respectively. [c]The modes ± s.e.m. obtained from the log-normal fitting (see the legend to Supplementary Fig. 6b). [d]NA, not analyzed owing to extensive blinking ('bright' periods generally lasting <66 ms; Methods).

that the reductive conditions in the cytoplasm (due to the presence of glutathione) did not affect photobleaching and ROXS efficacy. They also suggest that trolox and troloxquinone are membrane permeable.

The photobleaching lifetime of TMR-ACP-CD47 was shorter by a factor of ~3, as compared with that of TMR-Halo-CD47, and only a slight improvement was found after treatment with 2%O$_2$+TX. The reason for this difference is unknown. Meanwhile, when the membrane-impermeable dyes ATTO594 (AT594) and ST647 were conjugated to ACP-CD47 or Halo-CD47, the photobleaching lifetimes of the dyes bound to the ACP and Halo proteins were about the same (Supplementary Fig. 9 and Supplementary Table 1).

Single ST647 molecules can be imaged for ~3,200 frames. Among the 13 organic fluorescent compounds examined in this study (Fig. 1d), ST647 under optimal conditions (2%O$_2$+TQ20) exhibited the best photobleaching performance, with the exponential lifetime prolonged to 105.8 s from 16.2 s (6.5-fold difference; ~3,200 frames) at a single-molecule localization precision of 21.5 nm (Fig. 1d and Supplementary Fig. 6a). Note that, owing to rapid photoblinking, the photobleaching lifetimes of ST647 could not be properly determined with 0%O$_2$+TX or in the absence of ROXS. Rapid photoblinking was also observed with TMR under the same conditions (Methods). These conditions might be useful for direct stochastic optical reconstruction (dSTORM)-type observations.

Low O$_2$ + ROXS strongly suppresses photoblinking. Photoblinking is another serious problem in SMT. To avoid erroneous intermixing

of blinking with other tracking problems, cells were fixed to immobilize CD47 on the cell surface. The fluorescence intensities of fixed single molecules as a function of time exhibited a single-step transition to a non-fluorescent state, due to either photobleaching or photoblinking (Supplementary Fig. 10). We measured the duration from observation initiation by turning on the excitation laser until the first transition to the dark state for each molecule, and after observing many single molecules we obtained the histogram for 'bright'-state durations (Fig. 2a). This histogram might be close to the on-time distributions, but it is more relevant to actual experiments conducted using live cells, as it provides the distribution of the lengths of single-molecule trajectories observed from time 0.

We found that the distributions could operationally be fitted by single-exponential functions ('single-molecule tracking lifetime'). Under the optimal conditions shown in Fig. 1b, the decay lifetimes were 23.7 s for TMR under 2%O$_2$+TX and 83.4 s for ST647 under 2%O$_2$+TQ20. These values are 10–20% shorter than the bulk photobleaching lifetimes (Fig. 2b,c and Table 1), probably owing to photoblinking. Nevertheless, under these conditions, single molecules of TMR and ST647 could be tracked longer than previously reported.

When TMR-Halo-CD47 was observed at higher camera frame rates of up to 10 kHz (Supplementary Fig. 11), with higher laser excitation conditions to provide similar single-molecule localization precisions, photoblinking was observed in the recordings at a 10-kHz frame rate. However, the dark periods lasted for 0.22 and 0.26 ms, in contrast to the 18 and 59 ms of the bright 'on' periods (exponential lifetimes; control and 2%O$_2$+TX conditions, respectively), suggesting
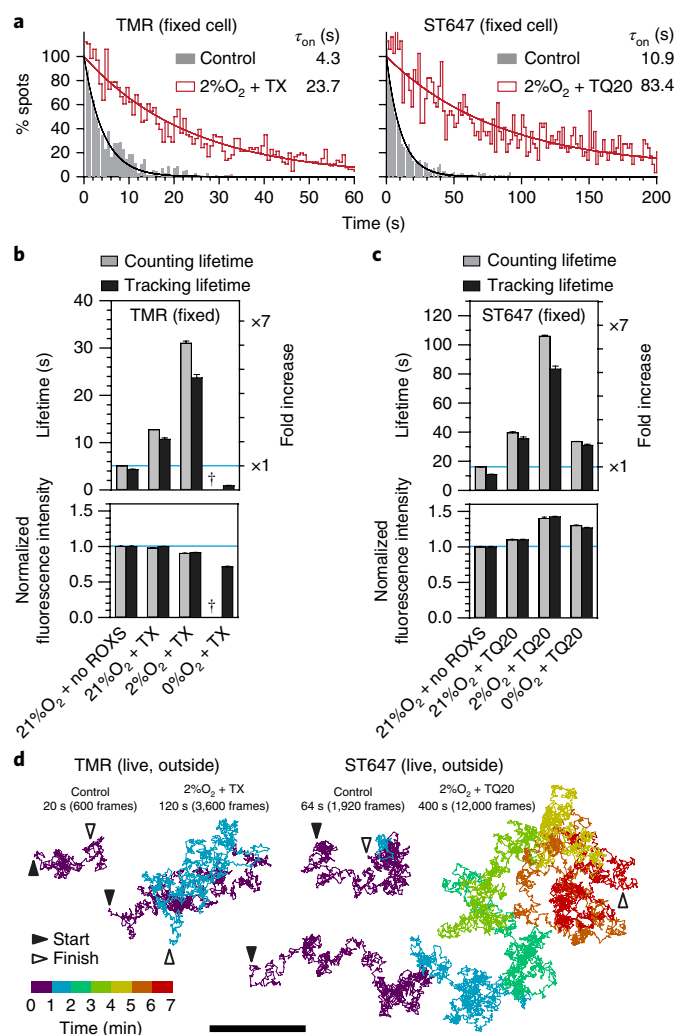
Fig. 2 | Photoblinking, in addition to photobleaching, can be suppressed under the optimal conditions of low oxygen concentrations+ROXS, as observed by single-fluorescent-molecule tracking at video rate. a, The distributions of bright-state durations of single TMR bound to Halo-CD47 (left) and ST647 bound to ACP-CD47 (right) molecules in fixed cells, observed at video rate, registered from time 0 of laser excitation and recording. Because single-molecule tracking ended at the moment the photoblinking (transition to the dark state) occurred, the lifetimes found by this method were shorter than those determined by counting the number of spots in each frame (Fig. 1a,b). The best-fit single-exponential curves are shown. The numbers of molecules examined are summarized in Table 1 (footnote b). **b,c**, Summary of photobleaching lifetimes obtained either by counting the number of fluorescence spots (counting lifetime) or from the duration distributions of single-molecule trajectories (tracking lifetime) (exponential-decay time constant) (means ± s.e.m.), as well as the fluorescence intensities (modes ± s.e.m. obtained by log-normal fitting; Supplementary Fig. 6b). A dagger symbol indicates that we were unable to measure these values owing to extensive blinking. For *n* values, see Table 1 (footnote b) and Supplementary Table 1. **d**, Typical trajectories for TMR and ST647 molecules linked to CD47 in the live cell PM that could be tracked without photoblinking and photobleaching for periods longer than 120 and 400 s (~4× lifetimes shown in Table 1, and thus representative among a few percent of molecules). Note the differences in the lengths of the trajectories obtained in the ambient atmosphere (control) versus those under the optimized conditions. Scale bar, 10 μm.

that such photoblinking will not strongly affect the observations at frame rates up to ~300 Hz (3.3-ms integration time > 10 × 0.26 ms).

In optimal cases, we found that single CD47 molecules could be tracked for 2 and 6.7 min at video rate using TMR and ST647, respectively, under their optimal conditions (Fig. 2d). Such long-term single-molecule observations would be extremely useful for studies of molecular interactions.

Strong cytotoxicity occurs at 0%O_2 but not at 2%O_2. First, under conditions with 2%O_2, T24, HeLa, CHO-K1 and NIH3T3 cells grew well. Their doubling times were comparable to those under the 5%O_2 and 21%O_2 conditions (Fig. 3a and Supplementary Fig. 12), consistent with previous observations[12].

Second, the effect of low oxygen concentrations on cell survival was examined in the microscope observation medium (Hank's balanced salt solution (HBSS) buffered with 2 mM *N*-Tris(hydroxymethyl)methyl-2-aminoethanesulfonic acid (TES, pH 7.4); hereafter referred to as T-HBSS) at 37 °C (Fig. 3b,c and Supplementary Fig. 13). At 2%O_2, almost all of the cells survived; however, at 0%O_2, the half-lives of the cells were only ~3.5 h.

Third, the influence of low oxygen concentrations on cellular activities was investigated by monitoring cell spreading. The time course of cell spreading was observed using β_1 integrin–deficient mouse embryonic fibroblasts (*Itgb1*-knockout MEFs; hereafter referred to as β_1-KO MEFs)[13] that had not or had been transfected with *Itgb1* (hereafter referred to as β_1-transfected MEFs; Fig. 3d and Supplementary Fig. 14a). The β_1-transfected MEFs spread faster than the β_1-KO MEFs, by a factor of ~2.5. The extent of cell spreading at 2%O_2 was almost the same as that at 21%O_2; however, at 0%O_2, it was diminished by 30–40% (statistically significantly), which was clear even at 15 min (observed for up to 90 min; Fig. 1d).

Fourth, the diffusion coefficients of CD47-mGFP in T24 and HeLa cells remained the same at 2%O_2; however, at 0%O_2 (even for 15 min), the diffusion coefficients in HeLa cells were greatly increased (although those in T24 cells were unaffected), consistent with the previous result[14] (Fig. 3e and Supplementary Figs. 15 and 16). According to our proposed picket-fence model[15], the increases in the diffusion coefficients found here are consistent with subtle depolymerization of the actin membrane skeleton.

Therefore, we conclude that for studies of living cells 0%O_2 should not be used and that 2%O_2 is quite suitable or even better than 21%O_2, consistent with previous observations[12,16]. Cells still thrive at lower oxygen concentrations, perhaps because of less peroxidation and/or the expression of hypoxia-inducible factor[17]. Indeed, the oxygen concentrations in animal tissues are generally much lower than 21%O_2[18–20].

Cytotoxicity of ROXS. Under the conditions of 2%O_2+ROXS, unlike that at 0%O_2, the reduction in the number of live T24 and HeLa cells became detectable only after 5, 6 and 7 h of incubation in the presence of TQ40, TQ20 and TX, respectively (Fig. 3b,c and Supplementary Fig. 13), and the diffusion coefficient of CD47-mGFP in the PM of these cells remained the same for 120 min (the longest incubation time used; Fig. 3e and Supplementary Figs. 15 and 16), indicating that ROXS did not change the physical properties of the PM during this period (however, see ref. [21]).

Similarly, under the conditions of 2%O_2+ROXS, unlike that at 0%O_2, the spreading of β_1-KO MEFs and β_1-transfected MEFs remained basically the same as under control conditions for 90 min (the longest incubation time used) (Fig. 3d and Supplementary Fig. 14a). Because our fluorescence observations were finished mostly within 15 min of the addition of ROXS (at 2%O_2), its toxic effect on our observations was predicted to be limited.

Comparison with dye molecules directly conjugated to trolox. Previously, other groups directly linked triplet-state quenchers (TSQs; such as cyclooctatetraene, 4-nitrobenzyl alcohol or trolox (TX)) to cyanine dyes and found that the photostabilities of the
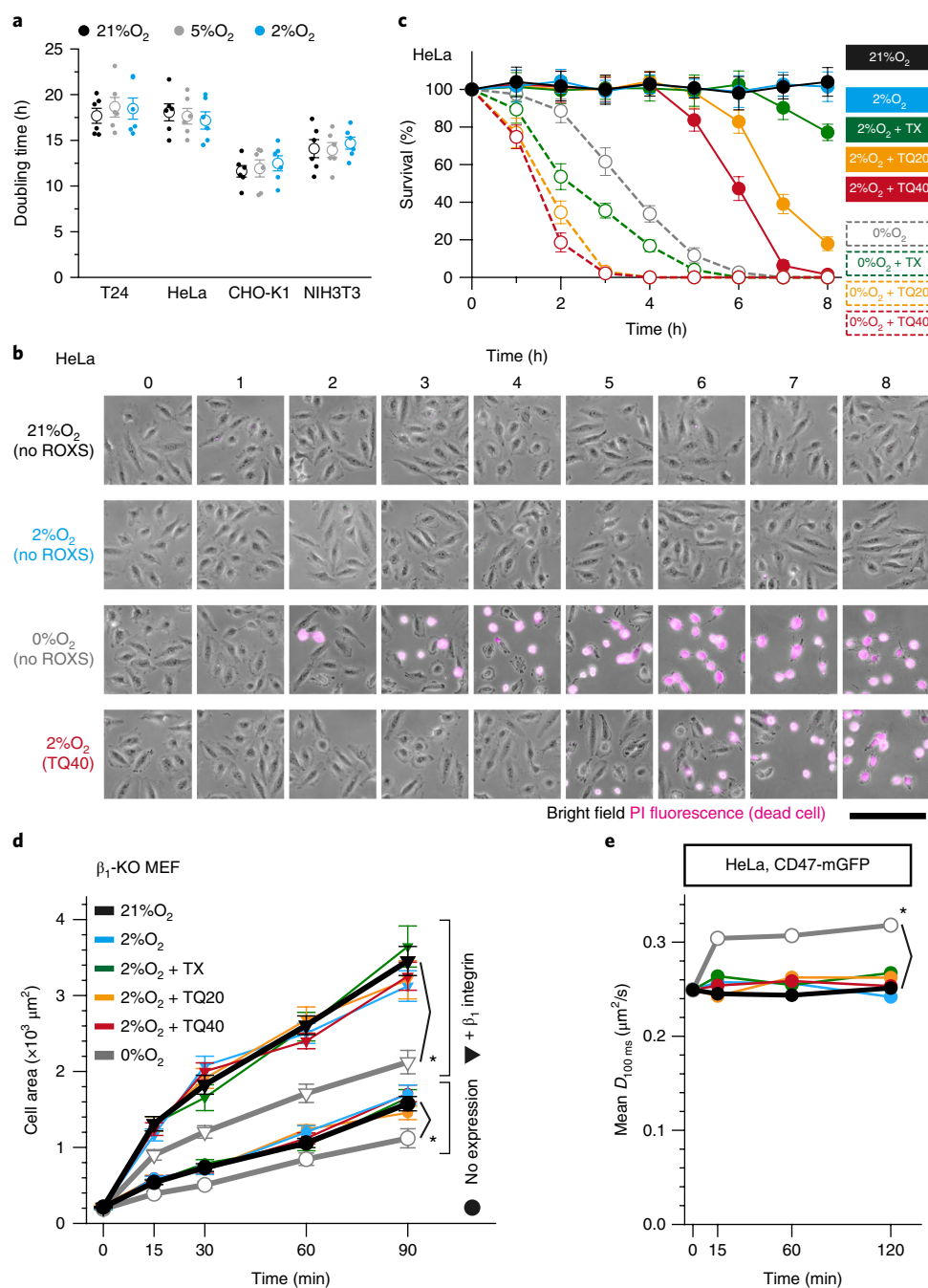
Fig. 3 | No cytotoxicity under 2%O$_2$, slight toxicity after ROXS addition, in marked contrast to the toxicity of 0%O$_2$. a, Cellular doubling times at 2%O$_2$, 5%O$_2$ or 21%O$_2$, determined for T24, HeLa, CHO-K1 and NIH3T3 cells. Data are means ± s.e.m. of $n = 6$ independent experiments. No significant differences were found at low oxygen concentrations using a two-sided Welch's *t* test (*P* values for 21%O$_2$ versus 5%O$_2$ and for 21%O$_2$ versus 2%O$_2$, respectively): T24, $P = 0.51$ and $P = 0.59$; HeLa, $P = 0.51$ and $P = 0.59$; CHO-K1, $P = 0.78$ and $P = 0.42$; NIH3T3, $P = 0.91$ and $P = 0.63$. For raw data, see Supplementary Fig. 12. **b**, Representative (among six independent experiments) phase-contrast micrographs of HeLa cells superimposed by their propidium iodide (PI)-stained fluorescence images (pink), recorded for 8 h under various conditions. Scale bar, 200 µm. **c**, Percentages of surviving HeLa cells, under various low-oxygen+ROXS conditions, as determined by the trypan blue exclusion assay ($n = 6$ independent experiments). Data are means ± s.e.m. **d**, Spreading of β$_1$-KO MEFs (± β$_1$ integrin expression) after plating on fibronectin (FN)-coated glass-base dishes (Supplementary Fig. 14a). Data are the mean cell areas ± s.e.m. of $n = 20$ cells. 2%O$_2$+ROXS incubation did not significantly alter the results for up to 90 min. *$P < 0.05$ by two-sided Mann–Whitney *U* test (for actual *P* values, see Supplementary Table 5). **e**, Mean diffusion coefficients of CD47-mGFP in HeLa cells, plotted against the incubation times under various conditions (distributions shown in Supplementary Fig. 16). See Supplementary Fig. 16 for *n* values. 2%O$_2$+ROXS treatment did not significantly alter the diffusion coefficients for up to 120 min. *$P < 0.05$ by two-sided Mann–Whitney *U* test (actual *P* values are shown in Supplementary Fig. 16). In d and e, statistically significant changes were found only at 0%O$_2$ (relative to the control conditions), even for an incubation time of 15 min at 0%O$_2$.

cyanine dyes were greatly improved as compared to the photostabilities observed when the TSQs were added to the solution, particularly under 0%O_2[1,2,4,6]. Here we performed similar experiments by synthesizing TMR-TX-Halo and AT594-TX-CoA, as well as Cy3-TX-Halo and Cy5-TX-Halo, which were examined previously (Supplementary Fig. 17; single-molecule localization precisions of 21.7–28.7 nm in the x and y directions).

TMR-TX did not show any improved photostability under all of the O_2 concentrations used here, whereas AT594-TX exhibited ~1.6-fold better photostabilities at 0%O_2 and 2%O_2 than with AT594 at 2%O_2+TQ40 (optimized conditions for AT594) (Supplementary Figs. 18 and 19). The extents of TX-induced photostability were large for Cy5-TX and small for Cy3-TX, in general agreement with the data reported previously[2] (Supplementary Figs. 18 and 19).

Among the dyes conjugated with TSQ, Cy5-TX exhibited the slowest photobleaching, with a lifetime of 44.8 s at 0%O_2 (with a single-molecule localization precision of 26.7 nm; Supplementary Table 1 and Supplementary Video 3). This indicates that ST647, under the optimized conditions of 2%O_2+TQ20 (with a 21.5-nm localization precision), photobleached more slowly than Cy5-TX under the optimized conditions of 0%O_2 (unfavorable conditions for live cells), by a factor of 2.2.

Super-long single-molecule tracking of integrins. ACP–β_1 integrin exhibited the ability to enhance cell spreading as much as the native β_1 integrin (Supplementary Fig. 14), and thus it was considered to be functional. Therefore, ST647-ACP–β_1 integrin was observed at the single-molecule level at video rate, together with the FA marker mGFP-paxillin, at 2%O_2+TQ20 (the optimal conditions for ST647). The mGFP-paxillin domains were classified by area size—either smaller or larger than 0.25 μm². The former might include the often called nascent adhesions or focal complexes[22,23] (Supplementary Fig. 20).

Single ACP-tagged β_1 and β_3 integrin molecules entered and exited from FAs and repeatedly exhibited temporary immobilizations, which are referred to as 'temporary arrest of lateral diffusion' (TALL), both inside and outside the FA (Fig. 4a, Supplementary Fig. 21 and Supplementary Videos 4 and 5; also see ref. [24]).

In subsequent experiments, we mostly dealt with the larger FAs because integrin behaviors could be observed much more clearly. Every time integrin molecules exhibited TALL, the TALL duration was measured (here the TALL durations included those for TALL events that ended by either movement or the photobleaching of the molecule). The TALL time fractions against the entire trajectory length inside and outside the FA were, respectively, 78% and 51% for ACP–β_1 integrin, or 83% and 40% for ACP–β_3 integrin (Fig. 4b). Namely, inside the FA, integrin molecules can diffuse but are immobilized about ~80% of the time. Even outside the FA, they underwent TALL half of the time, suggesting that integrins probably have important functions even outside the FA (Fig. 4b).

Theory for obtaining the correct TALL lifetime. After observing many TALL events, we obtained a histogram of TALL durations (Supplementary Figs. 22 and 23). To analyze the distribution of TALL duration, we developed a theory to evaluate the correct TALL lifetime from the experimentally obtained TALL duration distributions, which are skewed by photobleaching of probe molecules and limited observation (recording) durations (T_{rec}). Note that, in single-molecule observations, the time window for observing a molecular event is not uniform; rather, each individual molecule provides a different time window by stochastically following a single-exponential photobleaching lifetime distribution (as shown earlier in this study). Furthermore, the limited length of the observation duration (T_{rec}) affects the experimental raw data of the TALL duration distribution because a TALL event can be truncated by the initial and final ends of the observation period (Supplementary Fig. 37 in

Supplementary Note 1). Therefore, we developed a theory for obtaining the correct TALL duration distribution from the raw distribution directly obtained by experiments. This theory will be applicable for obtaining the lifetimes of many single-molecule events.

The detailed theory is provided in Supplementary Note 1. In the present integrin experiments, we selected a T_{rec} of 200 s, so that it would minimally affect the results, knowing that the optimized (minimized) photobleaching rate for ST647 is 1/83.5 (with 2%O_2+TQ20). Under these conditions, the duration distribution of TALL events corrected for photobleaching, in the presence of more than one independent immobile state, $n = 1, 2,…, n_I$, and a single mobile state, $G_{fit}^{nI}(\delta)$, would be given by

$$G_{fit}^{nI}(\delta) = \sum_{n=1}^{n_I} A_n exp[- (k_B + k_{M,n}) \cdot \delta] \quad (1)$$

where A_n represents a complex function of the rate constants for state n but can practically be determined, as the fitting parameters $k_{M,n}$ is the rate constant for the transition from the immobile state n to the mobile state (defined as $1/\tau_n$, where τ_n is the TALL lifetime for the immobile state n) and k_B is the photobleaching lifetime common to all of the states (defined as $1/\tau_B$, where τ_B is the photobleaching lifetime).

Three types of TALLs occur both inside and outside the FA. The histogram for TALL duration of β_1 integrin could be fitted by the sum of three exponential-decay functions (see equation (1)), based on both Akaike's and Bayesian information criteria (Supplementary Tables 2 and 3), with decay time constants (lifetimes) of $\tau_1 = 0.51$ (6% time fraction in the total TALL duration and 68% in terms of the number fraction), $\tau_2 = 4.3$ (12% and 16%, respectively), and $\tau_3 = 43$ s (82% and 16%, respectively) inside the FA, after the correction for photobleaching (Fig. 4b, Supplementary Figs. 22 and 24a, and Supplementary Table 2). β_3 integrin exhibited similar TALL behaviors, except that the lifetime of the longest TALL fraction (τ_3 TALL fraction) was longer (79 s) than that for β_1 integrin (43 s) (Fig. 4b and Supplementary Figs. 22 and 24a).

The majority of TALLs, in terms of the number of events, occurred with the shortest lifetime ($\tau_1 \leq 0.51$ and 0.66 s; 68% and 50% for β_1 and β_3 integrin, respectively; Supplementary Fig. 24a). However, the majority of TALLs, in terms of the time fraction (relative to the sum of all TALL durations), were explained by the relatively small numbers of longest TALL (τ_3) events (Fig. 4b). Notably, there were very few molecules that were immobile much longer than the τ_3 lifetimes of 43 and 79 s for β_1 and β_3 integrin, respectively (Supplementary Table 4; see Supplementary Note 1 for the evaluation method), indicating that these three TALL components could describe virtually all of the TALL events that occurred in the FA region. Notably, the addition of Mn^{2+}, an integrin activator[25], only slightly affected the TALL behaviors of β_1 integrin, but its effect on the TALL behaviors of β_3 integrin was much greater; the τ_3 lifetime was prolonged, and the time fraction of the longest τ_3 component was increased (Fig. 4b and Supplementary Figs. 22 and 24a).

TALLs were induced by the binding of integrins to ECM–actin filaments. The dynamic behaviors of three β_1 integrin mutant proteins, β_1-D130A (no RGD binding), β_1-Y783A/Y795A (mutations in the cytoplasmic domain with no binding to talin, tensin, filamin and kindlin, and thus no linkage to actin filaments) and β_1-D130A/Y783A/Y795A (the combination of the extracellular and intracellular mutations) (the products of $ITGB1^{D130A}$, $ITGB1^{Y783A/Y795A}$, and $ITGB1^{D130A/Y783A/Y795A}$, respectively) were investigated in HeLa cells (see the cell spreading results in Supplementary Fig. 25)[26,27]. β_1-D130A and β_1-Y783A/Y795A exhibited no longest-lifetime (τ_3) TALL component, but exhibited the middle-lifetime (τ_2) component
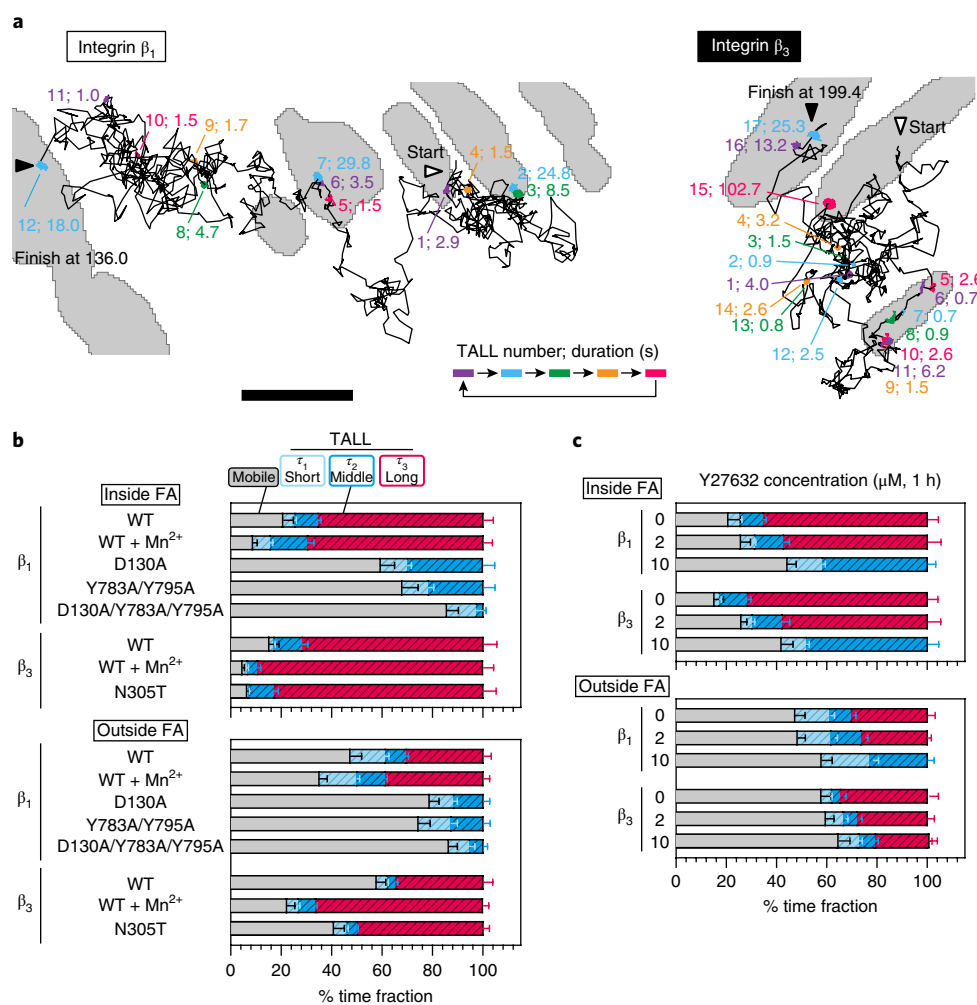
Fig. 4 | Both β₁ and β₃ integrin undergo repeated TALLs, often lasting for 43 and 79 s, respectively, due to binding both the extracellular matrix and actin filaments. a, Typical trajectories of ST647-ACP–β₁ integrin (left) and ACP–β₃ integrin (right) at 2%O₂+TQ20 (among 1,729 and 2,714 trajectories, respectively). The FA zone was visualized by mGFP-paxillin (binarized gray areas). TALLs are shown in color; in each set of numbers shown, the first number indicates the order of occurrences and the second number indicates the TALL duration (s). Scale bar, 2 μm. **b,c**, The time fractions of the periods of the mobile state and the short, middle and long TALL events, inside and outside the FA, for HeLa cells expressing WT (± its activator Mn²⁺) or mutant β₁ and β₃ integrin proteins (**b**) or before and after treatment with the indicated concentrations of Y27632 (μm) for 1 h (**c**). Data are means ± s.e.m. (for the numbers of observed cells and observed TALL events, see Supplementary Table 2). Fractions that seemed to be immobile were omitted for clarity (Supplementary Tables 2–4 and Supplementary Note 1).

(Fig. 4b and Supplementary Figs. 22 and 24a). β₁-D130A/Y783A/Y795A hardly exhibited even the τ₂ component, and the overall TALL time fraction was decreased to ~15% (Fig. 4b). These results indicate that the middle-length TALL was induced by β₁ integrin binding to either the ECM or the cytoplasmic FA components bound to actin filaments, whereas the longest TALL component was induced by β₁ integrin binding to both the ECM and cytoplasmic FA components.

These results were further confirmed by using a coverslip coated with vitronectin, to which β₁ integrin does not bind[28]. The longest τ₃ component disappeared, supporting the conclusion that this component is due to the binding of β₁ integrin to both the ECM and the actin filament (Supplementary Fig. 26). The time fraction of the τ₃ component of β₃ integrin, which binds to both fibronectin and vitronectin[28], was unchanged, as expected (Supplementary Fig. 26).

Furthermore, the treatment of cells with Y27632, which reduces the traction force on actin filaments by myosin filaments[29] (Supplementary Fig. 26), greatly reduced the τ₃ lifetime and its fraction in a concentration-dependent manner (Fig. 4c and

Supplementary Figs. 23 and 24b). Together, these results indicate that integrin molecules linked the ECM and the cytoplasmic actin filaments for the τ₃ periods (exponential distribution) only when the traction force by myosin II was applied to the actin filaments[30–32]. Consistently, the β₃ integrin protein with the hybrid domain swing-out mutation, β₃-N305T (the product of *ITGB3*^N305T; refs [33–35]), in which the integrin conformation is locked in the fully extended conformation ready for ECM binding, exhibited a slightly elongated τ₃ and an increased time fraction for the τ₃ component as compared to those of wild-type (WT) β₃ integrin[33–36] (Fig. 4b, Supplementary Figs. 22 and 24a, and Supplementary Table 2).

Even outside the FA, integrin molecules exhibited TALL that was characterized by three lifetime components, although the three TALL lifetimes were reduced as compared to those within the FA (Fig. 4, Supplementary Figs. 21–24 and Supplementary Table 2). Integrins might perform force-related functions both inside and outside the FA[37].

It is not clear how the shortest τ₁ TALL component is induced. Perhaps, before an integrin molecule binds to the ECM and/or
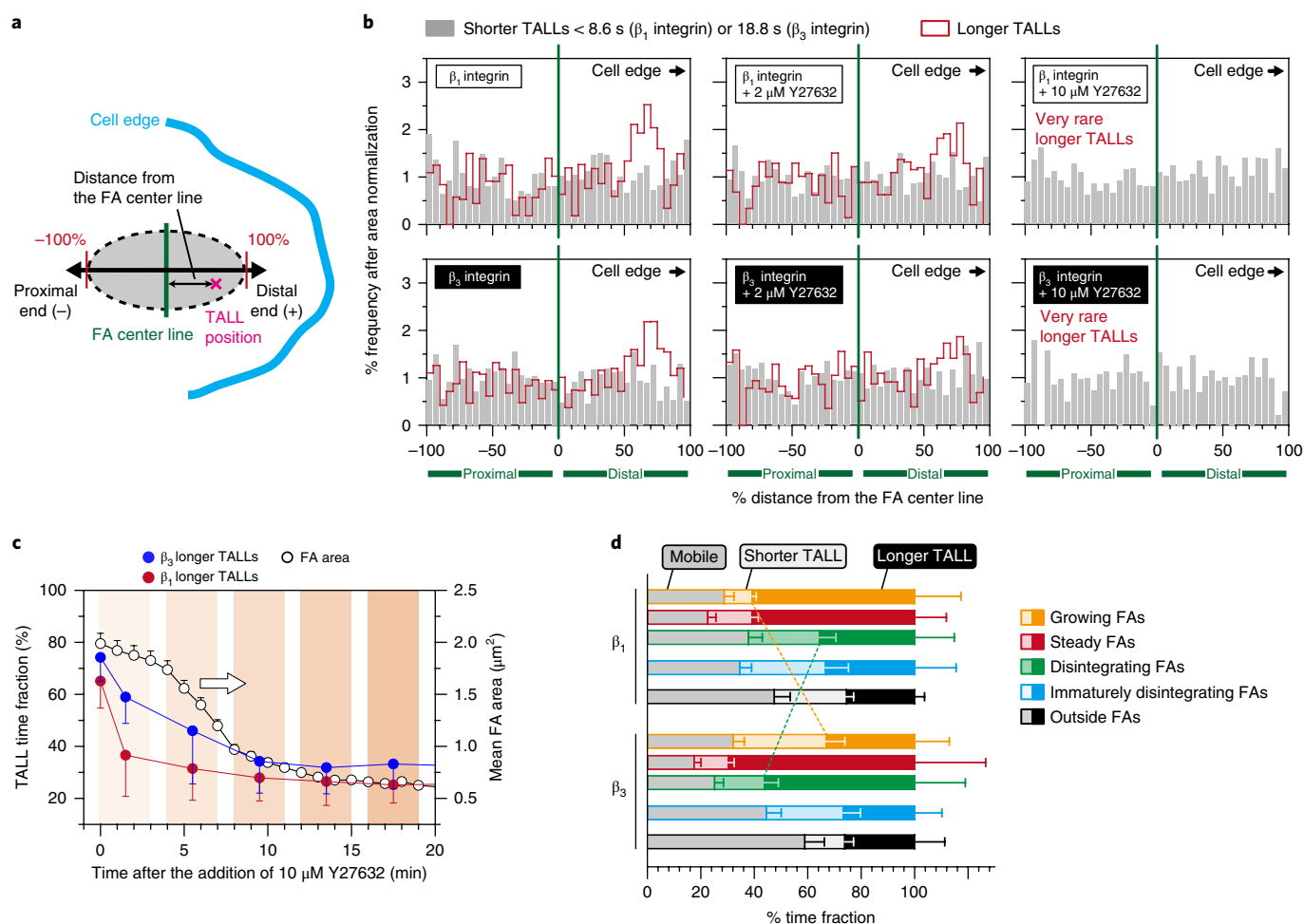
Fig. 5 | Longer TALLs of β_1 and β_3 integrin both occurred most frequently where the traction force was proposed to be largest, whereas in the course of the generation and disintegration of the FAs β_1 integrin arrived at and departed from the FA, respectively, earlier than β_3 integrin. a, Schematic drawing of the FA zone. **b**, Frequencies of longer and shorter TALLs of β_1 integrin (top) and β_3 integrin (bottom) (per unit area, after area normalization), plotted as a function of the location along the FA long axis (distance relative to the half-length of the long axis). For the frequency before the area normalization and the data plotted against the real distance, see Supplementary Fig. 30. For the numbers of inspected TALLs and cells, see Supplementary Table 2. **c**, The time-dependent reductions of the time fractions of longer TALLs of β_1 and β_3 integrin (y axis on the left), followed by that of the mean FA area (y axis on the right), after treatment with the ROCK inhibitor Y27632.Data are means ± s.e.m. of $n = 32$ cells for mean FA area or of $n = 10$ cells for the TALL time fraction; for clarity, error bars were plotted in only one direction. **d**, The time fractions of longer TALLs, shorter TALLs and mobile periods during the four phases of FA growth and disintegration (relative to the entire trajectory length in time): growing FAs (orange), steady FAs (red), disintegrating FAs (green) and immaturely disintegrating FAs (blue) (for the definition of these phases, see Supplementary Fig. 34). Time fractions outside the FAs are shown in black. Data are means ± s.e.m. of $n = 10$ cells per group.

to actin filaments (through interactions with other proteins), which will induce the τ_2- and τ_3-type TALLs, it might undergo weak interactions with (very transient binding to) the molecules in the ECM and/or actin filaments, which might induce τ_1-type TALLs[31,38].

This concept is consistent with another finding, in which four of five TALLs were the τ_1 and τ_2 types (~80% for both β_1 and β_3 integrin; Supplementary Fig. 24a). This implies that only one of the five shorter TALLs turned into the τ_3 type, which represents 80% of TALLs in terms of the time fraction (Fig. 4b). In summary, we propose that integrin molecules continually reach their sites for binding to the ECM and/or to actin filaments one after another and that once out of approximately five times an integrin molecule becomes bound to both the ECM and the actin filament, thus initiating the longest τ_3-type TALLs.

Integrins' longer TALLs tend to occur at distal FA sites. Because the τ_3-type TALLs were implicated in integrin function, we investigated where they occurred in the FA. For this purpose, TALL events lasting longer than $2 \times \tau_2$ (8.6 s and 18.8 s for β_1 and β_3 integrin, respectively), which represent most of the τ_3 component (86 and 78% for β_1 and β_3 integrin, respectively) and the longer ~15 percentiles of the τ_2 component (for both β_1 and β_3 integrin), were examined, using shorter TALLs that lasted for $<2 \times \tau_2$ as controls). Longer TALLs of both β_1 and β_3 integrin occurred most often at two-thirds of the distance away from the FA center toward the distal end (also in the presence of Mn^{2+}) in a myosin II–dependent manner, and thus in a traction-force-dependent manner, whereas shorter TALLs occurred uniformly along the FA long axis (Fig. 5a,b and Supplementary Figs. 28–32).

The actual location where the longer TALLs occurred most often was ~0.7 μm away from the FA center toward the distal end,

although the length of the FA long axis varied greatly (2.4±1.3 (mean±s.d.); Supplementary Fig. 28c). This location is in good agreement with the location where the traction force is highest in the FA[39–41]. Because traction force was required to induce the longer TALLs, we concluded that the longer TALLs are responsible for integrin function by mechanically connecting the ECM and actin filaments in the FA.

Traction force induces integrins' longer TALLs and FA integrity. After cell treatment with 10 μM Y27632, the time fraction of the integrins' longer TALLs decreased rapidly during the initial 1.5 min for β_1 integrin and during the initial 5.5 min for β_3 integrin (Fig. 5c). The mean FA area, as visualized with GFP-paxillin, was decreased by only ~20% during the initial 5 min of the Y27632 treatment, and then further decreased more rapidly between 5 and 15 min (Fig. 5c, Supplementary Fig. 33 and Supplementary Video 6). This result suggests that the integrins' longer TALLs might be important for maintaining FA architecture.

β_1 and β_3 integrin show distinct functions. The occurrence of TALL events in the process of FA maturation and disintegration (in four phases; see Supplementary Fig. 34) was observed (Fig. 5d, Supplementary Fig. 34 and Supplementary Video 7). In the growing phase, β_1 integrin first exhibited large fractions of longer TALLs, whereas β_3 integrin exhibited longer TALLs when the FA was in the mature steady phase (Fig. 5d). In the process of disintegration, the longer TALLs of β_1 integrin were reduced first, whereas β_3 integrin kept displaying longer TALLs for some time (for detailed explanations, see the legend to Supplementary Fig. 34), showing the distinct functions of β_1 and β_3 integrin in the formation, maintenance and disintegration of FAs[36,42,43].

Furthermore, β_1 integrin exhibited a larger fraction of longer TALLs in growing FAs, but ~50% less fractions in immaturely disintegrating FAs (Fig. 5d), whereas β_3 integrin exhibited similar fractions of longer TALLs in both types of FAs. These results indicate that β_1 integrin is responsible for regulating the formation and disintegration of FAs, whereas β_3 integrin is critical for maintaining FAs.

Discussion

Here we found that ST647 (2%O$_2$+TQ20) is most useful as a membrane-impermeable dye, which allowed for observations of up to 12,000 frames (400 s at video rate). To the best of our knowledge, this is the longest single-fluorescent-molecule tracking ever reported. There are only a few membrane-permeable dyes, but TMR (2%O$_2$+TX) was found to be the most useful among them, allowing for observations of up to 3,600 frames (120 s at video rate). Under these optimal conditions, the cellular spreading (ECM-binding) functions were unaffected for at least up to 90 min, and the dark state (when the single-dye molecule blinks) lasting for longer than 1 ms was undetectable.

Super-long SMT analyses of β_1 and β_3 integrin revealed that they are frequently, but temporarily, immobilized in various locations within the FA with durations less than 43 s and 79 s, respectively. Taken together with previous results[34,44,45], we concluded that the longer TALLs, which most frequently occurred two-thirds of the distance away from the FA center toward the distal end, were responsible for the mechanical linkage of the actin cytoskeleton to the ECM, in a manner that was dependent on the traction force generated by myosin II (which would induce important conformational changes in the hybrid domain of integrin[34,35,44]; Supplementary Fig. 35).

Methods

Methods, including statements of data availability and any associated accession codes and references, are available at https://doi.org/10.1038/s41589-018-0032-5.

References

1. Altman, R. B. et al. Cyanine fluorophore derivatives with enhanced photostability. *Nat. Methods* **9**, 68–71 (2011).
2. Altman, R. B. et al. Enhanced photostability of cyanine fluorophores across the visible spectrum. *Nat. Methods* **9**, 428–429 (2012).
3. Lukinavičius, G. et al. A near-infrared fluorophore for live-cell super-resolution microscopy of cellular proteins. *Nat. Chem.* **5**, 132–139 (2013).
4. van der Velde, J. H. M. et al. Mechanism of intramolecular photostabilization in self-healing cyanine fluorophores. *ChemPhysChem* **14**, 4084–4093 (2013).
5. Grimm, J. B. et al. A general method to improve fluorophores for live-cell and single-molecule microscopy. *Nat. Methods* **12**, 244–250 (2015). 3, 250.
6. van der Velde, J. H. M. et al. A simple and versatile design concept for fluorophore derivatives with intramolecular photostabilization. *Nat. Commun.* **7**, 10144 (2016).
7. Giloh, H. & Sedat, J. W. Fluorescence microscopy: reduced photobleaching of rhodamine and fluorescein protein conjugates by *n*-propyl gallate. *Science* **217**, 1252–1255 (1982).
8. Rasnik, I., McKinney, S. A. & Ha, T. Nonblinking and long-lasting single-molecule fluorescence imaging. *Nat. Methods* **3**, 891–893 (2006).
9. Vogelsang, J. et al. A reducing and oxidizing system minimizes photobleaching and blinking of fluorescent dyes. *Angew. Chem. Int. Edn Engl.* **47**, 5465–5469 (2008).
10. Kasper, R. et al. Single-molecule STED microscopy with photostable organic fluorophores. *Small* **6**, 1379–1384 (2010).
11. Cordes, T., Vogelsang, J. & Tinnefeld, P. On the mechanism of trolox as antiblinking and antibleaching reagent. *J. Am. Chem. Soc.* **131**, 5018–5019 (2009).
12. Packer, L. & Fuehr, K. Low oxygen concentration extends the lifespan of cultured human diploid cells. *Nature* **267**, 423–425 (1977).
13. Parsons, M., Messent, A. J., Humphries, J. D., Deakin, N. O. & Humphries, M. J. Quantification of integrin receptor agonism by fluorescence lifetime imaging. *J. Cell Sci.* **121**, 265–271 (2008).
14. Edwald, E., Stone, M. B., Gray, E. M., Wu, J. & Veatch, S. L. Oxygen depletion speeds and simplifies diffusion in HeLa cells. *Biophys. J.* **107**, 1873–1884 (2014).
15. Kusumi, A. et al. Dynamic organizing principles of the plasma membrane that regulate signal transduction: commemorating the fortieth anniversary of Singer and Nicolson's fluid-mosaic model. *Annu. Rev. Cell Dev. Biol.* **28**, 215–250 (2012).
16. Mohyeldin, A., Garzón-Muvdi, T. & Quiñones-Hinojosa, A. Oxygen in stem cell biology: a critical component of the stem cell niche. *Cell Stem Cell* **7**, 150–161 (2010).
17. Semenza, G. L. Oxygen sensing, hypoxia-inducible factors and disease pathophysiology. *Annu. Rev. Pathol.* **9**, 47–71 (2014).
18. Sakadžić, S. et al. Two-photon high-resolution measurement of partial pressure of oxygen in cerebral vasculature and tissue. *Nat. Methods* **7**, 755–759 (2010).
19. Carreau, A., El Hafny-Rahbi, B., Matejuk, A., Grillon, C. & Kieda, C. Why is the partial oxygen pressure of human tissues a crucial parameter? Small molecules and hypoxia. *J. Cell. Mol. Med.* **15**, 1239–1253 (2011).
20. Spencer, J. A. et al. Direct measurement of local oxygen concentration in the bone marrow of live animals. *Nature* **508**, 269–273 (2014).
21. Alejo, J. L., Blanchard, S. C. & Andersen, O. S. Small-molecule photostabilizing agents are modifiers of lipid bilayer properties. *Biophys. J.* **104**, 2410–2418 (2013).
22. Scales, T. M. E. & Parsons, M. Spatial and temporal regulation of integrin signaling during cell migration. *Curr. Opin. Cell Biol.* **23**, 562–568 (2011).
23. Hirata, H., Tatsumi, H., Hayakawa, K. & Sokabe, M. Non-channel mechanosensors working at focal-adhesion–stress-fiber complex. *Pflugers Arch.* **467**, 141–155 (2015).
24. Leduc, C. et al. A highly specific gold nanoprobe for live-cell single-molecule imaging. *Nano Lett.* **13**, 1489–1494 (2013).
25. Mould, A. P. et al. Integrin activation involves a conformational change in the α1 helix of the β-subunit A-domain. *J. Biol. Chem.* **277**, 19800–19805 (2002).
26. Loftus, J. C. et al. A β3-integrin mutation abolishes ligand binding and alters divalent cation-dependent conformation. *Science* **249**, 915–918 (1990).
27. Legate, K. R. & Fässler, R. Mechanisms that regulate adaptor binding to β-integrin cytoplasmic tails. *J. Cell Sci.* **122**, 187–198 (2009).
28. Humphries, J. D., Byron, A. & Humphries, M. J. Integrin ligands at a glance. *J. Cell Sci.* **119**, 3901–3903 (2006).
29. Oakes, P. W., Beckham, Y., Stricker, J. & Gardel, M. L. Tension is required but not sufficient for focal adhesion maturation without a stress fiber template. *J. Cell Biol.* **196**, 363–374 (2012).
30. Kong, F., García, A. J., Mould, A. P., Humphries, M. J. & Zhu, C. Demonstration of catch bonds between an integrin and its ligand. *J. Cell Biol.* **185**, 1275–1284 (2009).

31. Kong, F. et al. Cyclic mechanical reinforcement of integrin–ligand interactions. *Mol. Cell* **49**, 1060–1068 (2013).
32. Livne, A. & Geiger, B. The inner workings of stress fibers—from contractile machinery to focal adhesions and back. *J. Cell Sci.* **129**, 1293–1304 (2016).
33. Cluzel, C. et al. The mechanisms and dynamics of αvβ3 integrin clustering in living cells. *J. Cell Biol.* **171**, 383–392 (2005).
34. Wehrle-Haller, B. Assembly and disassembly of cell matrix adhesions. *Curr. Opin. Cell Biol.* **24**, 569–581 (2012).
35. Li, J. & Springer, T. A. Integrin extension enables ultrasensitive regulation by cytoskeletal force. *Proc. Natl Acad. Sci. USA* **114**, 4685–4690 (2017).
36. Rossier, O. et al. Integrins β1 and β3 exhibit distinct dynamic nanoscale organizations inside focal adhesions. *Nat. Cell Biol.* **14**, 1057–1067 (2012).
37. Wang, Y. & Wang, X. Integrins outside focal adhesions transmit tensions during stable cell adhesion. *Sci. Rep.* **6**, 36959 (2016).
38. Jiang, G., Giannone, G., Critchley, D. R., Fukumoto, E. & Sheetz, M. P. Two-piconewton slip bond between fibronectin and the cytoskeleton depends on talin. *Nature* **424**, 334–337 (2003).
39. Plotnikov, S. V., Pasapera, A. M., Sabass, B. & Waterman, C. M. Force fluctuations within focal adhesions mediate ECM-rigidity sensing to guide directed cell migration. *Cell* **151**, 1513–1527 (2012).
40. Blakely, B. L. et al. A DNA-based molecular probe for optically reporting cellular traction forces. *Nat. Methods* **11**, 1229–1232 (2014).
41. Morimatsu, M., Mekhdjian, A. H., Chang, A. C., Tan, S. J. & Dunn, A. R. Visualizing the interior architecture of focal adhesions with high-resolution traction maps. *Nano Lett.* **15**, 2220–2228 (2015).
42. Roca-Cusachs, P., Gauthier, N. C., Del Rio, A. & Sheetz, M. P. Clustering of α5β1 integrins determines adhesion strength, whereas αvβ3 and talin enable mechanotransduction. *Proc. Natl Acad. Sci. USA* **106**, 16245–16250 (2009).
43. Schiller, H. B. et al. β1- and αv-class integrins cooperate to regulate myosin II during rigidity sensing of fibronectin-based microenvironments. *Nat. Cell Biol.* **15**, 625–636 (2013).
44. Wehrle-Haller, B. Structure and function of focal adhesions. *Curr. Opin. Cell Biol.* **24**, 116–124 (2012).
45. Doyle, A. D. & Yamada, K. M. Mechanosensing via cell-matrix adhesions in 3D microenvironments. *Exp. Cell Res.* **343**, 60–66 (2016).

Author contributions

T.A.T. performed a large majority of the single-fluorescent-molecule tracking experiments and prepared trolox; Y.W., J.G. and K.N. performed some of the single-fluorescent-molecule tracking experiments to examine the effects of O$_2$ and ROXS on the photobleaching of fluorescent dye molecules, under the guidance of T.A.T.; T.K.F. and A.K. developed the single-molecule imaging camera system, set up the single-molecule instruments and developed the analysis software; R.S.K., K.G.N.S., T.K.F. and A.K. participated in extensive discussions during the course of this research; T.A.T., T.K.F. and A.K. conceived and formulated this project, and evaluated and discussed data; T.A.T. and A.K. wrote the manuscript; and all of the authors participated in revising the manuscript.

Competing interests

The authors declare no competing interests.

Additional information

Supplementary information is available for this paper at https://doi.org/10.1038/s41589-018-0032-5.

Reprints and permissions information is available at www.nature.com/reprints.

Correspondence and requests for materials should be addressed to A.K.

Publisher's note: Springer Nature remains neutral with regard to jurisdictional claims in published maps and institutional affiliations.

Methods

Cell culture and transfection. T24 cells, a kind gift from Masahiro Sokabe (Nagoya University)[46], HeLa cells (purchased from RIKEN cell bank, RCB0007) and CHO-K1 cells (purchased from Dainippon Pharma Co., Ltd., Osaka, 03-402) were cultured in Ham's nutrient mixture F12 (Sigma-Aldrich), supplemented with 10% (vol/vol) fetal bovine serum (FBS, Life Technologies). NIH3T3 cells (a kind gift from Makoto Kinoshita (Nagoya University))[47] were cultured in Dulbecco's modified Eagle's medium (DMEM, Sigma-Aldrich), supplemented with 10% (vol/vol) FBS. The β1-KO (*Itgb1*-knockout) MEFs were a kind gift from Martin Humphries (University of Manchester)[13]. The cells were cultured in DMEM supplemented with 10% (vol/vol) FBS and 20 U/ml interferon (IFN)-γ (Sigma-Aldrich), at 33 °C. About 24 h before use, the culture medium was replaced by DMEM supplemented with 10% (vol/vol) FBS without IFN-γ at 37 °C. All cell lines were tested for mycoplasma contamination with MycoAlert (Lonza). The identities of the T24 and HeLa cell lines were authenticated by PowerPlex16 STR (contracted to Promega).

For fluorescence microscopy of the cells, the cells were always plated in 12-mm-glass-bottom dishes (Iwaki, Tokyo), pre-coated with fibronectin (FN, Sigma-Aldrich) by placing 10 μg/ml FN on the glass for 1 h at room temperature. The cells were cultured in the growth medium for 24–48 h. Before observation, the culture medium was replaced by the observation medium, T-HBSS. For the experiments involving observing the effect of integrin activation with Mn²⁺, the cells were cultured in the presence of 1 mM MnCl₂ for 1 h before microscope observations.

T24 cells were transfected with the cDNAs encoding CD47 linked to various tag proteins using Lipofectamine LTX (Life Technologies), according to the manufacturer's recommendations. HeLa cells, MEFs and β₁-KO MEFs were transfected with the cDNAs encoding WT β₁ and β₃ integrin and their various mutants, using an electroporator (Nucleofector 2, Lonza; CLB solution and program I-13 for HeLa cells; CLB solution and program A-23 for MEFs), according to the manufacturer's recommendations.

cDNA construction. The cDNA encoding human *CD47* isoform 2 was a kind gift from Eric Brown (Genentech) (NCBI reference sequence: NM_198793.2)[48]. The cDNA encoding human *ITGB1* isoform β-1A was purchased from the NITE Biological Resource Center (NBRC, Tokyo, accession number: AK291697, http://getentry.ddbj.nig.ac.jp/getentry?accession_number=AK291697; NCBI reference sequence: NM_002211.3). The cDNA encoding human *ITGB3* was a kind gift from Jonathan C. Jones (Northwestern University) (NCBI reference sequence: NM_000212.2)[49]. The human paxillin isoform alpha cDNA was cloned from the WI38 cell line (NCBI reference sequence: NM_002859.3). The cDNAs encoding acyl carrier protein (ACP), Halo7 and mGFP (A206K) were obtained from New England Biolabs, Promega and Clontech, respectively. A linker sequence of five amino acids (Ser-Gly-Gly-Gly-Gly) was inserted between the target protein and ACP or mGFP, whereas a 15 amino acid linker ((Ser-Gly-Gly-Gly-Gly)₃) was inserted between the target protein and Halo7. When a tag protein was attached to the N terminus of a transmembrane protein, an additional signal sequence was attached to the N terminus of the tag protein; i.e., the signal peptide (SP) of CD47 for ACP-CD47, the SP of IL-6 for Halo7-CD47, and the SP of CD8 for ACP–β₁ integrin and ACP–β₃ integrin. For the generation of the β₁ integrin mutants *ITGB1*^D130A, *ITGB1*^Y783A/Y795A and *ITGB1*^D130A/Y783A/Y795A, site-directed mutagenesis was performed using an Agilent Technologies QuikChange site-directed mutagenesis kit. The sequences encoding ACP-CD47, Halo7-CD47, CD47-Halo7 and CD47-mGFP were subcloned into the pOStet15T3 vector (an episomal vector based on the Epstein–Barr virus that carries the tetracycline-regulated expression units: the transactivator (rtTA2-M2) and *tetO* sequence (a Tet-on vector)). The sequences encoding mGFP-paxillin, β₁ integrin, ACP–β₁ integrin (WT and mutant), β₁ integrin–mGFP and ACP–β₃ integrin (WT and mutant) were subcloned into the pEGFP vector (Clontech). For the details of the cDNA constructs including the linker sequences, see Supplementary Fig. 36.

Fluorescent dyes and fluorescent labeling. Atto488 (AT488)-CoA, DY547-CoA and DY647-CoA were purchased from New England Biolabs. Tetramethylrhodamine (TMR)-Halo, Alexa488 (AL488)-Halo and R110-Halo ligands were purchased from Promega. The syntheses of CoA ligands conjugated with fluorescent dye molecules, TMR, AT594, AT647N and ST647 (TMR-CoA, AT594-CoA, AT647N-CoA and ST647-CoA, respectively), and those of Halo ligands conjugated with AT594 and ST647 (AT594-Halo and ST647-Halo ligands, respectively), as well as those of the CoA and Halo ligands that were linked to fluorescent compounds, Cy3, Cy5, TMR and AT594, by way of TX (Cy3-TX-Halo, Cy5-TX-Halo and TMR-TX-Halo ligands, and AT594-TX-CoA, respectively) are described in Supplementary Note 2. The chemical syntheses of fluorescently conjugated Halo ligands and CoA compounds were performed by Shinsei Chemical Co., Ltd. (Osaka, Japan).

ACP-tagged CD47 and WT and mutant integrins expressed on the cell surface (ACP tag in the extracellular N terminus) were covalently labeled with fluorescent dye compounds by incubating the cells with 50 nM dye-conjugated CoA and 2 μM ACP synthase (New England Biolabs) in the complete growth medium (containing 10 mM MgCl₂, which was sufficient for activating the synthase) at 37 °C for 15 min.

Halo7-tagged proteins expressed in the PM (both inside and outside the cell) were covalently conjugated with fluorescent organic molecules by incubating the cells with 5 nM Halo ligands linked to TMR or AL488 in the complete growth medium at 37 °C for 15 min, or with 5 nM R110-Halo-ligand in the complete growth medium at 37 °C overnight. Under these conditions, 10~20% of expressed proteins were fluorescently labeled.

Microscopy observations of the cells at various O₂ concentrations. To maintain the cells at 37 °C during the microscopy observation period, the entire microscope, except for the excitation arm and the detection arms, was placed in a microscope environment chamber made with thermo- and electric-field-insulating plastic, and three heating circulators (SKH0-112-OT, Kokensya, Tokyo, Japan) were placed in the box to supply warmed air and to slow air circulation within the box (Supplementary Fig. 3a). A stage-top incubator (Tokai hit, Tokyo, Japan) was placed on the microscope stage for further stabilization of the temperature and for varying the partial pressure of molecular oxygen in the gas environment (Supplementary Fig. 3a). The bottom plane of the chamber had a hole in which a glass-base dish could be placed snugly, to let the gas in the chamber escape from the chamber only slowly. On the lid of this chamber, two small holes were made for the tubing to inject the humidified gas mixture and to place the micro-electrode for monitoring dissolved oxygen concentrations.

The N₂ gas and air (79%N₂+21%O₂) were supplied from each tank and mixed with a multi-gas mixer (Log MIX, FRONT Co., Ltd., Tokyo, Japan) with flow meters. The gas mixture was humidified by passage through a bottle filled with ultrapure water and was then continuously supplied to the surface of the solution covering the cells attached to the glass-base dish at a flow-rate of 200 ml/min. The dissolved O₂ concentration in the cell-culture medium was directly monitored with a microdissolved-oxygen electrode (DO-166MT; Lazer Research Laboratories, Los Angeles, CA, USA) or a fluorescence-based micro-oxygen probe (MicroTX3; PreSens Precision Sensing GmbH, Regensburg, Germany). The dissolved O₂ concentration in the medium was adjusted by varying the air fraction of the equilibrating gas mixture. When the concentration of the O₂ in the gas mixture was changed, the dissolved O₂ concentration in the specimen was stabilized at the new concentration within 4 min (Supplementary Fig. 3b). In this gas-environment chamber, probably due to the leakage of atmospheric oxygen, oxygen concentrations <0.5% were difficult to attain.

To further reduce the dissolved oxygen concentrations below the sensor's detection limit of 0.05%O₂, an enzymatic method was used. The culture medium was replaced with TES–HBSS buffer containing 0.5 mg/ml glucose oxidase and 40 μg/ml catalase, with or without ROXS, supplemented with 2% glucose (instead of the normal 0.1% glucose; for a sufficient supply of glucose) and 20 mM TES (instead of 2 mM TES; for pH stabilization against pH decreases due to the generation of gluconic acid by the enzymatic reactions to reduce the dissolved oxygen concentration) (GLOX buffer). When the surface of the GLOX buffer in the glass-base dish was left uncovered, owing to the newly dissolved O₂ from the atmosphere in the GLOX buffer, the glucose oxidase–catalase system continually generated gluconic acid (thus lowering the pH), which might have affected the live cells. To suppress the further influx of molecular oxygen into the GLOX buffer, a round cover made of aluminum foil was placed on the surface of the GLOX buffer. This effectively blocked the pH changes of the GLOX buffer, and the dissolved O₂ concentration was maintained below the detection limit for at least 2 h (<0.05%; Supplementary Fig. 3b). For longer-term incubation periods, the GLOX buffer was replaced every 2 h to prevent acidification.

ROXS solution preparation. Trolox was first dissolved in dry DMSO at a concentration of 0.5 M, and then diluted in T-HBSS. Troloxquinone was generated by UV (UVP, 302 nm, 15 W)-induced oxidation of 1.5 mM trolox in ultrapure water with air bubbling (to supply O₂) until the troloxquinone/trolox ratio reached 0.6:0.4 (typically in 10–20 min), as described previously[11] (Supplementary Fig. 4). The troloxquinone/trolox ratio in the solution was determined by measuring the optical density at 255 nm, as described previously[11], using an optical absorption spectrometer (U-3900H, Hitachi). A stock solution containing trolox and troloxquinone, at a molar ratio of 4:6, was produced by mixing this solution (prepared by UV-induced oxidation) with the TX solution; this was stored at 4 °C in the dark and used within a week. In the present research, the final concentration of trolox+troloxquinone was always 1 mM (in T-HBSS).

Assays for cell growth, cytotoxicity and cell spreading. To examine cell growth, cells were seeded in complete growth medium in 6-well tissue culture dishes (35-mm diameter; Iwaki) and cultured under a gas mixture containing 5% CO₂ and 21%O₂, 5%O₂ or 2%O₂ (+74%, 90%, or 93% N₂, respectively), using a multi-gas incubator MG-70M (Taitec, Tokyo), at 37 °C. Cells were removed from the culture dish every ~12 h, using the standard trypsin solution used in our study (0.25% trypsin and 1 mM EDTA in 10 mM PBS, pH 7.4), and mixed with a trypan blue solution; the live cells, which were not stained with trypan blue, were counted with a hemocytometer. The experiments were repeated for six independent specimens, and the mean ± s.e.m. was determined.

To quantitatively examine cell survival in the presence of ROXS reagents at 21%O₂ and 2%O₂ atmospheres in a time course up to 8 h, cells were plated on

FN-coated 35-mm tissue culture dishes and cultured in the complete growth medium for ~24 h. The medium was then replaced by T-HBSS that was prewarmed to 37 °C, with or without ROXS reagents. For experiments involving <0.05% dissolved oxygen (which is the detection limit of the sensor employed here), the GLOX buffer was used. Cells were removed from the culture dish by the standard trypsin solution every ~1 h. The number of live cells was evaluated as described for the cell growth assay.

For examining cell survival by imaging, cells cultured on FN-coated glass-base dishes were stained with 10 ng/ml PI in T-HBSS for 5 min and then fixed with 4% paraformaldehyde for 15 min. After fixation, phase-contrast and fluorescence microscopic images of the cells were obtained with an Olympus IX70 inverted epifluorescence microscope equipped with a 60×1.25 numerical aperture (NA) Plan Apo objective lens and an Andor-Clara cooled charge-coupled device (CCD) camera.

The influences of low oxygen concentrations and/or the presence of ROXS reagents on the spreading of β_1-KO MEFs and β_1-KO MEFs that were transfected with constructs encoding WT or modified β_1 integrin molecules on FN-coated glass-bottom dishes were examined. β_1-KO MEFs were transfected with the cDNAs encoding various β_1 integrin proteins by electroporation, as described in the subsection "Cell culture and transfection," cultured for 18 h, removed from the cell culture dish by trypsinization for 3 min, allowed to recover in the complete growth medium for 1 h, and then replated on FN-coated glass-bottom dishes in T-HBSS with or without ROXS or in the GLOX buffer with or without ROXS. At selected time points after plating, the cells were fixed with 4% paraformaldehyde for 1 h, incubated with 100 mM glycine for 15 min, permeabilized with 0.1% Triton X-100 for 5 min and then further incubated with 1% BSA for 1 h. The cells were then immunostained with 20 μM anti–β_1 integrin monoclonal antibody (K-20, also called 'neutral mAb', which recognizes both active and inactive β_1 integrin; Santa Cruz) for 1 h and then with 5 μM rhodamine red-X-labeled anti-mouse-IgG secondary antibody (Jackson ImmunoResearch, 715-295-151) for 1 h. Microscopic observations were conducted as described in the previous paragraph. The cell area (parameter for evaluating cell spreading) was measured in the phase-contrast images, using ImageJ software. Results are described as means ± s.e.m. for 20 cells.

Confocal imaging of mGFP-paxillin and Alexa647-conjugated phalloidin in cells before and after the treatment with the ROCK inhibitor Y27632. HeLa cells expressing mGFP-paxillin, which were replated on FN-coated glass-base dishes, were incubated with 1–10 μM Y27632 in T-HBSS for 1 h. The cells were then fixed with 4% paraformaldehyde for 1 h and incubated with 100 mM glycine for 15 min, 0.1% Triton X-100 for 5 min, 1% BSA for 1 h and then 500 nM Alexa647-phalloidin (Life Technologies) for 30 min, followed by embedding in Permafluor (Thermo Scientific) for confocal fluorescence microscopy (Olympus, FV1000) (Supplementary Fig. 27a).

Single-fluorescent-molecule imaging. Fluorescently labeled molecules located in the basal PM (the ventral PM; i.e., the PM facing the coverslip), and those attached to the coverslip, were illuminated with an evanescent field and observed at 37 °C, using home-built objective-lens-type TIRF microscopes, which were constructed on Olympus inverted microscopes (IX-81 and 70 for video-rate and high-speed observations, respectively) equipped with Olympus 100×1.49 NA objective lenses. The fluorescence images were projected onto a two-stage microchannel plate intensifier (C8600-03; Hamamatsu Photonics), which was lens-coupled to an electron bombardment CCD camera (C7190-23; Hamamatsu Photonics) operated at video rate or was optical-fiber-bundle-coupled to a high-speed complementary metal oxide semiconductor sensor camera (Focuscope SV-10k; Photron) operated at 1 and 10 kHz (256×256 pixels)[50].

The incident excitation laser power at the exit of the objective lens was 1.98 mW for the 488-nm line (for AT488, AL488, and R110), 2.31 mW or 4.60 mW for the 561-nm line (for TMR or DY547 and Cy3-TX, respectively), 1.17 mW for the 594-nm line (for AT594), and 1.06 mW or 3.18 mW for the 642-nm line (for DY647, AT674N, and ST647 or Cy5-TX, respectively). For high-speed observations of TMR (561-nm line), 10.8 and 108 mW were used for the observation frame rates of 1 and 10 kHz, respectively.

Each individual fluorescent spot in the image was identified and tracked by using a home-made computer program, as described previously[51]. The superimposition of images in different colors obtained by two separate cameras was conducted as described previously[50].

Methods to measure photobleaching lifetimes and durations in which single molecules could be tracked, and the mean signal intensity of single fluorescent spots. As a convenient measure for the photobleaching lifetime, the 'number-counting lifetime' measure was used. In this method, after obtaining image sequences at video rate, the number of fluorescence spots detected in each video frame was obtained and plotted against time, and then the numbers of spots in each frame (time bin) obtained in all of the image sequences were added together. We found that these plots of the (total) number of fluorescent spots versus time for all of the dye molecules under all of the ROXS conditions used here could be fitted by single-exponential functions. Therefore, the exponential decay constants (mean ± s.e.m.) were defined as the number-counting lifetime.

The number-counting photobleaching lifetime would virtually be the same as the lifetime evaluated by the bulk intensity measurements.

As another method, the 'single-molecule tracking lifetime' was used. In this method, we measured the duration in which each fluorescent spot was detectable, starting from the initiation of the observation by turning on the excitation laser (time 0; until the first transition to the dark state; this way, we only observed the molecules that were visible at time 0). After observing many single molecules, we obtained the histogram for the bright-state durations. This histogram might resemble that for the on-time distributions, but because it was observed from the start of excitation laser illumination, rather than the onset of fluorescence emission during steady-state illumination, the actual values would be different. However, we used this method because it would provide the lifetime more relevant to actual experiments conducted using live cells, as it provides the distribution of the lengths of single-molecule trajectories observed from time 0 (starting of laser excitation). We found that the distributions for all of the molecules under all of the ROXS conditions used here could operationally be fitted by single-exponential functions; the exponential decay constants (means ± s.e.m.) were used as 'single-molecule tracking lifetimes'.

The mean (± s.e.m.) fluorescence intensity of single fluorescence spots was obtained in the following way. After measuring the fluorescence signal intensities of all the fluorescence spots, the distribution of the intensities was fitted by a log-normal function, and the mean intensity was obtained as the value of the mode of the log-normal function.

Note that in these determinations, the s.e.m. is provided as the fitting error of the 68.3% confidence limit. In such determinations, the number of independent experiments is given as the degree of freedom for fitting (ν), which equals 'the number of bins used for the fitting' minus 'the number of free parameters used for the fitting'. However, because the number of total fluorescence spots and the number of events (various events observed in the present research, such as the TALL events) would also be useful for clarifying the conducted experiments, in addition to the degree of freedom, we describe the numbers of independent experiments and the numbers of observed molecules, events or cells, wherever appropriate.

Long-term tracking of single integrin molecules inside and outside the FA. HeLa cells transfected with sequences encoding ACP-integrins (WT and mutant β_1 integrin and β_3 integrin) and mGFP-paxillin were cultured for 24–48 h on FN-coated glass-bottom dishes, and the ACP-integrins were labeled with ST647-CoA by the same method used for labeling ACP-CD47. For the long-term tracking of single individual integrin molecules inside and outside FAs, the stage drift was corrected by using 100-nm fluorescent tetraspeck beads (Life Technologies) that were attached to the glass surface in the specimen as fiducial markers.

Single ST647 molecules attached to the coverglass of the glass-base dish were observed at a video rate for 6,000 frames (200 s), and after correcting for the long-term drift using the fiducial markers, the localization precisions of single ST647 molecules (31 molecules) were found to be 26 nm for both the x and y coordinates. These values should be compared with the localization precision for short-term observations (100 frames ~3 s) of 22 nm. This result showed that long-term tracking, such as 6,000 frames, could be performed at localization precisions comparable to those attainable for much shorter trajectories, such as 100 frames, after correction for the stage drift.

Transient-immobilization or TALL events were detected in single-molecule tracking trajectories, by using the algorithm developed by Sahl et al.[52] and modified by Shibata et al.[53]. The detection circle (magnifying-glass) radius and the threshold residency time were set at 200 nm and 20 frames (0.67 s), respectively. Using these parameter values, the TALL time fractions in Monte-Carlo-generated simple-Brownian trajectories with diffusion coefficients of 0.16 and 0.27 μm²/s, which are the mean diffusion coefficients for β_1 integrin inside and outside the FA region, respectively, were found to be only 1.42 ± 0.02% and 0.26 ± 0.01%, respectively.

To identify and define the FA areas, mGFP-paxillin was expressed in cells and used as an FA marker. The cells that expressed both mGFP-paxillin and ACP-integrin were selected. First, the mGFP-paxillin images were recorded for 3.3 s (100 video frames, not at the level of single molecules); subsequently, the ST647-labeled ACP-integrin was observed for 6,000 frames (200 s) at the level of single molecules. Consistent with the results described by Shibata et al.[53], the changes in the FA morphology during ~200 s were limited, and therefore, the mGFP-paxillin image sequence obtained before the single-molecule observations of integrins was used to define the FA areas. The entire image sequence of 100 frames was averaged, and the resulting image was binarized to determine the boundaries between the FA regions and the bulk PM domain. The threshold pixel value used for binarization was found by using an adaptive thresholding algorithm. For the successful binarization of both the larger and smaller FAs, the images before and after Laplacian filtering were binarized, and then the binarized images were compared. For further details, see Supplementary Fig. 20 and its legend. All integrin trajectories were subdivided into those inside and outside the FA zones, and then analyzed.

Software and statistical analysis. TIRF images of FAs were processed and analyzed using ImageJ for Windows or MatLab 2012a for Windows. Superimposition

of image sequences obtained in two colors and single-molecule tracking were performed using C++-based computer programs produced in-house, as described previously[50,51]. Statistical analysis was performed by two-sided Welch's t-test or two-sided Mann–Whitney U test using OriginPro 2015 for Windows. $P < 0.05$ was considered to be statistically significant. Curve fitting and its examination using Akaike's and Bayesian information criteria were performed using OriginPro 2015 for Windows.

Life Sciences Reporting Summary. Further information on experimental design is available in the Life Sciences Reporting Summary.

Data availability. All data generated or analyzed for this study are available within the paper and its associated supplementary information files. All other data presented and codes written are available upon reasonable request from the corresponding author.

References

46. Naruse, K., Sai, X., Yokoyama, N. & Sokabe, M. Uniaxial cyclic stretch induces c-SRC activation and translocation in human endothelial cells via SA channel activation. *FEBS Lett.* **441**, 111–115 (1998).
47. Ihara, M. et al. Association of the cytoskeletal GTP-binding protein Sept4 (H5) with cytoplasmic inclusions found in Parkinson's disease and other synucleinopathies. *J. Biol. Chem.* **278**, 24095–24102 (2003).
48. Lindberg, F. P., Gresham, H. D., Schwarz, E. & Brown, E. J. Molecular cloning of integrin-associated protein: an immunoglobulin family member with multiple membrane-spanning domains implicated in αvβ3-dependent ligand binding. *J. Cell Biol.* **123**, 485–496 (1993).
49. Tsuruta, D. et al. Microfilament-dependent movement of the β3-integrin subunit within focal contacts of endothelial cells. *FASEB J.* **16**, 866–868 (2002).
50. Koyama-Honda, I. et al. Fluorescence imaging for monitoring the colocalization of two single molecules in living cells. *Biophys. J.* **88**, 2126–2136 (2005).
51. Fujiwara, T., Ritchie, K., Murakoshi, H., Jacobson, K. & Kusumi, A. Phospholipids undergo hop diffusion in compartmentalized cell membrane. *J. Cell Biol.* **157**, 1071–1081 (2002).
52. Sahl, S. J., Leutenegger, M., Hilbert, M., Hell, S. W. & Eggeling, C. Fast molecular tracking maps nanoscale dynamics of plasma membrane lipids. *Proc. Natl Acad. Sci. USA* **107**, 6829–6834 (2010).
53. Shibata, A. C. E. et al. Archipelago architecture of the focal adhesion: membrane molecules freely enter and exit from the focal adhesion zone. *Cytoskeleton* **69**, 380–392 (2012).

Corresponding author(s): Akihiro Kusumi

☐ Initial submission   ☐ Revised version   ☒ Final submission

Life Sciences Reporting Summary

Nature Research wishes to improve the reproducibility of the work that we publish. This form is intended for publication with all accepted life science papers and provides structure for consistency and transparency in reporting. Every life science submission will use this form; some list items might not apply to an individual manuscript, but all fields must be completed for clarity.

For further information on the points included in this form, see Reporting Life Sciences Research. For further information on Nature Research policies, including our data availability policy, see Authors & Referees and the Editorial Policy Checklist.

▶ Experimental design

1. Sample size

Describe how sample size was determined.

> We performed pilot experiments using smaller sample numbers, and after performing Student t-test, we determined the expected minimal sample size to prove or disprove the hypothesis. We generally did more experiments than this minimal number of experiments.

2. Data exclusions

Describe any data exclusions.

> No data exclusions.

3. Replication

Describe whether the experimental findings were reliably reproduced.

> All experimental findings were reliably reproduced.

4. Randomization

Describe how samples/organisms/participants were allocated into experimental groups.

> All sample allocations were random.

5. Blinding

Describe whether the investigators were blinded to group allocation during data collection and/or analysis.

> The sample preparation and observation were mostly preformed by the same operator. Therefore, no blinding was performed.

Note: all studies involving animals and/or human research participants must disclose whether blinding and randomization were used.

6. Statistical parameters

For all figures and tables that use statistical methods, confirm that the following items are present in relevant figure legends (or in the Methods section if additional space is needed).

n/a	Confirmed	
☐	☒	The exact sample size (n) for each experimental group/condition, given as a discrete number and unit of measurement (animals, litters, cultures, etc.)
☐	☒	A description of how samples were collected, noting whether measurements were taken from distinct samples or whether the same sample was measured repeatedly
☐	☒	A statement indicating how many times each experiment was replicated
☐	☒	The statistical test(s) used and whether they are one- or two-sided (note: only common tests should be described solely by name; more complex techniques should be described in the Methods section)
☐	☒	A description of any assumptions or corrections, such as an adjustment for multiple comparisons
☐	☒	The test results (e.g. P values) given as exact values whenever possible and with confidence intervals noted
☐	☒	A clear description of statistics including central tendency (e.g. median, mean) and variation (e.g. standard deviation, interquartile range)
☐	☒	Clearly defined error bars

See the web collection on statistics for biologists for further resources and guidance.

▶ Software

Policy information about availability of computer code

7. Software

Describe the software used to analyze the data in this study.

> All the software used is described in the Methods section, under the heading "Software and statistical analysis". Data and code availability statement is now placed as an independent Subsection with the heading "Data and code availability" at the end of the Methods section.

For manuscripts utilizing custom algorithms or software that are central to the paper but not yet described in the published literature, software must be made available to editors and reviewers upon request. We strongly encourage code deposition in a community repository (e.g. GitHub). *Nature Methods* guidance for providing algorithms and software for publication provides further information on this topic.

▶ Materials and reagents

Policy information about availability of materials

8. Materials availability

Indicate whether there are restrictions on availability of unique materials or if these materials are only available for distribution by a for-profit company.

> No restricted materials were used in this study.

9. Antibodies

Describe the antibodies used and how they were validated for use in the system under study (i.e. assay and species).

> Anti-integrin β1 monoclonal antibody IgG (Santa Cruz, K20)
> Rhodamine red X-labeled anti-mouse IgG secondary antibody (Jackson Immuno Research 715-295-151)
> These have been described in the Methods section.

10. Eukaryotic cell lines

a. State the source of each eukaryotic cell line used.

> T24 is a kind gift from Masahiro Sokabe of Nagoya University; Naruse, K., Sai, X., Yokoyama, N. & Sokabe, M. FEBS Lett. 441, 111–115 (1998).
> HeLa is purchased from RIKEN cell bank (RCB0007).
> CHO-K1 is purchased from Dainippon Pharma Co., Ltd., Osaka (03-402).
> NIH3T3 is a kind gift from Makoto Kinoshita of Nagoya University; Ihara, M. et al. J. Biol. Chem. 278, 24095–24102 (2003).
> These are described in the Methods section.

b. Describe the method of cell line authentication used.

> The identities of the T24 and HeLa cell lines were authenticated by PowerPlex16 STR (contract to Promega).
> CHO-K1 and NIH3T3 cell lines were not authenticized.
> These are described in the Methods section.

c. Report whether the cell lines were tested for mycoplasma contamination.

> All cell lines used were proved to be mycoplasma free using MycoAlert (Lonza), and this is described in the Methods section.

d. If any of the cell lines used are listed in the database of commonly misidentified cell lines maintained by ICLAC, provide a scientific rationale for their use.

> T24 human epithelial bladder carcinoma cells used in this study were previously misidentified as ECV304 human endothelial cells. We used this cell line here because the structure and molecular dynamics in the plasma membrane have been very well characterized by us as well as many others.

▶ Animals and human research participants

Policy information about studies involving animals; when reporting animal research, follow the ARRIVE guidelines

11. Description of research animals

Provide details on animals and/or animal-derived materials used in the study.

> No animals were used in this study.

Policy information about studies involving human research participants

12. Description of human research participants

Describe the covariate-relevant population characteristics of the human research participants.

> This study did not involve human research participants.

In the format provided by the authors and unedited.

Super-long single-molecule tracking reveals dynamic-anchorage-induced integrin function

Taka A. Tsunoyama [1], Yusuke Watanabe[2], Junri Goto[2], Kazuma Naito[2], Rinshi S. Kasai[3], Kenichi G. N. Suzuki[2,4], Takahiro K. Fujiwara[2] and Akihiro Kusumi[1,2,3]*

[1]Membrane Cooperativity Unit, Okinawa Institute of Science and Technology Graduate University (OIST), Onna, Japan. [2]Institute for Integrated Cell-Material Sciences (WPI-iCeMS), Kyoto University, Kyoto, Japan. [3]Institute for Frontier Life and Medical Sciences, Kyoto University, Kyoto, Japan. [4]Present address: Center for Highly Advanced Integration of Nano and Life Sciences (G-CHAIN), Gifu University, Gifu, Japan. *e-mail: akihiro.kusumi@oist.jp

Super-long single-molecule tracking reveals dynamic-anchorage-induced integrin function

Taka A. Tsunoyama, Yusuke Watanabe, Junri Goto, Kazuma Naito, Kenichi G.N. Suzuki, Takahiro K. Fujiwara and Akihiro Kusumi

— Supplementary Information —

Note: Supplementary Videos are available on the Nature Chemical Biology website.

Supplementary Tables

Supplementary Table 1 | Summary of photobleaching lifetimes, fluorescence intensities, single-molecule localization precisions, the numbers of inspected fluorescent spots, and the degrees of freedom for fitting, for all fluorophores observed under all of the conditions employed in this study. Grey shading: control. Orange shading: optimal conditions. See **Fig. 1d** and **Supplementary Fig. 7** for graphical summaries.

Tag protein-Dye	Outside/ Inside the cell	Live/ Fixed cells	O_2 (%)	ROXS	Photobleaching lifetime (s)[a]	Relative prolongation (fold)[a]	Relative intensity (fold)[b]	Precision (nm)	N ($\times10^4$)[c]	ν[d]
Halo-R110	Outside	Live	21	-	5.2 ± 0.07	1.0 ± 0.02	1.0 ± 0.02	32.5	14.8	897
				TX	8.4 ± 0.06	1.6 ± 0.03	1.1 ± 0.01	-	20.1	897
				TQ20	4.0 ± 0.02	0.8 ± 0.02	1.1 ± 0.01	-	6.0	897
				TQ40	1.1 ± 0.01	0.2 ± 0.01	1.0 ± 0.01	-	2.9	897
			2	-	5.1 ± 0.08	1.0 ± 0.02	0.9 ± 0.01	-	6.2	897
				TX	7.4 ± 0.06	1.4 ± 0.02	1.2 ± 0.01	-	17.5	1497
				TQ20	3.9 ± 0.03	0.8 ± 0.01	1.0 ± 0.02	-	6.1	1497
				TQ40	1.9 ± 0.01	0.4 ± 0.01	0.9 ± 0.01	-	3.1	897
			0	-	N. A.[e]		N. A.[e]	-		
				TX	N. A.[e]		N. A.[e]	-		
				TQ20	5.2 ± 0.06	1.0 ± 0.02	0.9 ± 0.01	-	10.3	897
				TQ40	6.5 ± 0.05	1.3 ± 0.02	0.9 ± 0.01	-	9.9	897
Halo-R110	Inside	Live	21	-	4.8 ± 0.03	1.0 ± 0.01	1.0 ± 0.04	32.5	11.2	897
				TX	7.5 ± 0.05	1.5 ± 0.01	0.9 ± 0.01	-	9.0	897
				TQ20	3.7 ± 0.02	0.8 ± 0.02	1.0 ± 0.01	-	9.4	897
				TQ40	1.7 ± 0.01	0.4 ± 0.01	0.9 ± 0.02	-	4.1	897
			2	-	4.9 ± 0.01	1.0 ± 0.01	0.9 ± 0.02	-	10.0	897
				TX	6.9 ± 0.12	1.4 ± 0.03	0.9 ± 0.02	-	15.4	1497
				TQ20	1.9 ± 0.02	0.4 ± 0.01	1.1 ± 0.01	-	3.1	1497
				TQ40	1.6 ± 0.05	0.3 ± 0.01	1.1 ± 0.01	-	2.6	897
			0	-	N. A.[e]		N. A.[e]	-		
				TX	N. A.[e]		N. A.[e]	-		
				TQ20	5.8 ± 0.10	1.2 ± 0.02	1.0 ± 0.01	-	4.7	897
				TQ40	5.7 ± 0.06	1.2 ± 0.01	1.1 ± 0.02	-	5.8	897

To be continued

Tag protein-Dye	Outside/ Inside the cell	Live/ Fixed cells	O$_2$ (%)	ROXS	Photobleaching lifetime (s)[a]	Relative prolongation (fold)[a]	Relative intensity (fold)[b]	Precision (nm)	N (x10^4)	v[d]
Halo-AL488	Outside	Live	21	-	2.4 ± 0.01	1.0 ± 0.02	1.0 ± 0.01	26.7	6.7	897
				TX	4.2 ± 0.04	1.8 ± 0.02	1.1 ± 0.02	-	8.7	897
				TQ20	N. A.[e]		N. A.[e]	-		
				TQ40	N. A.[e]		N. A.[e]	-		
			2	-	2.3 ± 0.08	0.9 ± 0.03	0.9 ± 0.01	-	1.6	897
				TX	4.9 ± 0.09	2.1 ± 0.04	1.2 ± 0.01	-	9.8	897
				TQ20	N. A.[e]		N. A.[e]	-		
				TQ40	N. A.[e]		N. A.[e]	-		
			0	-	N. A.[e]		N. A.[e]	-		
				TX	N. A.[e]		N. A.[e]	-		
				TQ20	N. A.[e]		N. A.[e]	-		
				TQ40	N. A.[e]		N. A.[e]	-		
ACP-AT488	Outside	Live	21	-	2.8 ± 0.02	1.0 ± 0.01	1.0 ± 0.01	27.6	4.7	1497
				TX	2.9 ± 0.02	1.0 ± 0.01	1.1 ± 0.01	-	9.9	1497
				TQ20	4.5 ± 0.06	1.6 ± 0.03	1.2 ± 0.01	-	6.5	1497
				TQ40	2.4 ± 0.05	0.9 ± 0.02	1.0 ± 0.01	-	4.6	1497
			2	-	2.0 ± 0.03	0.7 ± 0.01	1.0 ± 0.01	-	2.8	1497
				TX	2.9 ± 0.03	1.0 ± 0.01	0.9 ± 0.01	-	5.4	1497
				TQ20	12.4 ± 0.35	4.4 ± 0.13	0.9 ± 0.01	-	19.1	1497
				TQ40	4.8 ± 0.05	1.7 ± 0.02	0.9 ± 0.01	-	3.8	1497
			0	-	N. A.[e]		N. A.[e]	-		
				TX	N. A.[e]		N. A.[e]	-		
				TQ20	5.7 ± 0.14	2.0 ± 0.05	1.0 ± 0.01	-	11.7	1497
				TQ40	6.3 ± 0.06	2.2 ± 0.03	1.1 ± 0.01	-	11.5	1497
Halo-TMR	Outside	Live	21	-	5.1 ± 0.03	1.0 ± 0.01	1.0 ± 0.02	24.7	7.5	1497
				TX	12.7 ± 0.04	2.5 ± 0.02	1.0 ± 0.01	-	19.5	1497
				TQ20	7.1 ± 0.10	1.4 ± 0.02	1.0 ± 0.01	-	13.3	1497
				TQ40	5.0 ± 0.14	1.0 ± 0.03	0.9 ± 0.01	-	6.5	1497
			10	-	3.7 ± 0.03	0.7 ± 0.01	0.9 ± 0.01	-	7.5	1497
				TX	13.4 ± 0.09	2.6 ± 0.02	1.0 ± 0.01	-	19.2	1497
				TQ20	9.1 ± 0.15	1.8 ± 0.03	1.0 ± 0.01	-	15.4	1497
				TQ40	7.6 ± 0.01	1.5 ± 0.01	0.9 ± 0.01	-	7.7	1497
			5	-	4.4 ± 0.11	0.9 ± 0.02	0.8 ± 0.01	-	9.3	1497
				TX	18.2 ± 0.11	3.6 ± 0.03	0.9 ± 0.01	-	34.4	1497
				TQ20	9.6 ± 0.35	1.9 ± 0.07	1.0 ± 0.01	-	23.8	1497
				TQ40	7.8 ± 0.21	1.5 ± 0.04	0.9 ± 0.01	-	16.8	1497

To be continued

Tag protein-Dye	Outside/ Inside the cell	Live/ Fixed cells	O_2 (%)	ROXS	Photobleaching lifetime (s)[a]	Relative prolongation (fold)[a]	Relative intensity (fold)[b]	Precision (nm)	N (x10^4)	ν[d]
Halo-TMR	Outside	Live	2	-	3.8 ± 0.02	0.5 ± 0.01	0.7 ± 0.02	-	3.8	1497
				TX	31.0 ± 0.47	6.1 ± 0.10	0.9 ± 0.01	25.8	40.3	1497
				TQ20	17.4 ± 0.27	3.4 ± 0.06	1.0 ± 0.01	-	21.1	1497
				TQ40	11.6 ± 0.21	2.3 ± 0.04	1.0 ± 0.01	-	20.4	1497
			0	-	N. A.[e]		N. A.[e]	-		
				TX	N. A.[e]		N. A.[e]	-		
				TQ20	9.5 ± 0.21	1.9 ± 0.04	0.8 ± 0.01	-	20.0	1497
				TQ40	17.3 ± 0.10	3.4 ± 0.03	0.8 ± 0.01	-	34.4	1497
Halo-TMR	Outside	Fixed	21	-	4.6 ± 0.11	1.0 ± 0.03	1.0 ± 0.01	24.7	7.7	1497
			21	TX	12.2 ± 0.27	2.6 ± 0.05	1.0 ± 0.01		24.1	1497
			2	TX	29.1 ± 0.50	6.3 ± 0.19	0.9 ± 0.01	25.8	53.5	1497
			0	TX	N. A.[e]		N. A.[e]			
Halo-TMR	Inside	Live	21	-	5.3 ± 0.02	1.0 ± 0.01	1.0 ± 0.01	24.7	9.4	1497
				TX	6.5 ± 0.09	1.4 ± 0.02	1.0 ± 0.01	-	10.2	1497
				TQ20	7.3 ± 0.03	1.6 ± 0.01	1.0 ± 0.01	-	8.7	1497
				TQ40	3.4 ± 0.07	0.7 ± 0.01	1.0 ± 0.01	-	5.2	1497
			10	-	4.0 ± 0.04	0.9 ± 0.01	0.9 ± 0.01	-	8.9	1497
				TX	13.6 ± 0.18	2.9 ± 0.04	0.9 ± 0.02	-	23.5	1497
				TQ20	13.7 ± 0.35	3.0 ± 0.07	0.9 ± 0.01	-	25.2	1497
				TQ40	7.2 ± 0.04	1.6 ± 0.01	0.8 ± 0.01	-	15.0	1497
			5	-	4.5 ± 0.05	1.0 ± 0.01	0.9 ± 0.01	-	8.2	1497
				TX	12.0 ± 0.13	2.6 ± 0.03	0.9 ± 0.01	-	14.4	1497
				TQ20	13.7 ± 0.16	3.0 ± 0.03	1.0 ± 0.01	-	23.4	1497
				TQ40	10.6 ± 0.11	2.3 ± 0.01	1.1 ± 0.02	-	19.3	1497
			2	-	3.6 ± 0.04	0.8 ± 0.02	0.9 ± 0.01	-	6.9	1497
				TX	32.4 ± 0.37	7.0 ± 0.08	0.9 ± 0.02	25.8	55.6	1497
				TQ20	26.1 ± 0.65	5.7 ± 0.12	0.9 ± 0.01	-	51.2	1497
				TQ40	16.1 ± 0.34	3.5 ± 0.07	0.9 ± 0.01	-	25.2	1497
			0	-	N. A.[e]		N. A.[e]	-		
				TX	N. A.[e]		N. A.[e]	-		
				TQ20	13.5 ± 0.27	2.9 ± 0.01	0.9 ± 0.02	-	36.0	1497
				TQ40	18.3 ± 0.29	4.0 ± 0.01	0.9 ± 0.01	-	33.7	1497
ACP-TMR	Outside	Live	21	-	1.8 ± 0.04	1.0 ± 0.05	1.0 ± 0.02	-	5.0	497
			2	TX	4.1 ± 0.05	2.3 ± 0.06	1.0 ± 0.01	-	10.4	497

Tag protein-Dye	Outside/ Inside the cell	Live/ Fixed cells	O_2 (%)	ROXS	Photobleaching lifetime (s)[a]	Relative prolongation (fold)[a]	Relative intensity (fold)[b]	Precision (nm)	N (x10^4)	ν[d]
ACP-DY547	Outside	Live	21	-	1.5 ± 0.01	1.0 ± 0.04	1.0 ± 0.01	30.0	4.4	597
				TX	1.1 ± 0.01	0.7 ± 0.04	1.1 ± 0.01	-	1.7	597
				TQ20	1.3 ± 0.04	0.9 ± 0.05	1.2 ± 0.01	-	2.1	597
				TQ40	1.5 ± 0.03	1.0 ± 0.04	1.2 ± 0.01	-	3.9	597
			2	-	1.8 ± 0.04	1.2 ± 0.04	1.1 ± 0.01	-	5.2	597
				TX	3.2 ± 0.01	2.1 ± 0.06	1.3 ± 0.01	-	3.2	597
				TQ20	1.8 ± 0.01	1.2 ± 0.05	1.1 ± 0.01	-	3.4	597
				TQ40	2.2 ± 0.01	1.5 ± 0.05	1.1 ± 0.01	-	2.4	597
			0	-	N. A.[e]		N. A.[e]	-		
				TX	N. A.[e]		N. A.[e]	-		
				TQ20	N. A.[e]		N. A.[e]	-		
				TQ40	N. A.[e]		N. A.[e]	-		
ACP-AT594	Outside	Live	21	-	9.2 ± 0.01	1.0 ± 0.01	1.0 ± 0.02	26.1	14.0	1497
				TX	7.7 ± 0.17	0.8 ± 0.02	0.8 ± 0.01	-	13.4	1497
				TQ20	12.8 ± 0.16	1.4 ± 0.02	1.2 ± 0.01	-	32.5	1497
				TQ40	6.7 ± 0.25	0.7 ± 0.03	1.2 ± 0.02	-	12.5	1497
			10	-	8.4 ± 0.17	0.9 ± 0.02	1.1 ± 0.01	-	7.1	1497
				TX	8.8 ± 0.23	1.0 ± 0.03	1.0 ± 0.01	-	14.0	1497
				TQ20	8.8 ± 0.38	1.0 ± 0.04	1.1 ± 0.02	-	27.7	1497
				TQ40	19.0 ± 0.31	2.1 ± 0.03	1.0 ± 0.01	-	35.5	1497
			5	-	7.7 ± 0.09	0.8 ± 0.01	1.0 ± 0.01	-	18.6	1497
				TX	7.9 ± 0.05	0.9 ± 0.01	0.9 ± 0.02	-	9.4	1497
				TQ20	13.7 ± 0.08	1.5 ± 0.02	1.0 ± 0.01	-	31.2	1497
				TQ40	15.8 ± 0.17	1.7 ± 0.01	1.1 ± 0.01	-	44.0	1497
			2	-	6.7 ± 0.06	0.7 ± 0.01	0.9 ± 0.02	-	11.9	1497
				TX	6.1 ± 0.11	0.7 ± 0.01	0.8 ± 0.01	-	18.2	1497
				TQ20	14.9 ± 0.39	1.6 ± 0.04	1.2 ± 0.02	-	17.6	1497
				TQ40	25.3 ± 0.25	2.8 ± 0.03	1.2 ± 0.02	-	53.8	1497
			0	-	N. A.[e]		N. A.[e]	-		
				TX	N. A.[e]		N. A.[e]	-		
				TQ20	18.6 ± 0.20	2.0 ± 0.02	1.0 ± 0.01	-		
				TQ40	20.8 ± 0.30	2.3 ± 0.03	1.0 ± 0.01	-		
Halo-AT594	Outside	Live	21	-	8.6 ± 0.21	1.0 ± 0.03	1.0 ± 0.01	-	37	1497
			2	TQ40	24.8 ± 0.46	2.9 ± 0.09	1.2 ± 0.02	-	64	1497

Tag protein-Dye	Outside/ Inside the cell	Live/ Fixed cells	O$_2$ (%)	ROXS	Photobleaching lifetime (s)[a]	Relative prolongation (fold)[a]	Relative intensity (fold)[b]	Precision (nm)	N (x10^4)	v[d]
ACP-DY647	Outside	Live	21	-	1.9 ± 0.02	1.0 ± 0.02	1.0 ± 0.01	30.0	4.5	597
				TX	0.7 ± 0.03	0.4 ± 0.02	1.1 ± 0.01	-	1.1	597
				TQ20	1.1 ± 0.01	0.6 ± 0.01	1.1 ± 0.02	-	1.9	597
				TQ40	1.2 ± 0.03	0.6 ± 0.02	1.1 ± 0.01	-	1.3	597
			2	-	1.8 ± 0.03	1.0 ± 0.02	1.0 ± 0.02	-	2.8	597
				TX	2.2 ± 0.03	1.2 ± 0.02	1.1 ± 0.02	-	5.6	597
				TQ20	7.0 ± 0.17	3.8 ± 0.11	1.1 ± 0.02	-	14.2	597
				TQ40	6.6 ± 0.23	3.6 ± 0.13	1.2 ± 0.02	-	10.3	597
			0	-	N. A.[e]		N. A.[e]	-		
				TX	N. A.[e]		N. A.[e]	-		
				TQ20	31.7 ± 0.46	17.1 ± 0.34	0.9 ± 0.01	-		1497
				TQ40	33.6 ± 0.40	18.1 ± 0.32	0.7 ± 0.02	-	64.9	1497
									52.9	
ACP-AT647N	Outside	Live	21	-	9.5 ± 0.17	1.0 ± 0.03	1.0 ± 0.02	30.1	22.1	1497
				TX	6.7 ± 0.05	0.7 ± 0.01	1.0 ± 0.01	-	19.6	1497
				TQ20	8.8 ± 0.21	0.9 ± 0.03	1.0 ± 0.01	-	20.3	1497
				TQ40	8.9 ± 0.07	0.9 ± 0.02	1.1 ± 0.02	-	11.0	1497
			2	-	10.8 ± 0.16	1.1 ± 0.03	1.0 ± 0.01	-	26.3	1497
				TX	5.8 ± 0.04	0.6 ± 0.01	0.8 ± 0.01	-	15.1	1497
				TQ20	51.5 ± 1.37	5.4 ± 0.17	1.3 ± 0.01	-	73.1	2997
				TQ40	27.3 ± 0.90	2.9 ± 0.11	1.2 ± 0.01	-	41.7	2997
			0	-	N. A.[e]		N. A.[e]	-		
				TX	N. A.[e]		N. A.[e]	-		
				TQ20	35.1 ± 0.89	3.7 ± 0.11	1.3 ± 0.04	-	76.8	2997
				TQ40	13.8 ± 0.28	1.5 ± 0.04	1.1 ± 0.01	-	31.9	2997
ACP-ST647	Outside	Live	21	-	16.2 ± 0.06	1.0 ± 0.01	1.0 ± 0.02	23.0	25.2	5997
				TX	26.0 ± 0.03	1.6 ± 0.01	1.0 ± 0.01	-	34.4	5997
				TQ20	39.6 ± 0.69	2.4 ± 0.04	1.1 ± 0.03	-	29.5	5997
				TQ40	41.7 ± 0.62	2.6 ± 0.04	1.0 ± 0.01	-	52.3	5997
			2	-	23.4 ± 0.09	1.4 ± 0.01	1.1 ± 0.02	-	56.1	5997
				TX	61.1 ± 1.01	3.8 ± 0.06	1.0 ± 0.02	-	63.1	5997
				TQ20	105.8 ± 0.78	6.5 ± 0.05	1.4 ± 0.01	21.5	269.8	5997
				TQ40	72.1 ± 0.70	4.5 ± 0.05	1.2 ± 0.01	-	139.4	5997
			0	-	N. A.[e]		N. A.[e]	-		
				TX	N. A.[e]		N. A.[e]	-		
				TQ20	33.5 ± 0.12	2.1 ± 0.01	1.3 ± 0.01	-	74.6	5997
				TQ40	38.5 ± 0.18	2.4 ± 0.01	1.1 ± 0.01	-	56.8	5997

To be continued

Tag protein-Dye	Outside/ Inside the cell	Live/ Fixed cells	O_2 (%)	ROXS	Photobleaching lifetime (s)[a]	Relative prolongation (fold)[a]	Relative intensity (fold)[b]	Precision (nm)	N (x10⁴)	ν[d]
Halo-ST647	Outside	Live	21	-	17.8 ± 0.09	1.0 ± 0.01	1.0 ± 0.01	-	25.4	5997
			2	TQ20	107.1 ± 0.59	6.0 ± 0.05	1.3 ± 0.02	-	178.3	5997
ACP-ST647	Outside	Fixed	21	-	15.5 ± 0.11	1.0 ± 0.01	1.0 ± 0.01	23.0	33.6	5997
			21	TQ20	42.1 ± 0.66	2.7 ± 0.05	1.1 ± 0.01	-	106.8	5997
			2	TQ20	99.0 ± 1.57	6.4 ± 0.11	1.4 ± 0.01	21.5	120.8	5997
			0	TQ20	47.2 ± 1.30	3.0 ± 0.09	1.3 ± 0.02	-	91.7	5997
Halo-TMR-TX	Outside	Live	21	-	4.0 ± 0.08	1.0 ± 0.01	0.9 ± 0.01	26.5	4.9	997
			10	-	4.4 ± 0.11	1.1 ± 0.02	0.9 ± 0.01	-	10.1	997
			5	-	3.5 ± 0.05	0.9 ± 0.01	0.9 ± 0.01	-	5.6	997
			2	-	3.4 ± 0.05	0.8 ± 0.01	0.9 ± 0.01	27.3	3.9	997
			0	-	6.5 ± 0.10	1.6 ± 0.02	0.8 ± 0.01	28.4	17.3	997
ACP-AT594-TX	Outside	Live	21	-	13.1 ± 0.07	1.0 ± 0.01	0.9 ± 0.01	27.4	28.1	1497
			10	-	13.8 ± 0.21	1.0 ± 0.02	0.8 ± 0.01	-	19.1	1497
			5	-	18.8 ± 0.18	1.4 ± 0.02	0.8 ± 0.01	-	42.1	1497
			2	-	39.3 ± 0.70	3.0 ± 0.06	0.7 ± 0.01	28.7	25.4	1497
			0	-	30.4 ± 0.57	2.3 ± 0.04	0.9 ± 0.01	-	50.1	1497
Halo-Cy3-TX	Outside	Live	21	-	1.7 ± 0.02	1.0 ± 0.02	1.0 ± 0.01	22.2	3.1	997
			10	-	2.6 ± 0.06	1.5 ± 0.04	1.0 ± 0.01	-	3.4	997
			5	-	2.7 ± 0.05	1.6 ± 0.04	1.1 ± 0.01	-	6.9	997
			2	-	4.1 ± 0.08	2.4 ± 0.06	0.9 ± 0.01	23.8	11.4	997
			0	-	3.0 ± 0.02	1.7 ± 0.03	0.9 ± 0.01	-	3.1	997
Halo-Cy5-TX	Outside	Live	21	-	0.7 ± 0.01	1.0 ± 0.01	1.0 ± 0.02	25.1	0.8	5997
			10	-	2.5 ± 0.07	3.6 ± 0.11	1.0 ± 0.01	-	3.8	5997
			5	-	17.2 ± 0.52	25.4 ± 0.78	0.9 ± 0.01	-	28	5997
			2	-	40.3 ± 0.44	59.5 ± 0.69	0.9 ± 0.01	26.3	101.6	5997
			0	-	42.8 ± 0.36	63.2 ± 0.59	0.9 ± 0.01	26.7	68.5	5997

[a]The photobleaching lifetime (exponential decay time constant [= mean] ± the standard error) obtained by counting the number of fluorescent spots in each frame followed by the fitting with a single exponential function (see **Online Methods**).

^bThe fluorescence intensities (the mode values ± the standard errors) obtained by the log-normal curve fitting (see **Supplementary Fig. 6b** and its caption for the detailed method).

^cThe total numbers of fluorescent spots detected in all video frames in six independent movies.

^dThe degree of freedom for curve fitting ([the number of bins] − [the number of free parameters for fitting]).

^dNot analyzed due to extensive blinking ("ON" times mostly less than 66 ms; see **Online Methods**).

Supplementary Table 2 | Summary of TALL lifetimes ($\tau_1 = 1/k_{M,1}$, $\tau_2 = 1/k_{M,2}$, and $\tau_3 = 1/k_{M,3}$ with a $1/k_B$ of 83.5 s), time fractions against the total TALL period, and total numbers of cells and TALL events examined. The cover glasses used for culturing/observing cells were coated with fibronectin except for the specimens shown as "+ VN" (vitronectin coating).

a. Inside FA

	TALL lifetime (s) (time fraction [%])[a]			# of observed cells	# of observed TALLs	# of shorter TALLs	# of longer TALLs	ν[b]
	τ_1	τ_2	τ_3					
Itg β1 (WT)	0.51 ± 0.013 (6)	4.3 ± 0.46 (12)	43 ± 5.1 (82)	22	1155	785	370	294
Itg β1 (WT) + Mn^{2+}	0.79 ± 0.021 (8)	5.2 ± 0.82 (16)	40 ± 6.4 (76)	21	1250	918	332	294
Itg β1 (D130A)	0.65 ± 0.0060 (27)	5.7 ± 0.15 (73)	– (0)	25	1192	1025	169	296
Itg β1 (Y783A/Y795A)	0.48 ± 0.080 (33)	4.7 ± 0.21 (67)	– (0)	30	587	521	66	296
Itg β1 (D130AY783A/Y795A)	0.24 ± 0.012 (81)	1.3 ± 0.073 (19)	– (0)	25	452	430	22	296
Itg β1 (WT) + 2 µM Y27632	0.40 ± 0.019 (8)	2.3 ± 0.16 (15)	19 ± 2.0 (77)	28	1145	865	280	294
Itg β1 (WT) + 10 µM Y27632	0.52 ± 0.0070 (25)	4.3 ± 0.10 (75)	– (0)	26	1437	1245	192	296
Itg β1 (WT) + VN	0.38 ± 0.015 (19)	6.0 ± 0.33 (81)	– (0)	33	606	488	118	296
Itg β3 (WT)	0.66 ± 0.016 (2)	9.4 ± 1.5 (13)	79 ± 10 (85)	33	1376	909	467	294
Itg β3 (WT) + Mn^{2+}	0.61 ± 0.022 (2)	6.2 ± 1.7 (4)	87 ± 10 (94)	47	921	529	309	294
Itg β3 (N305T)	0.66 ± 0.16 (6)	8.4 ± 1.1 (11)	99 ± 11 (88)	39	1093	724	369	294
Itg β3 (WT) + 2 µM Y27632	0.67 ± 0.015 (6)	7.7 ± 1.5 (16)	67 ± 12 (78)	45	1052	831	221	294
Itg β3 (WT) + 10 µM Y27632	0.46 ± 0.010 (17)	6.7 ± 0.26 (83)	– (0)	39	998	880	118	296
Itg β3 (WT) + VN	0.68 ± 0.0098 (8)	6.3 ± 1.1 (11)	50 ± 6.7 (81)	41	1415	1154	261	294

b. Outside FA

	TALL lifetime (s) (time fraction [%])[a]			# of observed cells	# of observed TALLs	# of shorter TALLs	# of longer TALLs	ν[b]
	τ_1	τ_2	τ_3					
Itg β1 (WT)	0.35 ± 0.0051 (26)	2.0 ± 0.095 (16)	20 ± 2.3 (58)	22	4595	N.D.[c]	N.D.	294
Itg β1 (WT) + Mn^{2+}	0.36 ± 0.0066 (23)	1.6 ± 0.060 (17)	15 ± 1.0 (60)	21	3986	N.D.	N.D.	294
Itg β1 (D130A)	0.38 ± 0.0041 (45)	2.4 ± 0.039 (55)	– (0)	25	4115	N.D.	N.D.	296
Itg β1 (Y783A/Y795A)	0.33 ± 0.0026 (51)	2.6 ± 0.033 (49)	– (0)	30	2831	N.D.	N.D.	296
Itg β1 (D130AY783A/Y795A)	0.40 ± 0.0030 (61)	3.0 ± 0.087 (39)	– (0)	25	1815	N.D.	N.D.	296
Itg β1 (WT) + 2 µM Y27632	0.36 ± 0.0066 (26)	1.3 ± 0.040 (23)	8.0 ± 0.39 (51)	28	5451	N.D.	N.D.	294
Itg β1 (WT) + 10 µM Y27632	0.48 ± 0.0035 (46)	2.8 ± 0.050 (54)	– (0)	26	5267	N.D.	N.D.	296
Itg β1 (WT) + VN	0.47 ± 0.0080 (34)	4.3 ± 0.18 (49)	– (0)	33	2260	N.D.	N.D.	296
Itg β3 (WT)	0.76 ± 0.015 (10)	3.4 ± 0.59 (8)	21 ± 1.9 (82)	33	2656	N.D.	N.D.	294
Itg β3 (WT) + Mn^{2+}	0.43 ± 0.010 (6)	2.6 ± 0.11 (9)	61 ± 4.2 (85)	47	2471	N.D.	N.D.	294
Itg β3 (N305T)	0.35 ± 0.0074 (9)	2.1 ± 0.10 (7)	31 ± 2.0 (84)	39	2548	N.D.	N.D.	294
Itg β3 (WT) + 2 µM Y27632	0.47 ± 0.0060 (18)	2.3 ± 0.13 (13)	20 ± 1.6 (69)	45	3505	N.D.	N.D.	294
Itg β3 (WT) + 10 µM Y27632	0.35 ± 0.0053 (23)	1.8 ± 0.061 (19)	14 ± 0.91 (58)	39	4072	N.D.	N.D.	294
Itg β3 (WT) + VN	0.55 ± 0.0049 (23)	3.6 ± 0.34 (17)	21 ± 3.7 (66)	41	2194	N.D.	N.D.	294

[a]Exponential decay time constant (= mean ± the standard error).

[b]The degree of freedom for curve fitting ([the number of bins] − [the number of free parameters for fitting]).

[c]N.D. : Not determined.

Supplementary Table 3 | Summary of Akaike's and Baysian information criteria (AIC and BIC, respectively) for the fitting of TALL lifetimes (**Supplementary Table 2**), using a sum of 1, 2, 3, and 4 exponential functions (single, double, triple, and quadruple expo.). For *n*, see **Supplementary Table 2**.

a. Inside FA

	Information criteria (AIC, BIC)							
	single expo.		double expo.		triple expo.		quadruple expo.	
Itg β1 (WT)	128	139	−374	−356	−448	−415	−415	−448
Itg β1 (WT) + Mn^{2+}	165	176	−421	−402	−534	−501	−511	−485
Itg β1 (D130A)	−54	−43	−1018	−989	−1005	−972	−999	−973
Itg β1 (Y783A/Y795A)	−49	−38	−671	−633	−644	−618	−644	−617
Itg β1 (D130AY783A/Y795A)	−523	−511	−1020	−998	−943	−971	−379	−346
Itg β1 (WT) + 2 µM Y27632	208	220	−411	−392	−611	−585	−607	−574
Itg β1 (WT) + 10 µM Y27632	50	61	−846	−828	−924	−898	−919	−886
Itg β1 (WT) + VN	−307	−318	−185	−167	−194	−162	−181	−155
Itg β3 (WT)	453	464	−211	−192	−265	−239	−261	−228
Itg β3 (WT) + Mn^{2+}	344	355	−90	−71	−121	−95	−152	−119
Itg β3 (N305T)	395	407	−217	−199	−291	−265	−303	−271
Itg β3 (WT) + 2 µM Y27632	126	137	−335	−317	−356	−330	−411	−378
Itg β3 (WT) + 10 µM Y27632	222	233	−621	−599	−607	−581	−603	−570
Itg β3 (WT) + VN	−27	−16	−606	−588	−650	−624	−650	−617

b. Outside FA

	Information criteria (AIC, BIC)							
	single expo.		double expo.		triple expo.		quadruple expo.	
Itg β1 (WT)	−246	−236	−1004	−985	−1228	−1202	−1223	−1190
Itg β1 (WT) + Mn^{2+}	−196	−185	−964	−945	−1377	−1344	−1314	−1288
Itg β1 (D130A)	−187	−176	−1321	−1299	−1295	−1262	−1268	−1242
Itg β1 (Y783A/Y795A)	−173	−161	−1445	−1421	−1436	−1409	−1431	−1398
Itg β1 (D130AY783A/Y795A)	−472	−460	−1335	−1316	−1312	−1286	−1291	−1258
Itg β1 (WT) + 2 µM Y27632	−193	−182	−1122	−1103	−1610	−1584	−1675	−1642
Itg β1 (WT) + 10 µM Y27632	−292	−281	−1362	−1344	−1543	−1510	−1533	−1507
Itg β1 (WT) + VN	−72	−60	−675	−656	−886	−860	−882	−849
Itg β3 (WT)	66	77	−758	−740	−837	−812	−833	−800
Itg β3 (WT) + Mn^{2+}	19	31	−553	−535	−864	−838	−859	−826
Itg β3 (N305T)	24	35	−605	−586	−1025	−991	−1007	−974
Itg β3 (WT) + 2 µM Y27632	−187	−176	−972	−954	−1350	−1317	−1229	−1203
Itg β3 (WT) + 10 µM Y27632	−136	−125	−987	−968	−1382	−1349	−1363	−1337
Itg β3 (WT) + VN	−305	−294	−1094	−1076	−1192	−1166	−1187	−1154

Supplementary Table 4 | Summary of % time fractions (against the sum of the observation periods for all of the molecules, T_{total}; Mean ± SEM. For n, see **Supplementary Table 2**). The cover glasses used for culturing/observing cells were coated with fibronectin except for the specimens shown as "+ VN" (vitronectin coating).

a. Inside FA

	$f_{Exp\text{AATI}}$ (%)[a]	f_{AATI} (%)[b]	f_{MLI} (%)[c]	True TALL (%)[d]
Itg β1 (WT)	9.6 ± 1.7	8.6 ± 2.8	0.99 ± 3.3	78 ± 4.9
Itg β1 (WT) + Mn^{2+}	10.8 ± 1.7	8.3 ± 3.9	2.6 ± 4.3	89 ± 2.6
Itg β1 (D130A)	1.5 ± 1.9	0.14 ± 0.022	1.4 ± 1.9	39 ± 5.9
Itg β1 (Y783A/Y795A)	0.53 ± 2.0	0.077 ± 0.017	0.45 ± 2.0	32 ± 6.3
Itg β1 (D130AY783A/Y795A)	1.5 ± 1.5	0.0017 ± 0.00060	1.5 ± 1.4	13 ± 4.6
Itg β1 (WT) + 2 µM Y27632	0.72 ± 1.6	2.3 ± 0.43	−1.6 ± 1.6	76 ± 4.9
Itg β1 (WT) + 10 µM Y27632	2.5 ± 1.2	0.12 ± 0.0098	2.4 ± 1.2	54 ± 3.8
Itg β1 (WT) + VN	0.74 ± 3.3	0.25 ± 0.037	0.50 ± 3.3	56 ± 5.6
Itg β3 (WT)	20 ± 4.0	18 ± 7.6	2.0 ± 8.6	83 ± 9.3
Itg β3 (WT) + Mn^{2+}	26 ± 1.7	25 ± 9.3	1.1 ± 9.4	95 ± 10
Itg β3 (N305T)	26 ± 2.3	27 ± 11	-1.2 ± 12	95 ± 13
Itg β3 (WT) + 2 µM Y27632	12 ± 4.3	13 ± 9.5	−0.72 ± 10.4	75 ± 11
Itg β3 (WT) + 10 µM Y27632	1.1 ± 1.5	0.32 ± 0.036	0.74 ± 1.5	58 ± 4.9
Itg β3 (WT) + VN	15 ± 1.8	11 ± 4.4	3.4 ± 4.7	88 ± 6.6

b. Outside FA

	$f_{Exp\text{AATI}}$ (%)[a]	f_{AATI} (%)[b]	f_{MLI} (%)[c]	True TALL (%)[d]
Itg β1 (WT)	3.2 ± 1.4	1.4 ± 0.34	1.8 ± 1.4	51 ± 4.4
Itg β1 (WT) + Mn^{2+}	2.0 ± 1.1	1.2 ± 0.16	0.87 ± 1.1	64 ± 3.3
Itg β1 (D130A)	0.86 ± 1.3	0.013 ± 0.0025	0.85 ± 1.3	21 ± 4.0
Itg β1 (Y783A/Y795A)	0.36 ± 1.5	0.018 ± 0.0034	0.34 ± 1.5	25 ± 4.7
Itg β1 (D130AY783A/Y795A)	1.2 ± 1.0	0.0091 ± 0.0025	1.2 ± 1.0	13 ± 3.3
Itg β1 (WT) + 2 µM Y27632	0.99 ± 0.94	0.27 ± 0.024	0.72 ± 0.90	51 ± 3.0
Itg β1 (WT) + 10 µM Y27632	0.81 ± 1.3	0.033 ± 0.0034	0.77 ± 1.3	42 ± 4.1
Itg β1 (WT) + VN	3.0 ± 0.94	0.061 ± 0.0071	3.0 ± 1.3	30 ± 2.4
Itg β3 (WT)	4.0 ± 1.3	1.5 ± 0.27	2.5 ± .3	40 ± 4.1
Itg β3 (WT) + Mn^{2+}	15 ± 0.98	13 ± 2.6	1.9 ± 2.8	76 ± 3.4
Itg β3 (N305T)	7.2 ± 0.49	4.1 ± 0.49	3.1 ± 0.70	56 ± 3.1
Itg β3 (WT) + 2 µM Y27632	1.5 ± 1.1	1.2 ± 0.20	0.34 ± 1.1	40 ± 3.5
Itg β3 (WT) + 10 µM Y27632	2.2 ± 1.4	0.53 ± 0.096	1.6 ± 1.4	34 ± 4.5
Itg β3 (WT) + VN	3.0 ± 1.3	0.061 ± 0.0071	3.0 ± 1.3	38 ± 3.2

[a]Time fractions of molecules (in %) that were experimentally and directly determined to be immobile at time 0 and photobleached before starting motion (% Time fraction of experimentally-observed apparent all-time immobile periods). See **Eq. 39** in **Supplementary Note 1**.

[b]Time fractions (in %) in which the observed molecules are expected to exhibit the AATI behavior (f_{AATI}) in the absence of "alternative molecules" undergoing immobilization for periods much longer than T_{rec} (**Eq. 44** in **Supplementary Note 1**), i.e., the time fraction calculated using the parameters determined by $G_{TALL}(\delta)$ (**Eq. 29** in **Supplementary Note 1**).

[c]f_{ExpATI} - f_{AATI}, representing the time fraction (in %) of "alternative molecules" exhibiting Much Longer Immobilization (molecules that are immobilized for periods much longer than T_{rec}). See **Eq. 39** in **Supplementary Note 1**. Note that this time fraction is much less than the immobile time fraction previously determined by FRAP[54-56], which was 55~67% in the time scale between 20-200 s. Since the longest τ_3 TALLs found here were 43 s (~15% time fraction) for integrin β1 and 79 s (~30% time fraction) for integrin β3 (**Supplementary Figs. 23 and 24**), they might have been counted as immobile fractions in FRAP observations. In addition, since three types of immobilization durations existed, the FRAP evaluation of immobile components might have been quite difficult.

[d]The time fraction of "True TALL" periods (against T_{total}), calculated as 100 − %Mobile − f_{MLII}.

Supplementary Table 5 | Summary of P values (two-sided Mann-Whitney U test) for the cell area (n = 20 cells) shown in **Supplementary Fig. 14**.

Integrin expression	ROXS conditions	Time after plating (min)			
		15	30	60	90
None	Control	-	-	-	-
	2%O_2	0.95	0.56	0.12	0.97
	2%O_2+TX	0.93	0.30	0.22	0.13
	2%O_2+TQ20	0.70	0.66	0.29	0.36
	2%O_2+TQ40	0.78	0.24	0.60	0.84
	0%O_2	1.6×10^{-4}	6.7×10^{-4}	6.0×10^{-4}	0.028
Itgβ1	Control	-	-	-	-
	2%O_2	0.14	0.19	0.31	0.54
	2%O_2+TX	0.93	0.71	0.12	0.70
	2%O_2+TQ20	0.73	0.97	0.086	0.56
	2%O_2+TQ40	0.056	0.64	0.82	0.86
	0%O_2	3.3×10^{-4}	1.0×10^{-4}	1.0×10^{-6}	4.1×10^{-6}
ACP-Itgβ1	Control	0.76	0.41	0.053	0.068
	2%O_2	0.90	0.51	0.22	0.12
	2%O_2+TX	0.064	0.44	0.95	0.81
	2%O_2+TQ20	0.37	0.25	0.84	0.80
	2%O_2+TQ40	0.80	0.68	0.46	0.98
ACP-Itgβ1(D130A)	Control	N.D.[a]	3.3×10^{-7}	3.9×10^{-8}	1.0×10^{-4}
ACP-Itgβ1(Y783A/Y795A)	Control	N.D.[a]	5.2×10^{-7}	3.9×10^{-8}	6.6×10^{-7}
ACP-Itgβ1(D130A/Y783A/Y795A)	Control	N.D.[a]	1.1×10^{-8}	6.8×10^{-10}	6.9×10^{-8}

[a]N.D. : Not determined because no data were obtained.

Supplementary Figures
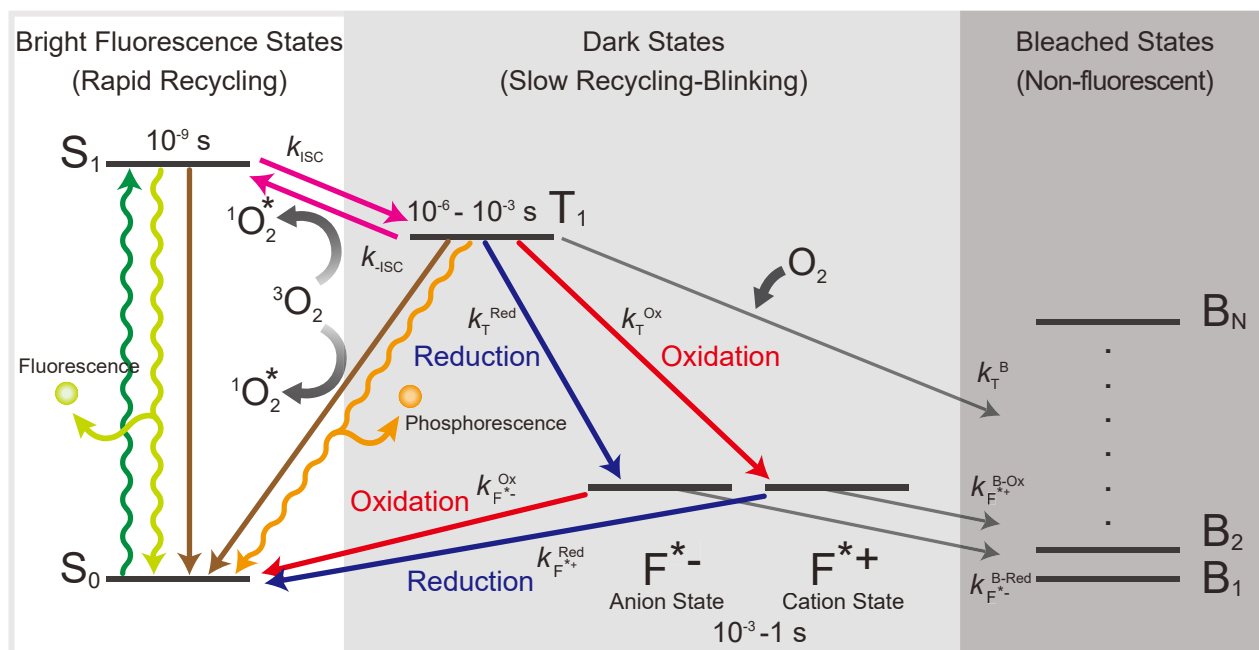
Supplementary Figure 1 | The effects of molecular oxygen and ROXS on the probabilities of transitions among various energy states of fluorescent molecules, schematically shown based on a Jablonski diagram.

Vibration-induced sublevels are omitted for clarity. The triplet state T_1 is considered to be most relevant to photobleaching. Fluorophores in the T_1 state often react with other compounds such as molecular oxygen to form non-fluorescent compounds, due to its higher energy and longer lifetime. This is the major cause of photobleaching.

During the continuous excitation of a fluorophore, it undergoes the excitation-deexcitation cycle, moving back and forth between the ground state S_0 and the excited singlet state S_1, and thus a single fluorescent molecule becomes observable because it emits many fluorescent photons during the integration time of the detector.

However, a fluorescent molecule in the excited state S_1 sometimes (with certain probabilities) transitions to the T_1 state and then to the ion states, F^{*-} and F^{*+}[57-59]. Since the lifetimes of these states are longer than that of S_1, often by a factor of a million or more, once a fluorescent molecule enters these states, it cannot be excited for long periods of time (and thus cannot emit any photons) until it relaxes to the ground state S_0. Therefore, these states are called dark states. When the fluorescent molecule finally returns back to the

ground state S_0, it can be excited again and resume the excitation-emission cycle. Namely, when a fluorescent dye molecule cycles between bright and dark periods, it blinks, and this phenomenon is called photoblinking[60-62].

In ROXS, both reducing and oxidizing reagents are included in the specimen, and the molecules in the T_1 state react with either the reducing or oxidizing reagent to transition to the ion states (F^{*-} or F^{*+}, respectively) and then are further oxidized or reduced, respectively, by the added reagent to return to the ground state S_0. In the ROXS experiments, there was generally no dissolved molecular oxygen present in the specimen[9].

In its ground state, molecular oxygen is in the triplet spin state. Therefore, it undergoes spin exchange reactions with the dye molecules in the T_1 state, bringing the dye molecules back to the ground state S_0 directly or indirectly by way of the excited singlet state S_1, but the reactive singlet molecular oxygen produced by the exchange reaction might in turn react with the dye molecule, inducing photobleaching of the dye molecule. Thus, the presence of molecular oxygen in the specimen could induce photobleaching of the dye molecule, but at the same time could reduce photobleaching by reducing the lifetime of T_1. Furthermore, molecular oxygen could participate in the oxidizing reactions of the dye (working as an oxidizing reagent in a ROX system). Therefore, if a good compromise of the dual functions of molecular oxygen (inducing and reducing photobleaching) by varying its concentrations (used together with the separately added ROXS), it would be desirable. Furthermore, for the research using living cells, because the cell, for its proper function, requires environmental molecular oxygen concentrations in the range between 1 and 13%[18-20] (for cells in culture, 2% is better than 21%[12]), molecular oxygen should be present in the medium for fluorescence observations. Therefore, we set out to find the dyes and the observation conditions (ROXS + proper oxygen concentrations) that can allow us to observe fluorescence molecules in living cells as long as possible.

Supplementary Figure 2| Schematic diagram showing the equilibrium of mobile (non-bleached), immobile (TALL; non-bleached), and bleached (mobile and TALL) states, with the kinetic rate constants for the transitions between these states. The final objective is to develop a theory to evaluate k_M (and k_I) from the results obtained by single fluorescent-molecule imaging.
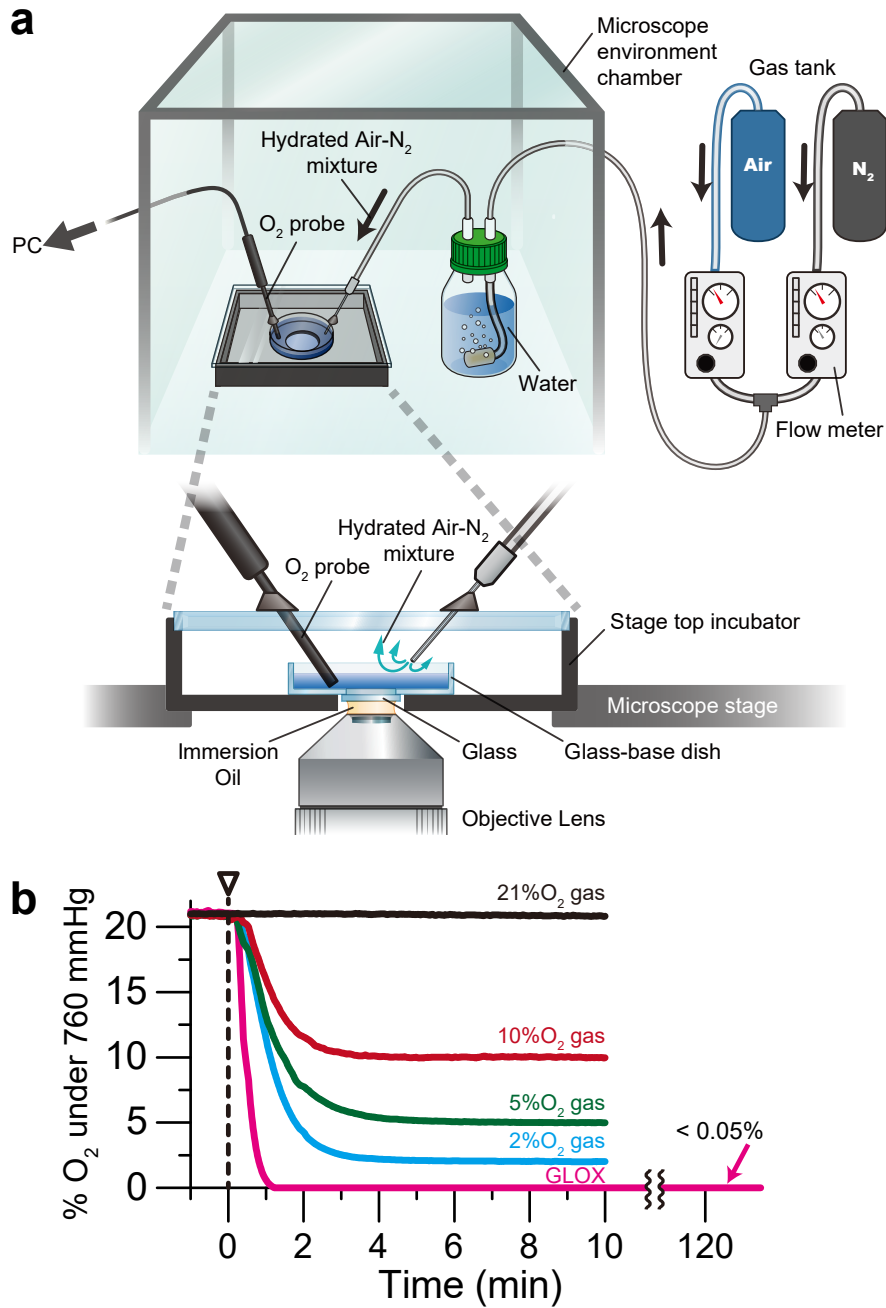
Supplementary Figure 3 | The set up to control the dissolved oxygen concentrations in the cell culture medium in the glass-base dish (the cells were cultured on the cover-glass bottom of this dish) placed on the microscope stage in the gas-environment chamber (**a**), and the time course of the decrease of the dissolved O_2 concentration in the cell culture medium when the injected gas mixture was changed from normal air to an air-nitrogen mixture (**b**). 0% O_2 (below the sensor's detection limit of 0.05% O_2) was achieved enzymatically, using the GLOX buffer.

(a) Schematic figure showing the set up to control the gas-environment and the temperature of cells cultured in the glass-base dish during the microscope observations. In a home-built microscope environment chamber made of thermo- and electric-field-insulating plastic, which covers the entire microscope except for the excitation arm and the detection arms, and contains three heating circulators, an additional smaller chamber was placed on the microscope stage, for further stabilization of the specimen temperature and for varying the partial pressure of molecular oxygen in the gas surrounding the specimen. The bottom plane of the chamber has a hole in which a glass-base dish can be placed snugly, so air escapes from there only slowly. On the lid of this chamber, two small holes allow access for the tubing for injecting the humidified gas mixture and for placing the micro-electrode for monitoring the dissolved oxygen concentrations. The N_2 gas and air (79% N_2 + 21% O_2) were supplied from each tank and mixed with a multi gas mixer with flow meters. The gas mixture was humidified by passage through a bottle filled with ultrapure water, and then continuously supplied onto the surface of the solution covering the cells attached to the glass-base dish, at a flow-rate of 200 ml/min.

(b) Time courses of the decrease of dissolved O_2 concentration in the cell culture medium when the injected gas mixture was changed from normal air to an air-nitrogen mixture at time 0. To reach 0% O_2; *i.e.*, below the sensor's detection limit of 0.05% O_2, an enzymatic method was employed using the GLOX buffer. For the details of the method, see **Online Methods**.
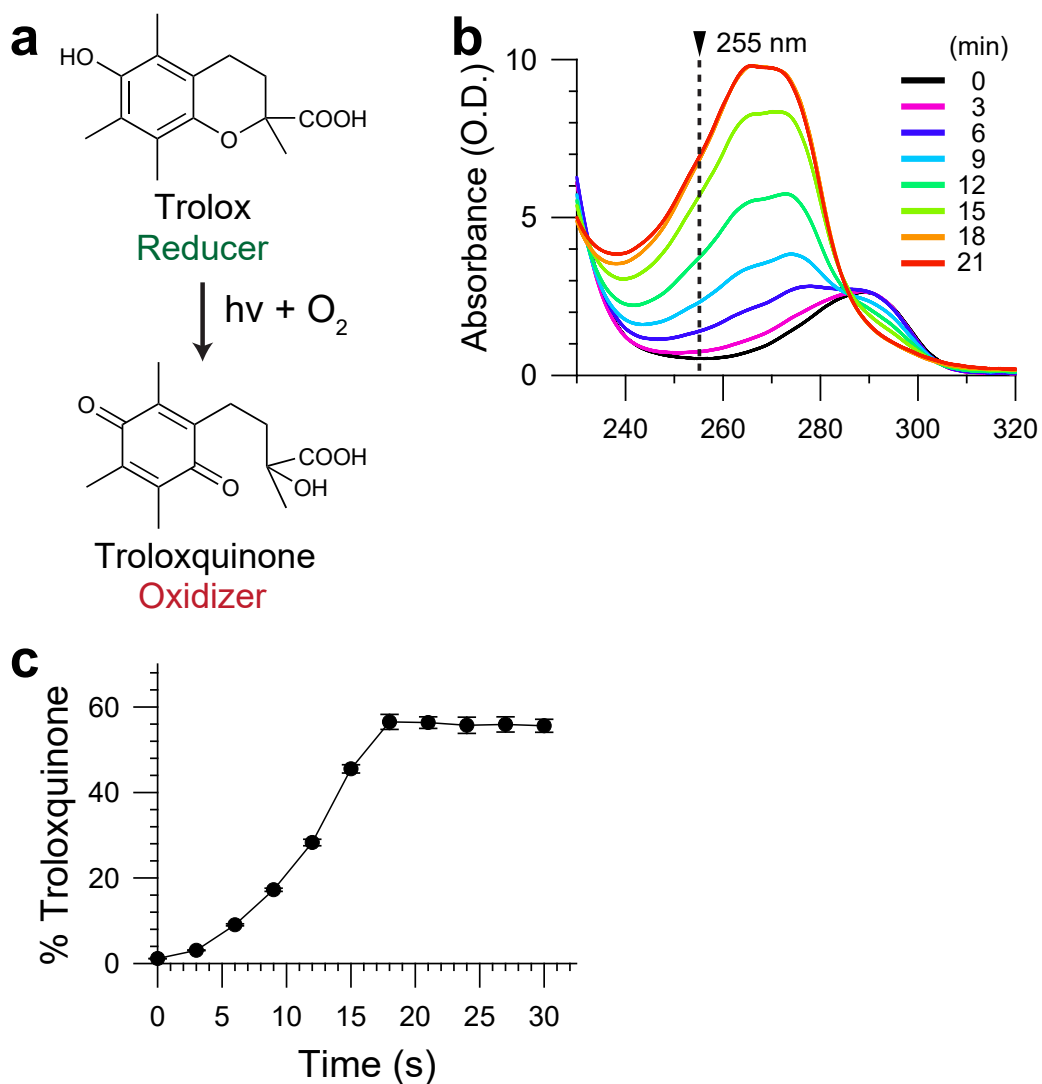
Supplementary Figure 4 | Troloxquinone preparation from trolox by UV irradiation.

(a) Troloxquinone was generated from trolox by UV (λ_{max}~302 nm)-induced oxidation.

(b) Time-dependent changes of the absorption spectrum of the trolox solution (λ_{max}~290 nm) induced by UV irradiation, showing the formation of troloxquinone (λ_{max}~270 nm), with an isosbestic point of ~285 nm. The optical density (O.D.) refers to that of the UV-irradiated solution before dilution for the absorption measurement (among 10 independent experiments.). Absorption at 255 nm was used for determining the concentrations of trolox and troloxquinone[11]. No difference was found between the spectra obtained at 18 and 21 min. The total amount of TX and TQ was 1 mM. Representative spectra among 10 totally independent experiments.

(c) The time-dependent increase of the troloxquinone fraction (*vs.* trolox + troloxquinone, mean ± SEM values, n = 10 independent experiments) after UV irradiation, reaching

quasi-photoequilibrium at ~60% troloxquinone (*vs.* 40% trolox) after 20 min UV irradiation under the conditions employed here. For details, see **Online Methods**.
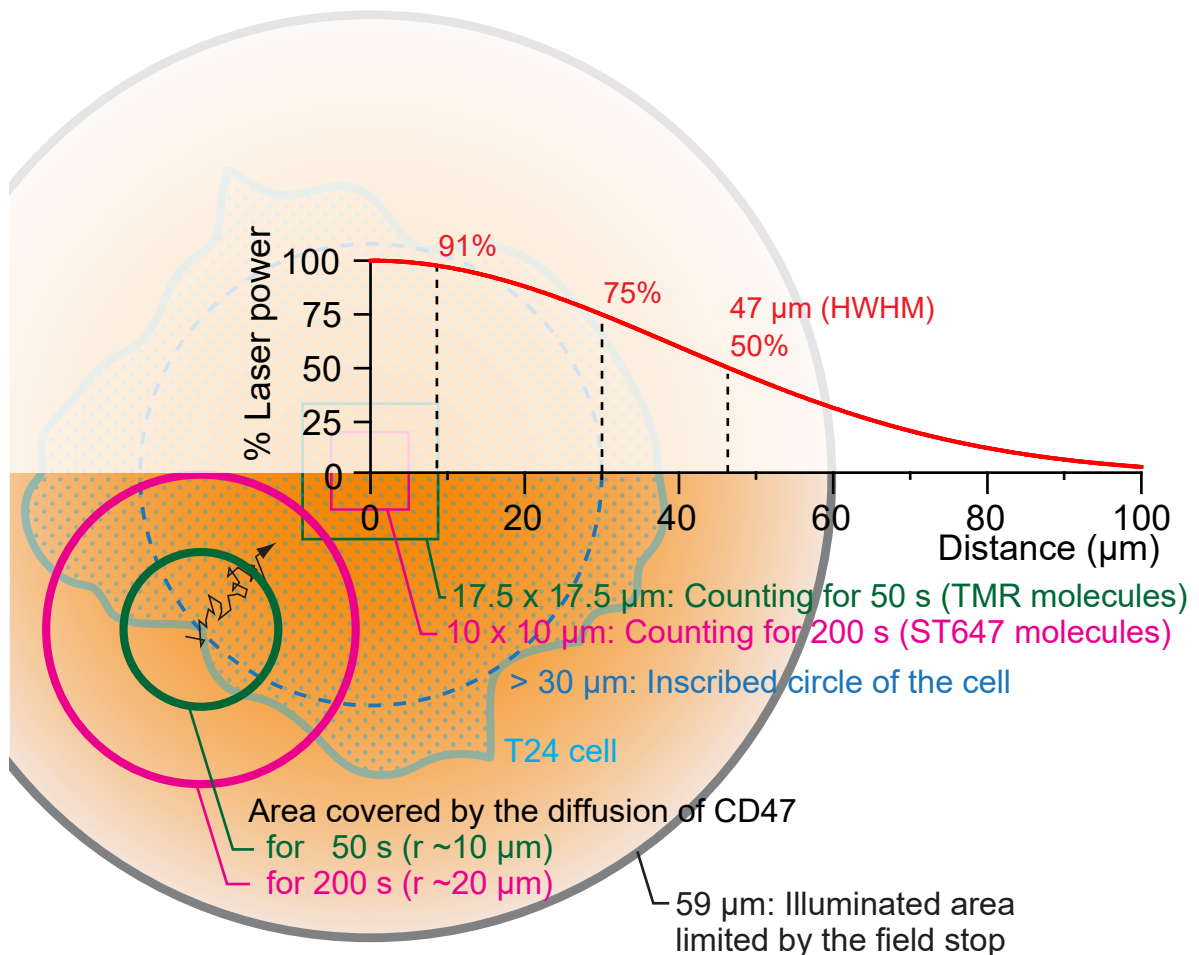
Supplementary Figure 5 | Schematic figure showing the selection of the PM area for counting the number of fluorescent spots to evaluate the photobleaching rate, without the influence of fluorescent molecules diffusing into the counting area from the PM domains where the exciting laser intensity was lower or nearly none (mostly from the apical PM).

Schematic drawing of the TIRF illuminated spot on the focal plane at the basal PM of T24 cells used in this study (HWHM~ 47 µm; the field stop limited the illumination area to a circular area with a 59 µm radius). The typical basal PM area of T24 cells (40~60% confluency; see blue hand-drawn curves) was a circle with a ~30 µm radius (inscribed dashed circle). The laser power was reduced gradually over the cell, and near the cell peripheries, which were ~30 µm away from the cell center (the center of the laser spot was placed near the cell center), the laser intensity was decreased to 75% of that at the center of the illuminated area.

To evaluate the photobleaching rates by counting the number of fluorescent spots in each image in an image sequence, the measurements must be made in an area where the

influx of fluorescently-labeled CD47 molecules into the illumination area from the outside by diffusion is negligible and the laser illumination was rather uniform.

As shown in the figure, in the case of T24 cells, since almost the entire basal PM was illuminated at the intensity close to the center of the spot (>75%), the major problem for evaluating photobleaching by counting the spot numbers was caused by the influx of fluorescently-labeled CD47 molecules, diffusing into the counting area from the apical PM. Since the effective macroscopic diffusion coefficient of CD47 was 0.25 ± 0.14 μm^2/s (mean $\pm$ SD), CD47 can diffuse within areas with radii of ~10 and 20 μm during 50 and 200 s, respectively (using mean diffusion coefficient + SD x2, ~95.5% of CD47 molecules). Therefore, the area used for counting fluorescent CD47 spots was limited to a small square region of 17.5 x 17.5 μm (half the diagonal length = 12.4 μm, which is smaller than 20 μm [the cell radius of 30 μm minus 10 μm of the CD47 diffusion radius during 50 s]) for 50-s observations or 10.0 x 10.0 μm (half the diagonal length = 7.1 μm, which is smaller than 10 μm [the cell radius of 30 μm minus 20 μm of the CD47 diffusion radius during 200 s]) for 200-s observations in the center of the laser-illuminated area.

With regard to the uniformity of laser illumination, in these square areas for counting the number of fluorescent spots, the laser intensity was likely reduced from the laser center by only 4.8% or less. Therefore, the illumination is considered to be rather uniform in the area used for counting the number of fluorescent spots.
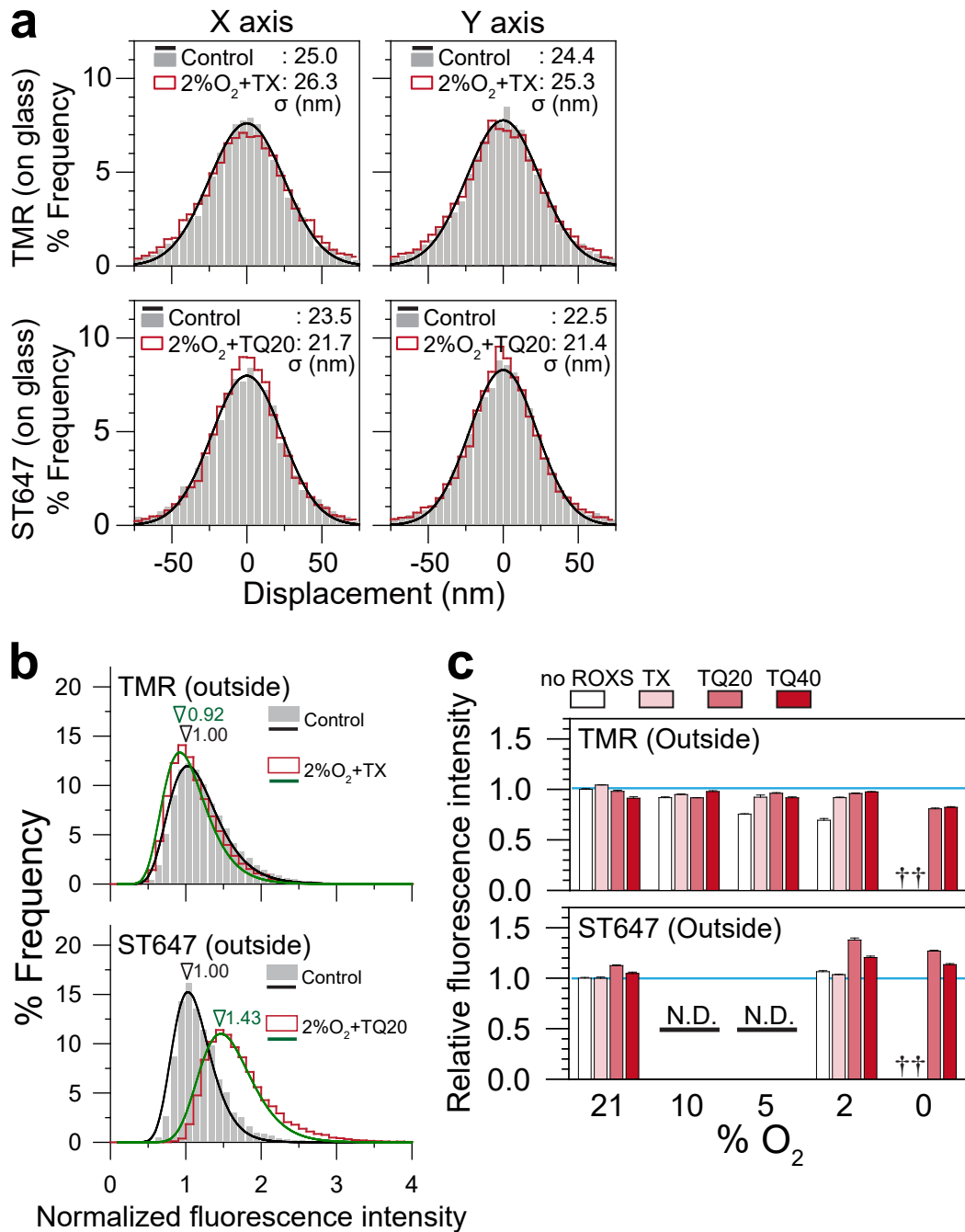
Supplementary Figure 6 | Single-molecule localization precisions and fluorescence signal intensities of single TMR and ST647 molecules (located on the outer cell surface) were either unchanged or only slightly affected when the observation conditions were changed from the control conditions to the optimized low oxygen + ROXS conditions.

(a) The locations (x and y coordinates) of single TMR (**top**) and ST647 (**bottom**) molecules attached to the glass-base dish in T-HBSS, determined for 128 and 151 molecules (TMR and ST647, respectively; after 30 coordinate determinations for each molecule, their mean value

was subtracted from each of the 30 determined coordinates). The standard deviations determined by best-fit Gaussian functions (black curves for the control specimens; the curves for the 2%O_2+ROXS specimens were close to the black curves and are not shown here) provided the single-molecule localization precision.

(b) The distributions of the fluorescence signal intensities (after background subtraction for individual spots) of TMR bound to Halo-CD47 (**top**) and ST647 bound to ACP-CD47 (**bottom**), located on the outer surface of living cells. Distributions could be fitted by log-normal functions[63,64], providing the mode values (triangles; the mode is the signal intensity value at which the log-normal probability distribution function has its maximal value). The intensities were normalized by the mode value determined under control conditions.

(c) The mode values and standard errors of fluorescence intensities obtained by the log-normal fitting of TMR (**top**) and ST647 (**bottom**) located outside the cell, under various %O_2 + ROXS conditions. [†]Unable to determine due to extensive blinking, providing trajectories mostly as short as 1-2 frames (33 and 66 ms), which could not be distinguished from the noise signal. N.D., not done. For n, see **Supplementary Table 1**.
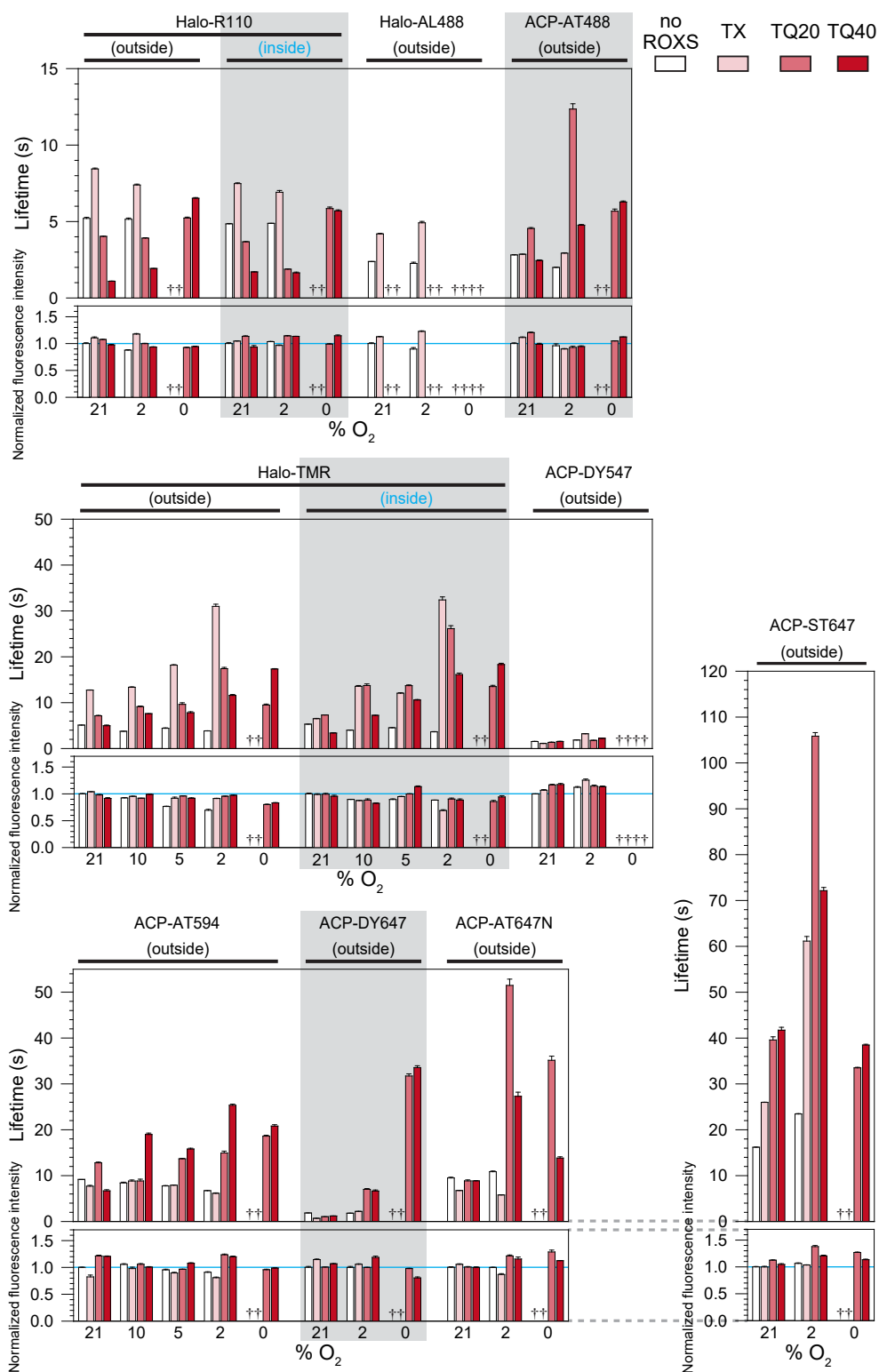
Supplementary Figure 7 | Summary of photobleaching lifetimes (obtained by counting the number of fluorescent spots in each video frame in live cells; exponential decay time constant [= mean] ± the standard error) and fluorescence intensities of organic fluorophores (the mode values ± the standard errors obtained by log-normal fitting)

examined in this study, under various dissolved oxygen concentrations and ROXS conditions. Also see **Supplementary Table 1**. For *n*, see **Supplementary Table 1**.

(Top row) Blue-excitable dyes: Rhodamine 110 (R110), Alexa488 (AL488), and ATTO488 (AT488).

(Middle row) Green-excitable dyes: TMR and DY547.

(Bottom row) Orange-red-excitable dyes: AT594, DY647, ATTO647, and ST647.

The top box in each row shows photobleaching lifetimes, whereas the bottom box in each row shows fluorescence intensities. For the dependence on tag proteins (Halo and ACP), see **Supplementary Fig. 9**. [†]Unable to determine due to extensive blinking, providing trajectories mostly as short as 1-2 frames (33 and 66 ms), which could not be distinguished from the noise signal.

To examine fluorophores located outside the cell, R110-, AL488-, TMR-, TMR-TX-, Cy3-TX-, and Cy5-TX-Halo ligands were conjugated to Halo-CD47, and AT488-, DY547-, AT594-, AT594-TX-, DY647-, AT647N-, and ST647-CoA were linked to ACP-CD47. To examine fluorophores located in the cytoplasm, R110 and TMR were attached to CD47-Halo.

a TMR (inside)

Time (s)

Control

2%O$_2$+TX

10 μm

b

% Spots

TMR (inside)

2%O$_2$+TX: 32.4 s
2%O$_2$: 3.6 s
Control: 5.3 s

Time (s)

c

% Frequency

TMR (inside)

▽0.95
▽1.00

Control
2%O$_2$+TX

Normalized fluorescence intensity

d

no ROXS TX TQ20 TQ40

Lifetime (s)

TMR (inside)

x7

x1

††

Fold increase

Normalized fluorescence intensity

21 10 5 2 0

††

% O$_2$
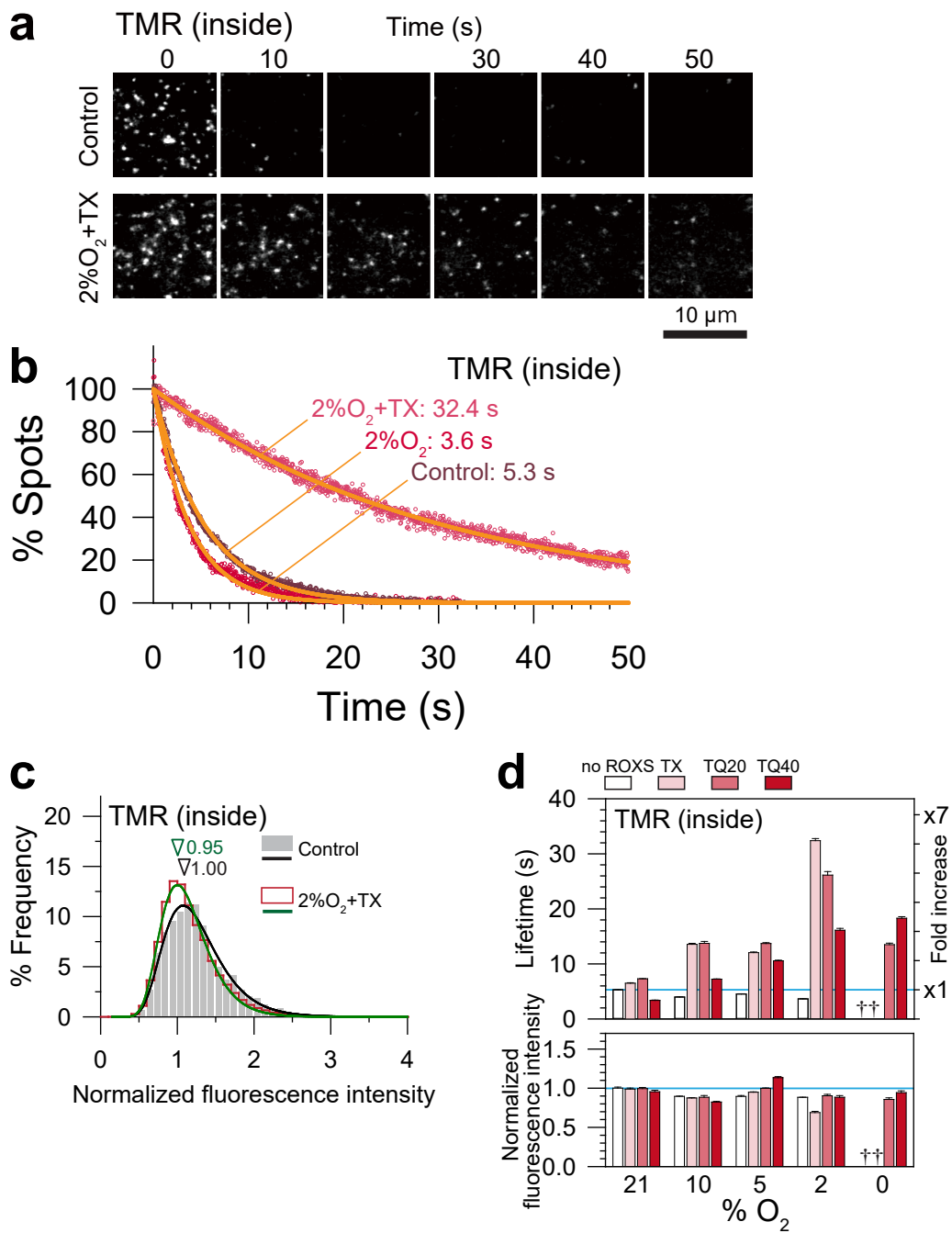
Supplementary Figure 8 | TMR (Halo ligand conjugated with TMR) is a membrane permeable dye useful to label the Halo-tag protein inside the cell (CD47-Halo). Its photobleaching *inside* the living cells (in the cytoplasm) can be suppressed by low O$_2$ concentrations + ROXS, as effectively as that of TMR located outside the cell.

(a) Representative (among six independent experiments) time series of TIRF images of TMR bound to CD47-Halo (TMR located inside the cell) in a single cell.

(b) The time-dependent decreases of the numbers of fluorescent-spots of TMR inside the cell counted in each frame, observed in a single cell. Orange curves represent the best-fit single exponential functions.

(c) The distributions of the fluorescence signal intensities (after background subtraction for individual spots) of TMR bound to CD47-Halo located in the cytoplasm of a single living cell. Distributions could be fitted by log-normal functions, providing the mode values (triangles). The intensities were normalized by the mode value determined under control conditions.

(d) The photobleaching lifetimes (single-molecule tracking lifetime; exponential decay time constant [= mean] ± the standard error) (**top**) and the fluorescence intensities (the mode values ± the standard errors obtained by log-normal fitting) (**bottom**) of TMR bound to CD47-Halo, under various %O_2 + ROXS conditions. Photobleaching lifetimes inside the living cells were prolonged to about the same extent as those located outside the cells. [†]Unable to determine due to extensive blinking, providing trajectories mostly as short as 1-2 frames (33 and 66 ms), which could not be distinguished from the noise signal. For n, see **Supplementary Table 1**.
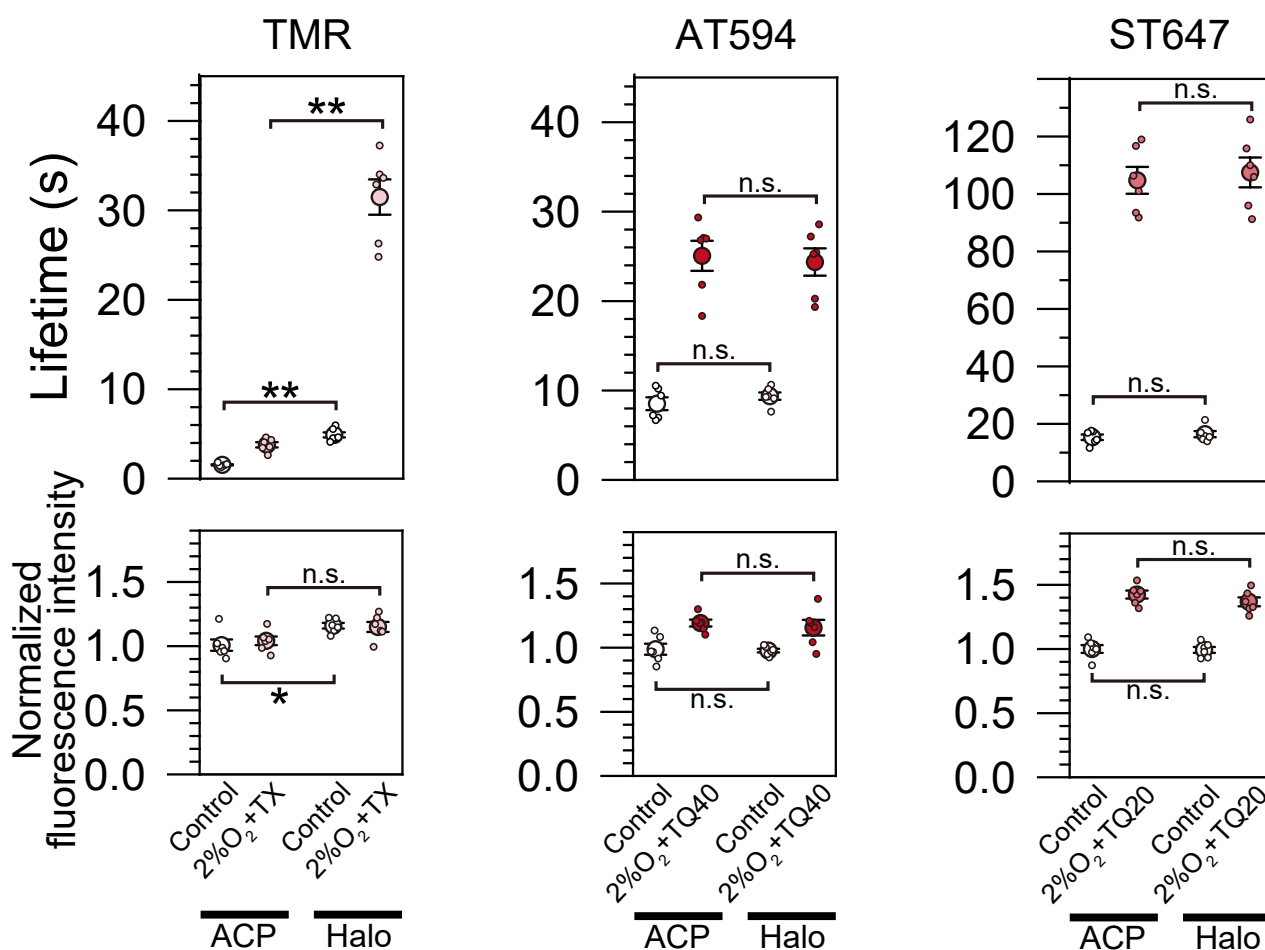
Supplementary Figure 9 | Comparison between Halo and ACP tags, in terms of the photostabilization effect by 2%O_2+ROXS on TMR, AT594, and ST647 bound to these protein tags (linked to the N-terminus of CD47, located outside the cell).

Six independent experiments were performed for each dye under a given ROXS condition. For each experiment, the photobleaching lifetime (exponential decay time constant, **top**) and the mode of the signal intensity of single spots (obtained by the log-normal fitting; see **Supplementary Fig. 6b**, **bottom**) were obtained. These values were averaged to obtain the mean ± SEM of the six independent experiments. ROXS conditions were those optimized for the Halo (for TMR) or ACP (for AT594 and ST647)-tag protein and its fluorescent ligands (**Fig. 1d**).

The photobleaching lifetime of TMR bound to the Halo-tag protein was significantly longer than that bound to the ACP-tag protein under both the control and 2%O_2+ROXS conditions. Meanwhile, no statistically significant differences were detectable between Halo- and ACP-tag proteins for the dyes of AT594 and ST647. Two-sided Welch's T test: [*P* for ACP

vs. Halo (control), P for ACP vs. Halo (optimized conditions)] = [4.5 x 10^{-5}, 2.6 x 10^{-5}] for TMR, [0.33, 0.76] for AT594, and [0.49, 0.70] for ST647).

For the fluorescent intensities, significant difference was found only between ACP-TMR and Halo-TMR under the control conditions (two-sided Welch's T test: [P for ACP vs Halo (control), P for ACP vs Halo (optimized conditions)] = [0.017, 0.065] for TMR, [0.81, 0.61] for AT594, and [0.84, 0.25] for ST647). For number of fluorescent spots, n, see **Supplementary Table 1**. **: $P < 0.01$, *: $P < 0.05$, n.s.: $P > 0.05$
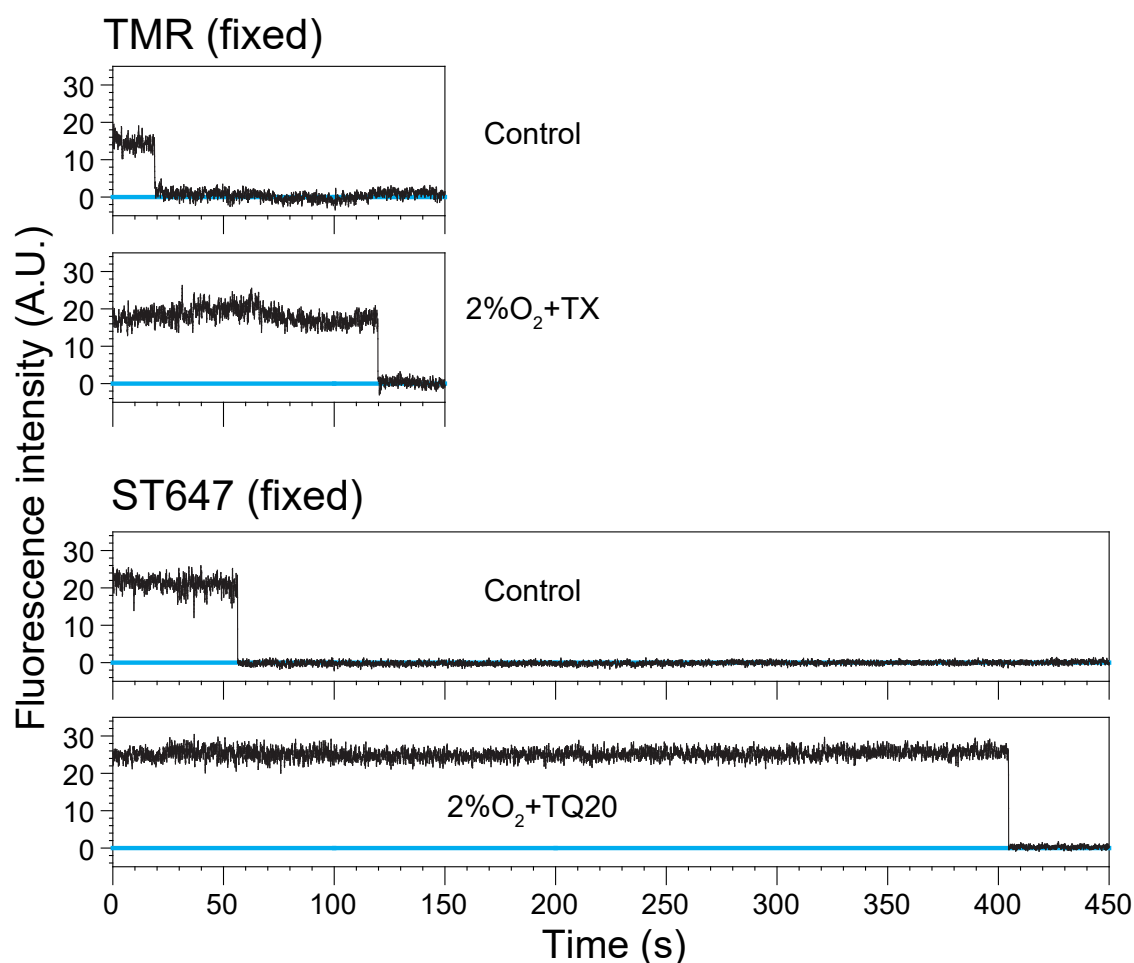
Supplementary Figure 10 | TMR (bound to Halo-CD47) and ST647 (bound to ACP-CD47) hardly exhibited blinking at a time resolution of 33 ms under either the control or $2\%O_2+$ optimized ROXS conditions. To avoid other difficulties of tracking moving molecules, the cells were chemically fixed[65].

Typical (for *n*, see **Table 1**) time traces of fluorescence intensities of single molecules of TMR (**two top boxes**) and ST647 (**two bottom boxes**). Trajectories with durations of ~4x lifetimes (**Table 1**) were selected arbitrarily. Note that blinking (temporary transition to the dark state) is undetectable even in these long traces.
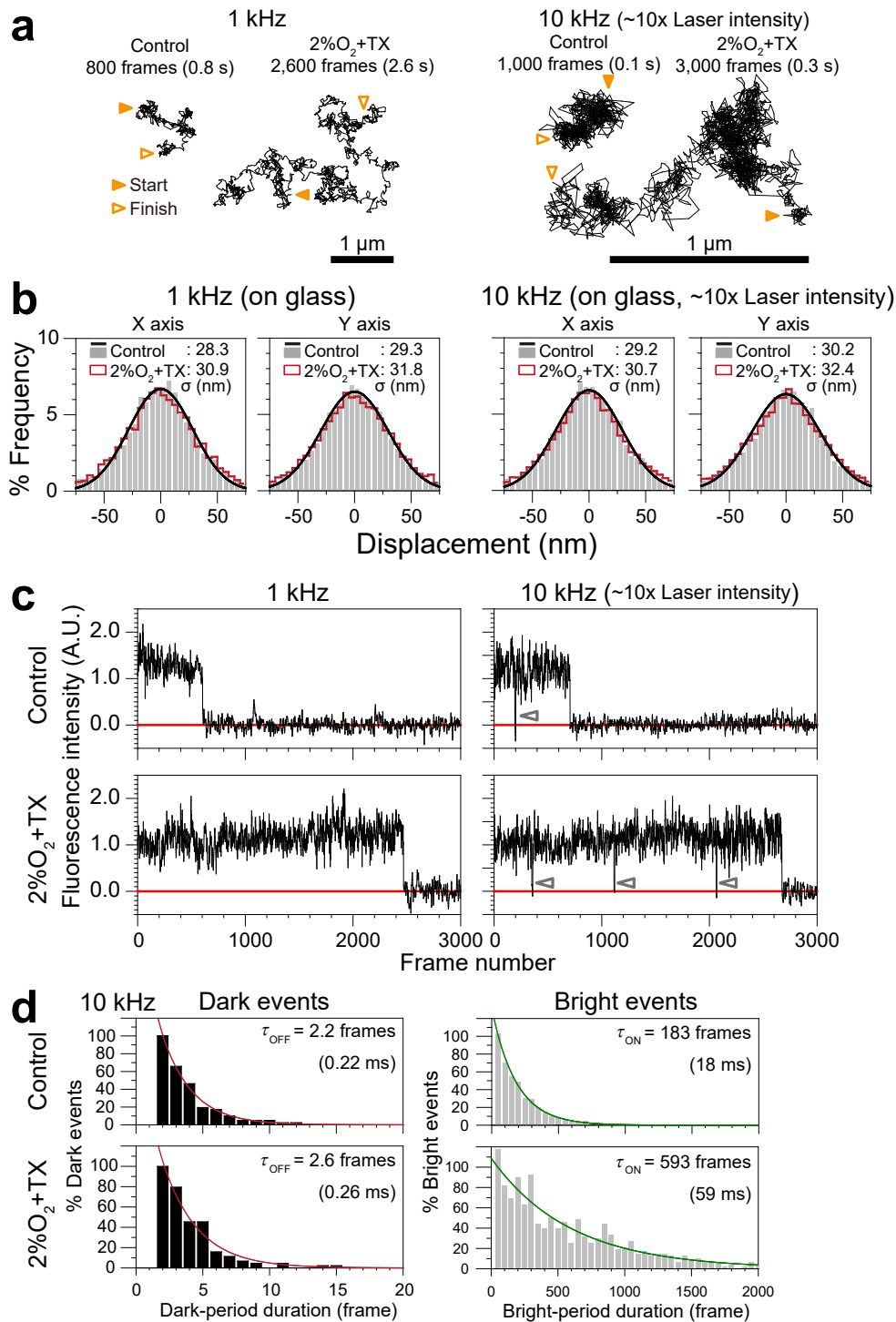
Supplementary Figure 11 | Ultrafast single fluorescent-molecule tracking at a 0.1-ms resolution revealed TMR blinking, with alternating dark-and-bright states with lifetimes of 0.22 and 18 ms (0.26 and 59 ms), respectively, under the control (optimized; 2%O$_2$+TX) conditions. TMR bound to Halo-CD47 in the live-cell PM (outside the cell) (**a, c, d**) or TMR attached to the coverslip surface (**b**) was observed.

(a) Typical trajectories (among 331, 585, 401 and 583 trajectories from left to right) of TMR bound to Halo-CD47 in the live-cell PM (outside the cell) at observation frame rates of 1 **(left)** and 10 kHz **(right)** (integration times of 1 and 0.1 ms, respectively) under the control and optimized (2%O_2+TX) conditions. A few % of TMR molecules could be tracked without photoblinking and photobleaching for periods of ~1,000 and ~3,000 frames under the control and optimized conditions, respectively, under single-molecule tracking conditions at both 1 and 10 kHz (in terms of the number of frames, the observable length remained the same for both 1 and 10 kHz when the laser intensity was increased by a factor of ~10 at 10 kHz). This way, the number of emitted photons from a single molecule per frame would remain about the same. No non-linear effects were observed at the laser powers employed here. The integrated laser intensity during a single frame was adjusted to become about the same for the observations at both frame rates. Note that the trajectory lengths in terms of the actual time are different by a factor of ~10 for the two frame rates, and therefore, the trajectories are shown in different scales. Here, the integrated laser intensities during a single frame are ~60% of those employed at video rate. The actual laser intensities employed are described in the Online Methods section "Single fluorescent-molecule imaging".

(b) Single-molecule localization precisions (on the x and y axes, representing the horizontal and vertical axes of the camera) for TMR attached to the glass observed at frame rates of 1 and 10 kHz, determined for 140 and 131 molecules (1 and 10 kHz, respectively; after 30 coordinate determinations for each molecule, their mean value was subtracted from each of the 30 determined coordinates. Grey closed bars (green best-fit Gaussian curves) and red open bars are for the control and optimized conditions. The curves for the 2%O_2+ROXS specimens were close to the black curves and are not shown here. The precision is given as the standard deviation of the best-fit Gaussian functions. By varying the excitation laser intensity by a factor of ~10, the single-molecule localization precisions at 1 and 10 kHz were largely equalized.

(c) Typical (among the same number of trajectories shown in **a**) time traces of fluorescence intensities of single molecules of TMR bound to Halo-CD47 in the live-cell PM under the control and optimized conditions (**top and bottom boxes, respectively**), observed at frame rates of 1 and 10 kHz (**left and right boxes, respectively**). At an observation frame rate of 10 kHz, blinking (temporary transition to the state of no signal intensity) of

TMR was detected (triangles). The x-axis is given as the frame number. The actual time is 1 ms/frame for 1 kHz and 0.1 ms/frame for 10 kHz.

(d) Distributions of the dark (**left**) and bright (**right**) periods detected at 10 kHz. Red and green curves are best-fit single exponential functions, providing the lifetimes of the dark and bright states of 0.22 ± 0.0050 and 18 ± 0.33 ms, respectively, under the control conditions, and 0.26 ± 0.011 and 59 ± 3.5 ms, respectively, under the optimized (2%O_2+TX) conditions (exponential decay time constant [= mean] ± its standard error; n for dark and bright events = 115 and 585 for control, and 140 and 583 for 2%O_2+TX conditions). These results suggest that blinking was rarely detectable at lower frame rates, such as 1 kHz and 30 Hz, due to averaging over 1 and 33 ms (much longer than the dark periods).
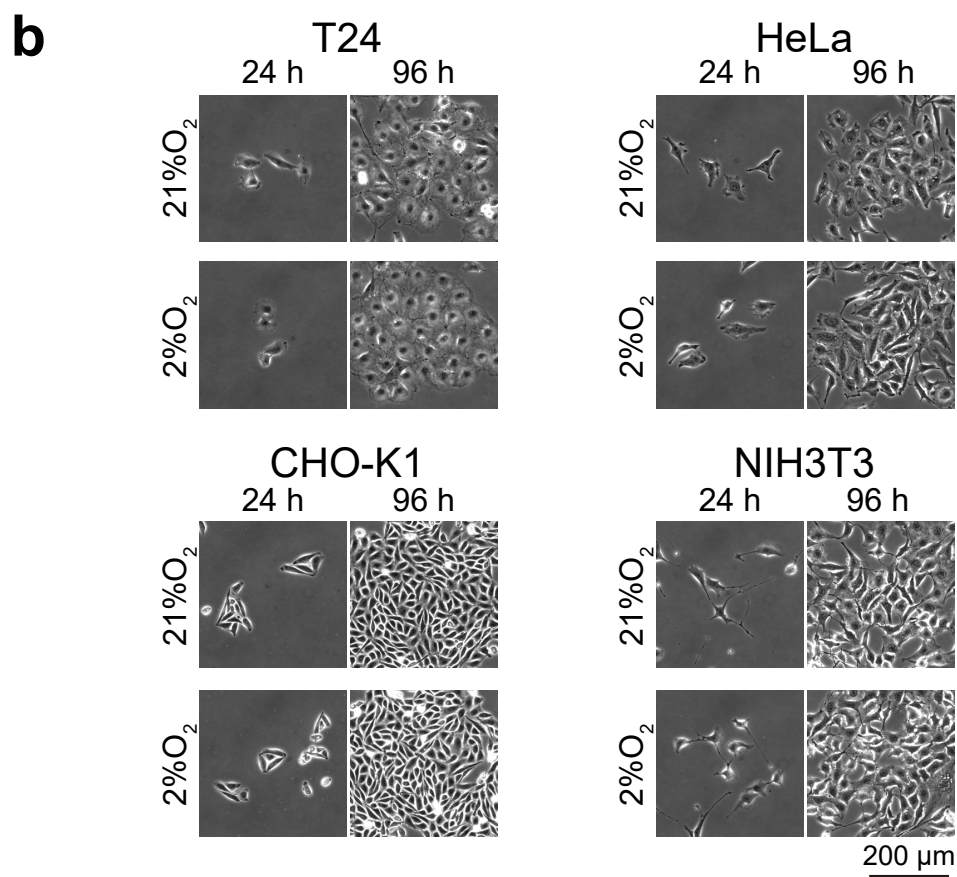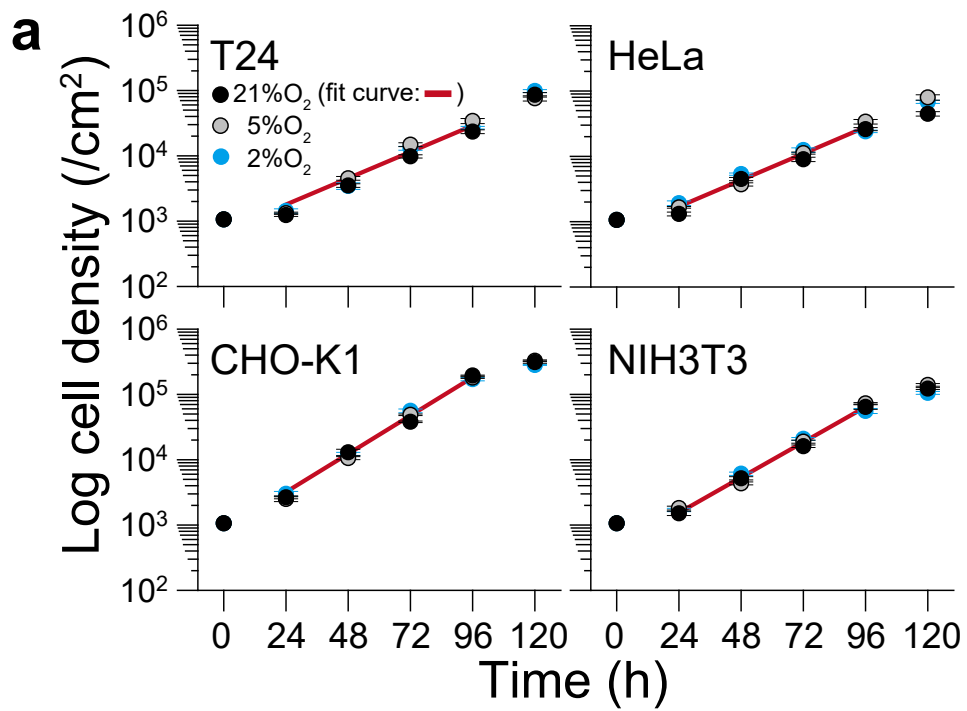
Supplementary Figure 12 | Cells grew at about the same rate under 2, 5, and 21% oxygen atmospheres.

(a) The number densities of T24, HeLa, CHO-K1, and NIH3T3 cells cultured with complete growth medium under 5% CO_2 in the presence of 2, 5, and 21% oxygen atmospheres, plotted as a function of time after inoculation (mean ± SEM, n = 6). The doubling time was obtained by fitting the cell density between 24 and 96 h with a single exponential growth curve, and shown in **Fig. 3a** (note that the y-axis is in the log scale). The data at ~126 h were not used for the evaluation of the doubling time, because the cell confluencies were high at this time point, which might have already induced contact inhibition of growth. Note that the results obtained under the conditions of 2, 5, and 21%O_2 were similar to each other for each cell line.

(b) Typical (among 6 fields for each picture) phase-contrast images of cells cultured under 21 or 2%O_2 conditions for 24 or 96 h after plating.
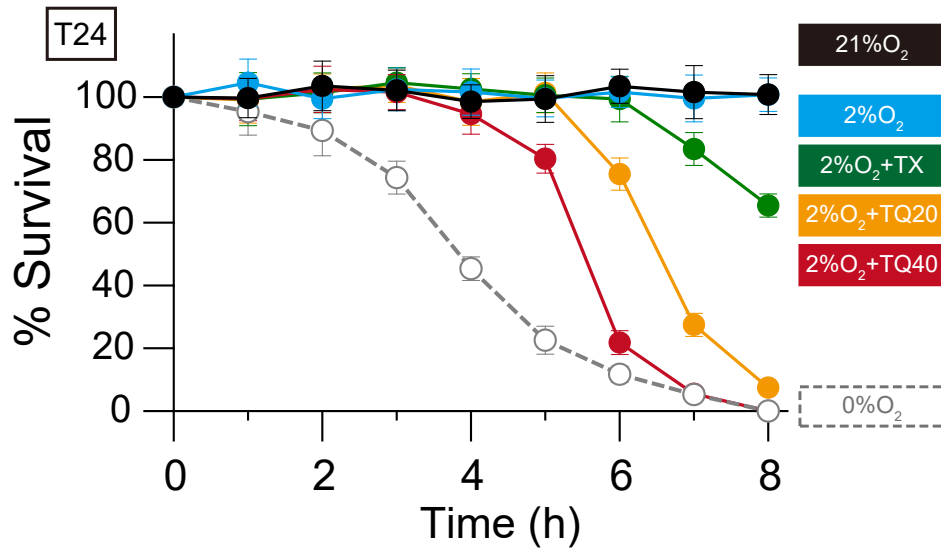
Supplementary Figure 13 | Percentages of surviving T24 cells, under various low-oxygen + ROXS conditions, determined by the trypan-blue exclusion assay (mean ± SEM, n = 6 independent experiments).
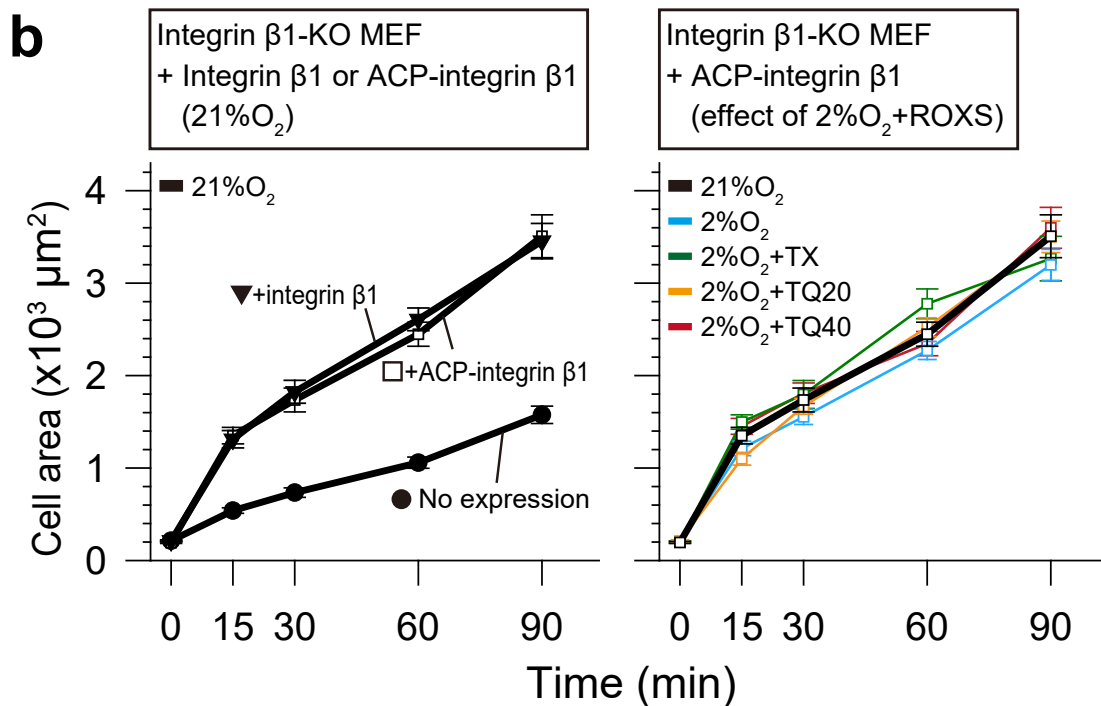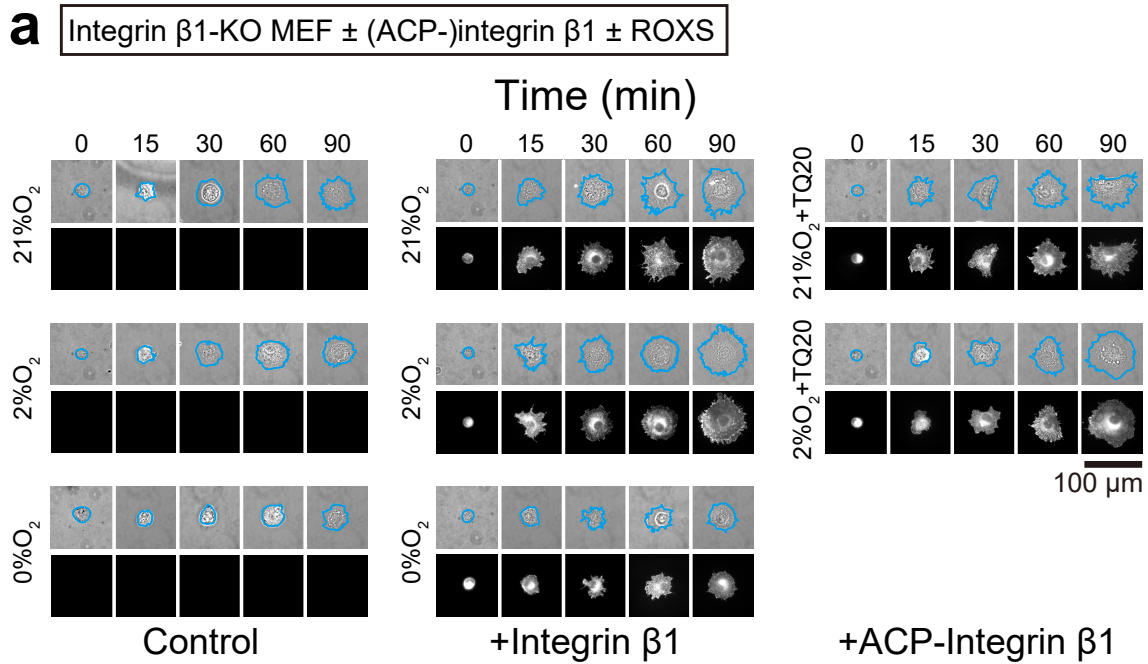
Supplementary Figure 14 | Spreading of integrin β1-KO MEF cells before and after transfection of the integrin β1 or ACP-integrin β1 cDNA was inspected under 0, 2, and 21%O_2 conditions as well as those with 2%O_2+ROXS (TX, TQ20, and TQ40). Differences in cell spreading were undetectable between the 21%O_2 and 2%O_2+ROXS (TX, TQ20, and TQ40) conditions for at least 90 min.

(a) Representative (among 20 cells inspected closely) phase-contrast (**top**) and anti-integrin β1 immunofluorescence (epi-fluorescence, **bottom**) images of integrin β1-KO MEFs with or without transfection-expression of integrin β1 (no tag) or ACP-integrin β1, at 0, 15, 30, 60, and 90 min after plating on FN-coated glass-base dishes. The anti-integrin β1 monoclonal antibody used here (K20) can bind to both active and inactive integrin β1. The cells with similar integrin β1 expression levels were selected for comparing cells cultured under different oxygen concentrations. Cyan lines in the phase-contrast images indicate cell peripheries, and by measuring the area within the cyan line, the cell area attached to the glass was evaluated (see **b**). Non-transfected integrin β1-KO MEF cells spread more slowly than transfected cells. Cells under 2% oxygen appeared to spread as well as those under 21% oxygen, whereas cells under 0% oxygen spread much more slowly.

(b) The time course of cell spreading after plating, as measured by the cell area attached to the glass observed by phase-contrast microscopy (mean cell area ± SEM, n = 20).

(**left**) Expression of integrin β1 or ACP-integrin β1 at similar levels enhanced cell spreading after plating to similar extents. This result suggests that ACP attached to the N-terminus of integrin β1 does not strongly inhibit integrin β1 function. As plotted in **Fig. 3d** (based on the data shown in **a**), under 0%O_2, cell spreading was greatly suppressed in cells with and without integrin β1 expression. No significant difference was found between integrin β1 and ACP-integrin β1 up to 90 min (two-sided Mann-Whitney U test; for the actual P values, see **Supplementary Table 5**).

(**right**) The time course of spreading of integrin β1-KO MEFs expressing ACP-integrin β1 was not affected for at least 90 min under the conditions of 2%O_2+ROXS (TX, TQ20, and TQ40). The statistical significance was evaluated by the two-sided Mann-Whitney U test (for the actual P values, see **Supplementary Table 5**).
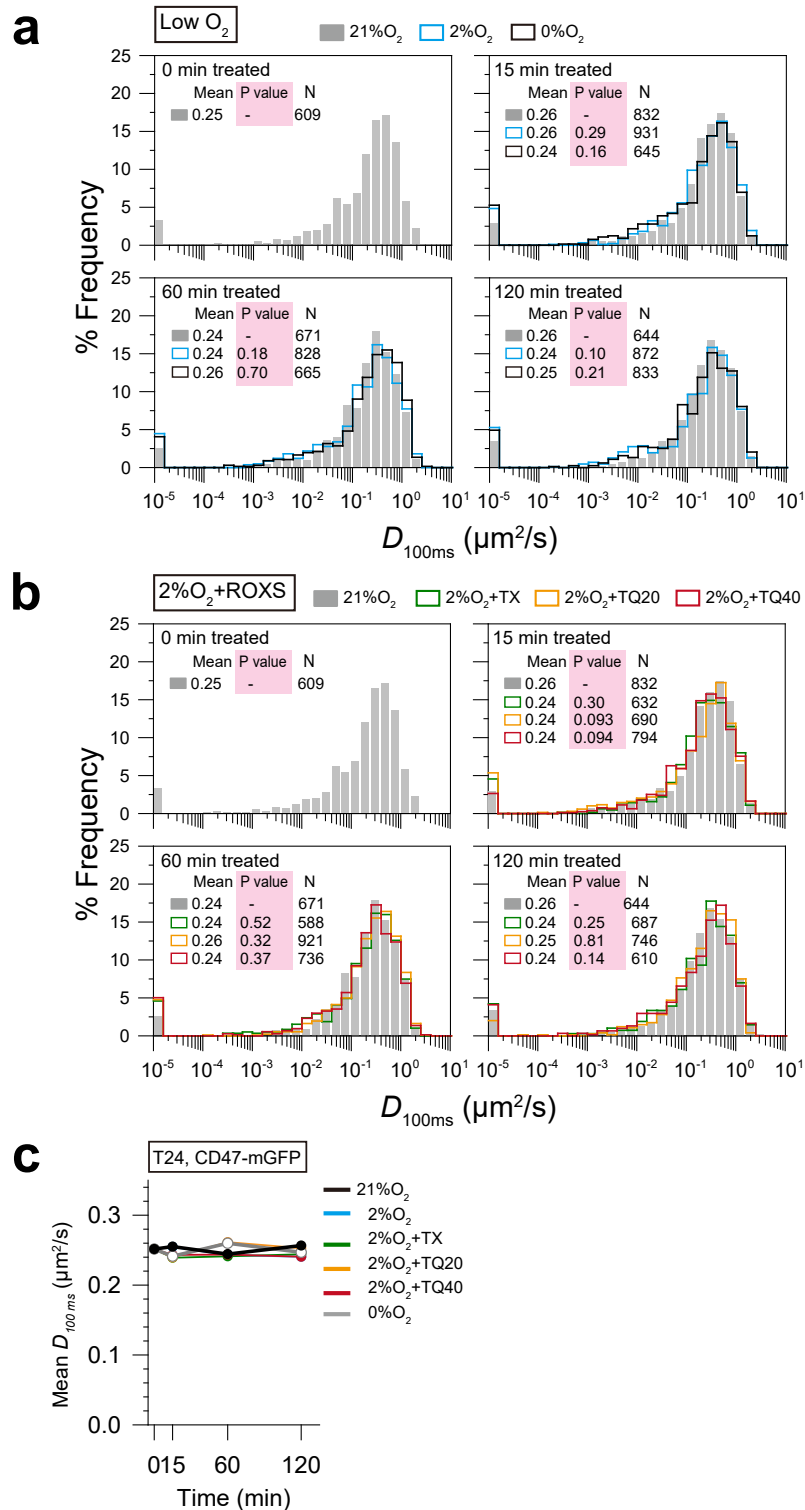
Supplementary Figure 15 | The diffusion of CD47-mGFP in the PM of T24 cells did not significantly change under various O₂ and ROXS conditions. The mGFP probe was employed here, because the photo-properties of GFP were hardly affected by the O₂ concentration and the ROXS conditions.

(**a**) The distributions of the diffusion coefficients (in the time scale of 100 ms, D_{100ms}) of CD47-mGFP when T24 cells were incubated in 21, 2, and 0% oxygen for various time periods up to 120 min. The mean value, the P value (compared with the distribution under control conditions [21%O_2], using the two-sided Mann–Whitney U-test), and the N value (total number of trajectories inspected here) are shown in each box.

(**b**) The distributions of the diffusion coefficients of CD47-mGFP when T24 cells were incubated under various ROXS conditions (TX, TQ20, and TQ40; all in the presence of 2% O_2) for various time periods up to 120 min. The results were compared with the D_{100ms} distributions under 21%O_2 conditions after the given treatment periods. The mean value, the P value (compared with the distribution under control conditions [21%O_2], using the two-sided Mann–Whitney U-test), and the N value (total number of trajectories inspected here) are shown in each box.

(**c**) Mean diffusion coefficients of CD47-mGFP in T24 cells plotted as a function of time under various conditions. As shown in (**a**) and (**b**), under all conditions examined here, the diffusion coefficient of CD47-mGFP was not statistically significantly affected, at least for 120 min, in T24-cell PM. This result suggests that the T24-cell PM (with its associated actin meshwork) is less sensitive to 0%O_2 as compared with the HeLa-cell PM.
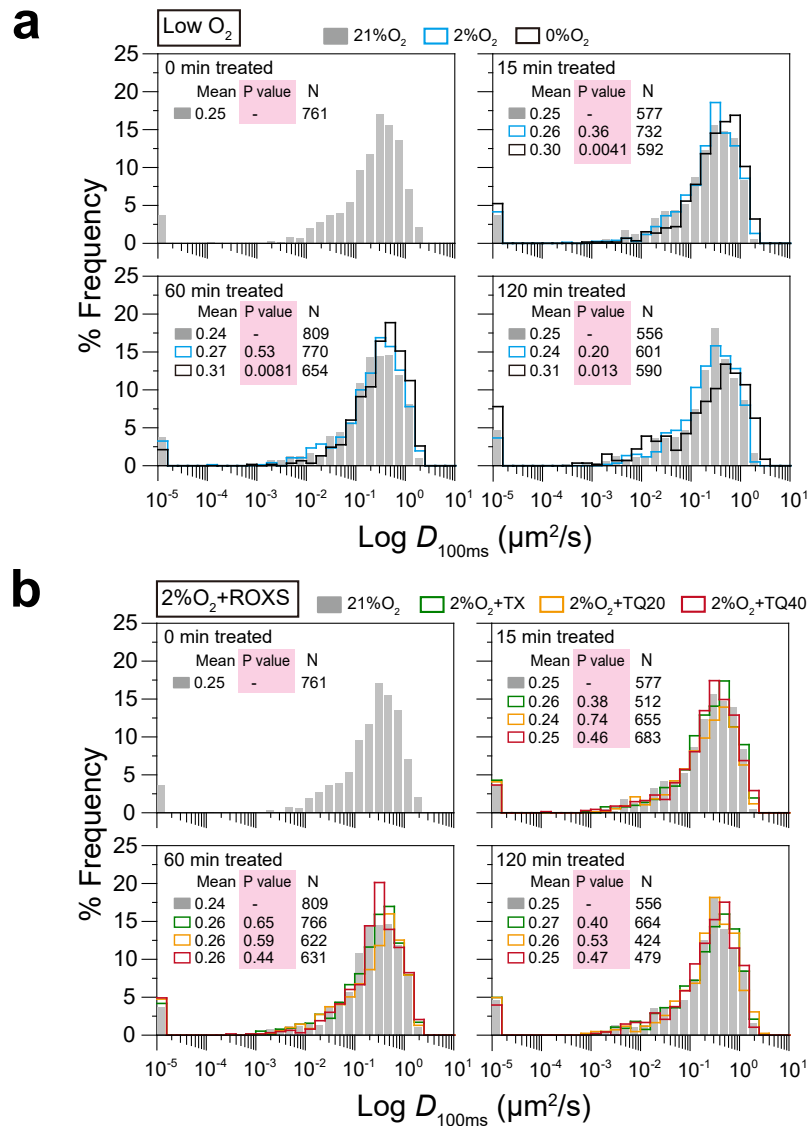
Supplementary Figure 16 | The diffusion of CD47-mGFP in the PM of HeLa cells was *enhanced* even 15 min after the cells were placed under 0% oxygen, at variance with the diffusion of CD47-mGFP in T24 cells. The figure arrangements, keys, and the numbers related to statistics are the same as those of **Supplementary Fig. 15a and b**.

a TMR-TX-Halo ligand
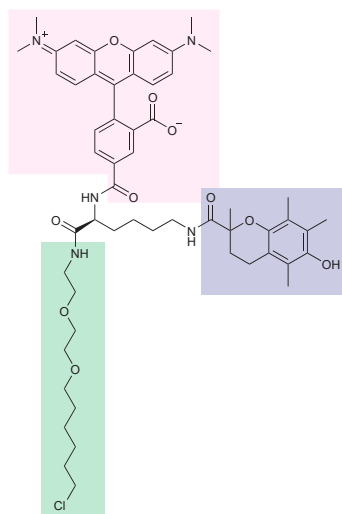
b AT594-TX-CoA
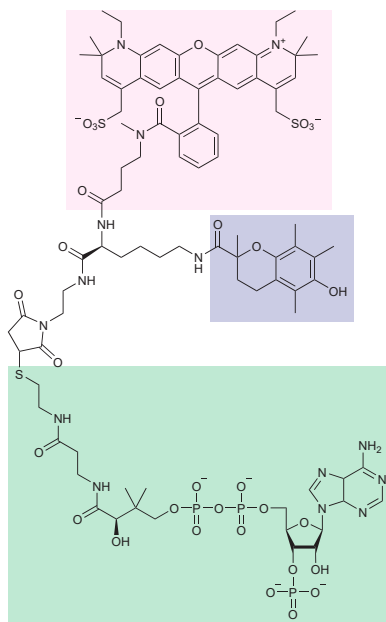
c Cy3-TX-Halo ligand
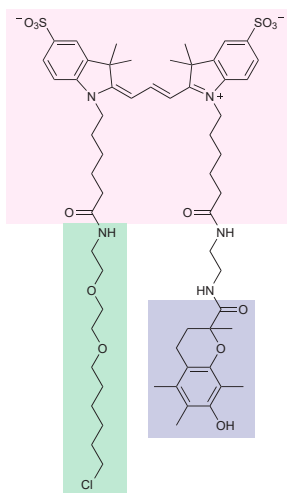
d Cy5-TX-Halo ligand
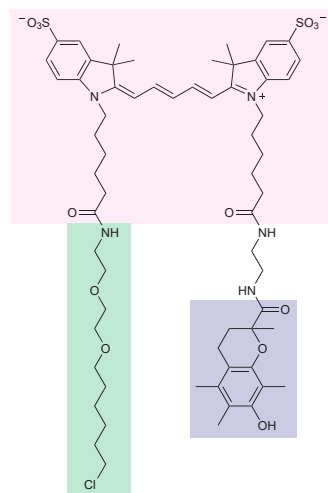
Supplementary Figure 17 | Chemical structures of the trolox-conjugated fluorophores examined in the present study.

Trolox-conjugated fluorophores for avoiding photobleaching were independently developed by two groups[1,2,4,6]. However, TX-conjugated TMR (TMR-TX-Halo ligand, **a**) and AT594 (AT594-TX-CoA, **b**) have never been synthesized or examined. In addition, in the present study, we employed the Halo ligand and CoA (for conjugation to ACP), rather than the SNAP ligand, because the Halo ligand and the CoA compound worked better for single-molecule

tracking of CD47, due to lower non-specific binding to the PM (Cy3-TX-Halo ligand, **c**, and Cy5-TX-Halo ligand, **d**). The fluorescent dye moiety (magenta shading) was conjugated to trolox (purple shading) and either the halo ligand or the ACP ligand (coenzyme A) (green shading).
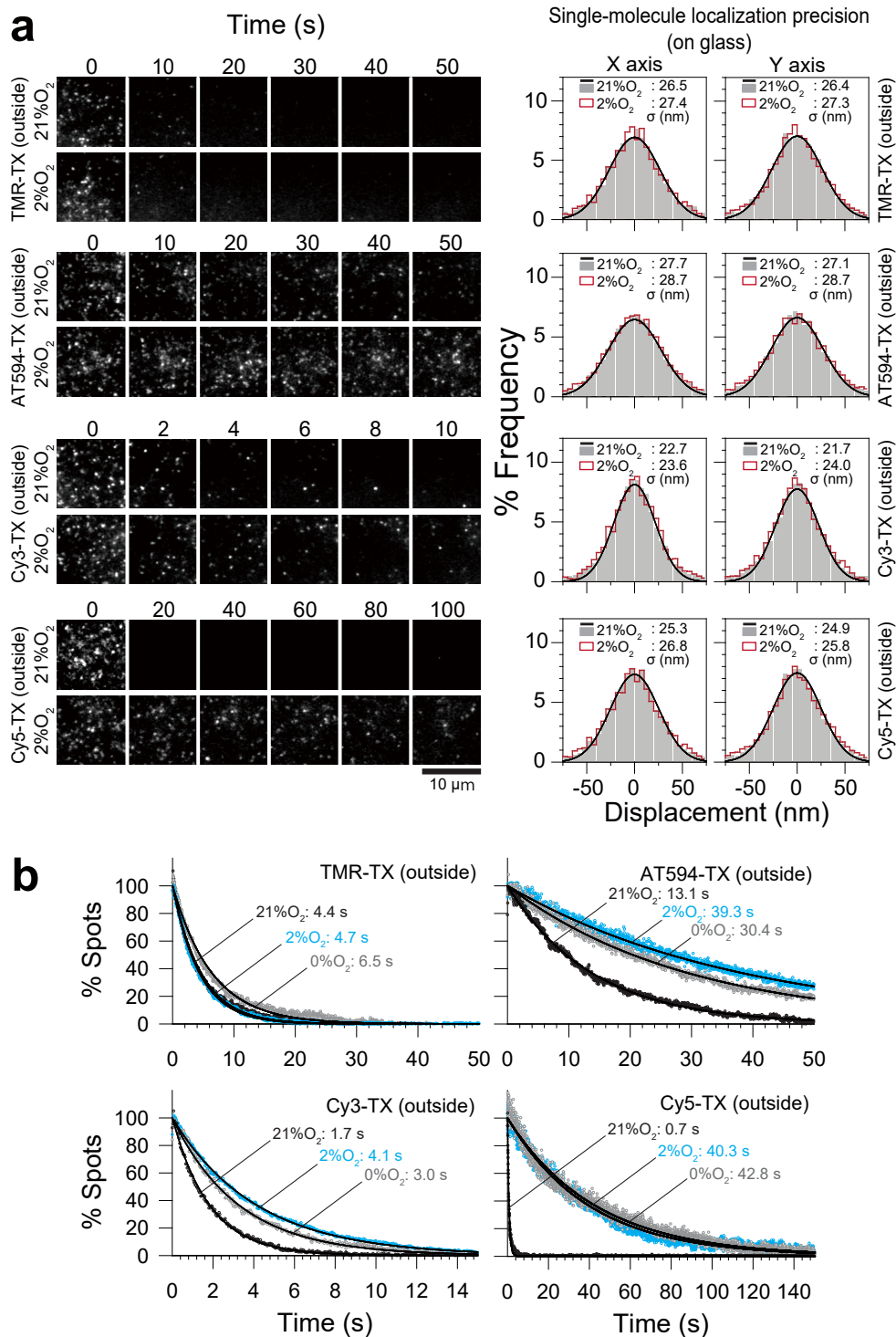
Supplementary Figure 18 | Photobleaching time courses of trolox-conjugated fluorescent dyes (TMR-TX-, Cy3-TX-, and Cy5-TX-Halo-ligands and AT594-TX-CoA) under single fluorescent-molecule imaging conditions at localization precisions in the range of 21.7~28.7 nm, under 21 and 2%O_2 conditions (no ROXS here because TX is already covalently linked to the dye moiety), observed in T24 cells.

(a) Representative (among six independent experiments) time series of TIRF images (**left**) of TMR-TX, AT594-TX, Cy3-TX, and Cy5-TX bound to Halo-CD47 (probes located outside the cell) and single-molecule localization precisions of those dyes attached to the glass, determined for 137, 151, 143 and 135 molecules of TMR-TX, AT594-TX, Cy3-TX, and Cy5-TX, respectively (see **Supplementary Fig. 6a** for details) (**right**). The results were compared between 21 and 2%O_2. Grey closed bars (black best-fit Gaussian curves) are for 21%O_2 and red open bars are for 2%O_2 conditions. The best-fit Gaussian curves for the 2%O_2 conditions are not shown here, as they almost entirely overlapped with the black best-fit Gaussian curves. The precision is given as the standard deviation of the best-fit Gaussian functions.

(b) The time-dependent decreases of the numbers of fluorescent spots found in each frame. Black curves represent the best-fit single exponential functions. Note that the x-axes for Cy3-TX and Cy5-TX are different from those for TMR-TX and Atto594-TX, due to the much shorter and much longer photobleaching lifetimes, respectively. Among the four trolox-conjugated dye molecules, Cy5-TX exhibited the best performance. Under the 2%O_2 conditions, the Cy5-TX photobleaching lifetime was extended to 39 s with a localization precision of ~25 nm.
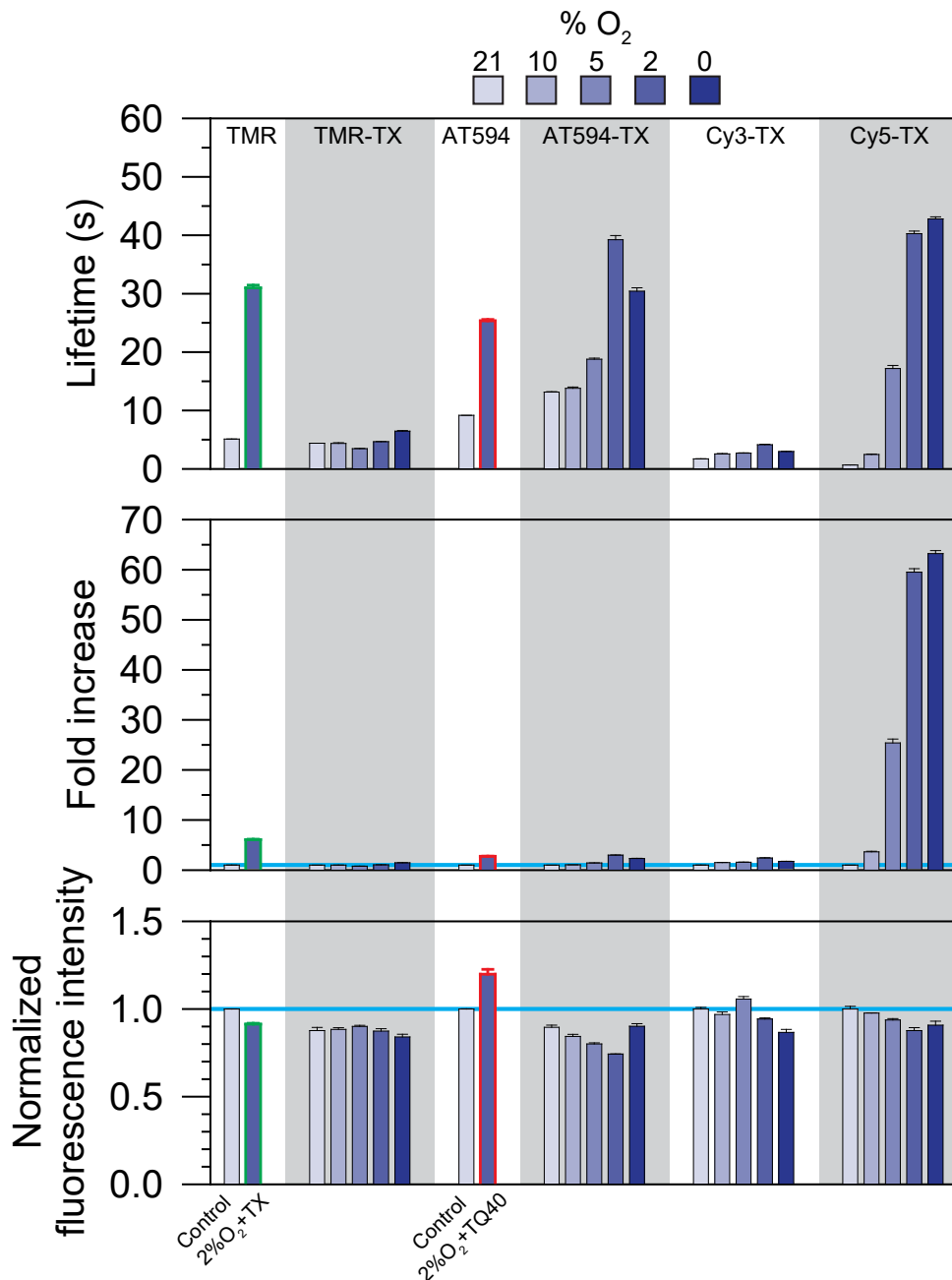
Supplementary Figure 19 | Photobleaching lifetimes (number-counting lifetimes) of trolox-conjugated fluorescent dyes, TMR-, AT594-, Cy3-, and Cy5-TX bound to Halo-CD47 (+ TMR and AT594 without TX conjugation under the control and optimized 2%O₂ + ROXs conditions, for comparison) in the T24-cell-PM under 21, 10, 5, 2, and 0%O₂ atmospheres and single fluorescent-molecule imaging conditions, with localization precisions in the range of 21.7~28.7 nm. The photobleaching lifetime (exponential decay time constant [= mean] ± the standard error), its fold-increase as compared with that under control conditions (21% O₂) (**top and middle, respectively**), and the fluorescence

intensity (mode ± the standard error obtained from the log-normal fitting; **bottom**) are shown. For n, see **Supplementary Table 1**.

The AT594- and Cy5-TX photobleaching lifetimes could be extended to 35~47 s, respectively, under 2 and 0%O_2 conditions. Nevertheless, it should be noted that ST647 under optimized conditions (2%O_2+TQ20) exhibited lifetimes about two-fold longer than the best TX-conjugated dyes employed here. TMR under the optimal 2%O_2 + TX conditions exhibited a longer photobleaching time than TMR-TX, whereas AT594-TX performed better than AT594 under the optimal 2%O_2 + TQ40 conditions.
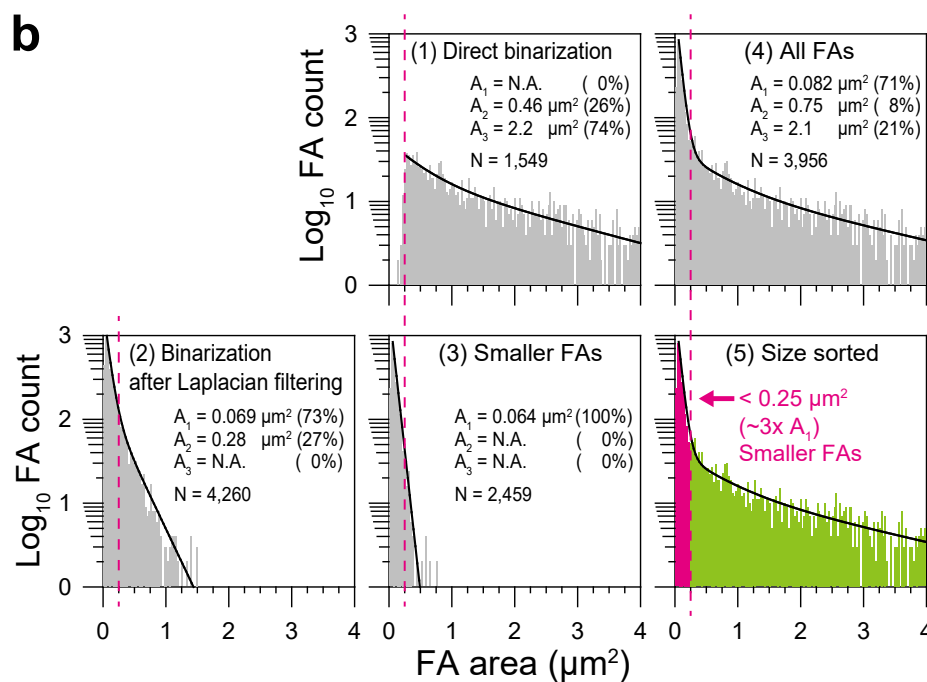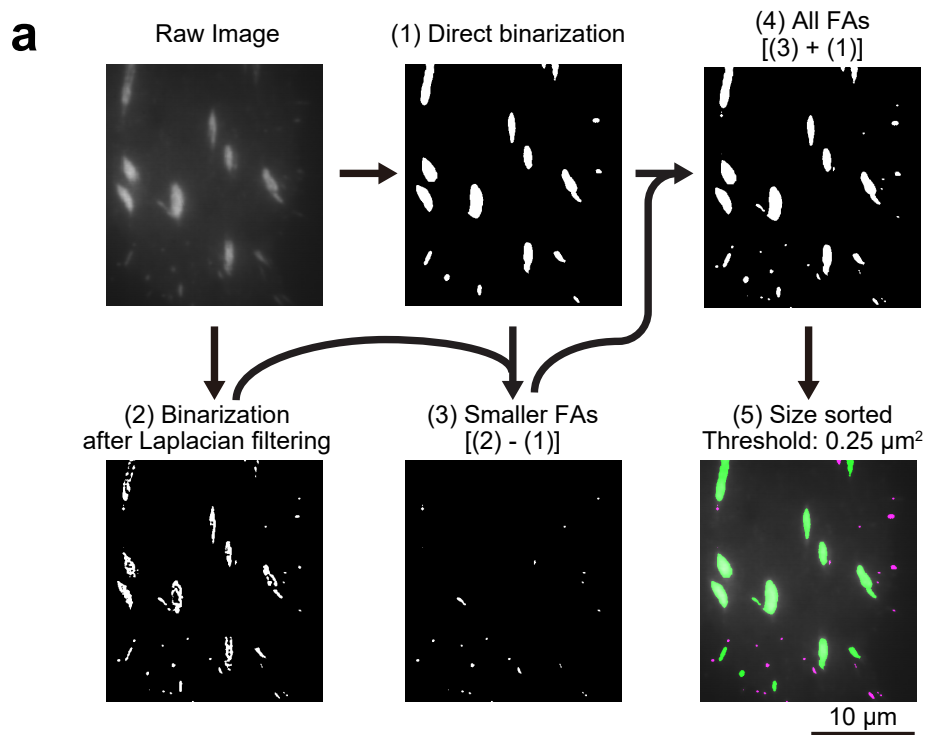
Supplementary Figure 20 | The method for defining the FA region using a binarization method developed for identifying both larger and smaller FAs (larger and smaller than 0.25 µm², respectively).

(**a**) The process of binarization for defining larger and smaller FA regions, employed in the present research. It is shown by using a typical raw image. (**Top, left**) A raw image of

mGFP-paxillin. (**Top, middle**) The binarized image from the raw image (1: "Direct binarization"; see **Online methods** for details). However, the binarized images tended to lose smaller FAs. To circumvent this problem, we first applied a Laplacian filter (5x5 matrix with a value of 24 at the center pixel and -1 in other pixels; total =0) and then a 5x5 pixel median filter to the raw image, and then binarized the image (2: "Binarization after Laplacian filtering", **bottom left**). This procedure enhanced the images of smaller FAs (quantitative results shown in **b**). However, it caused the fragmentation of larger FAs, which we assumed to be artifactual, considering the spatial resolution of normal TIRF microscopy (240 nm). Therefore, to identify only the smaller FAs, in image 2, we removed the FAs that colocalized with the FAs in image 1, to obtain image 3 ("Smaller FAs", **bottom middle**). Finally, to show all of the FAs, we combined (superimposed) image 1 and image 3 (4: "All FAs"). The FAs in image 4 are shown in two colors; those larger and smaller than 0.25 μm^2 are shown in green and magenta, respectively. The basis for this is clarified in **b**.

(**b**) The distributions of the FA area sizes. These distributions could operationally be fitted by an exponential function or the sum of two or three exponential functions. The best number of exponentials for each distribution was determined by both Akaike's and Baysean information criteria. The exponential decay constants (in terms of the area size) are shown in each box (A_1, A_2, and A_3), together with the number of FAs examined (N). The number fractions of each exponential component are shown in parentheses. The boxes are arranged in the same manner as in **a**. The size distribution for image 3 ("Smaller FAs", bottom, middle) could be fitted by a single exponential function with an A_1 of 0.064 μm^2, which is very similar to the A_1 of image 2 (0.069 μm^2). This result supports the idea that the image processing method developed here works well for identifying FAs. Note that the distributions for image 1 ("Direct binarization") and image 3 ("Binarization after Laplacian filtering") lack the smallest (A_1) and largest (A_3) components, respectively. The distribution for image 4 could be fitted by the sum of three exponential functions, with the A_1 value close to that for images 2 and 3, the A_2 value somewhat close to those for images 1 and 2, and the A_3 value close to that for image 1, quantitatively supporting the image processing conducted in **a**. The threshold value between the smaller and larger FAs (magenta and green, respectively, in distribution 5) employed was 0.25 μm^2, which was ~3x A_1 determined in the distribution for image 4. Smaller FAs might include those often called nascent adhesions or focal complexes[22,23].
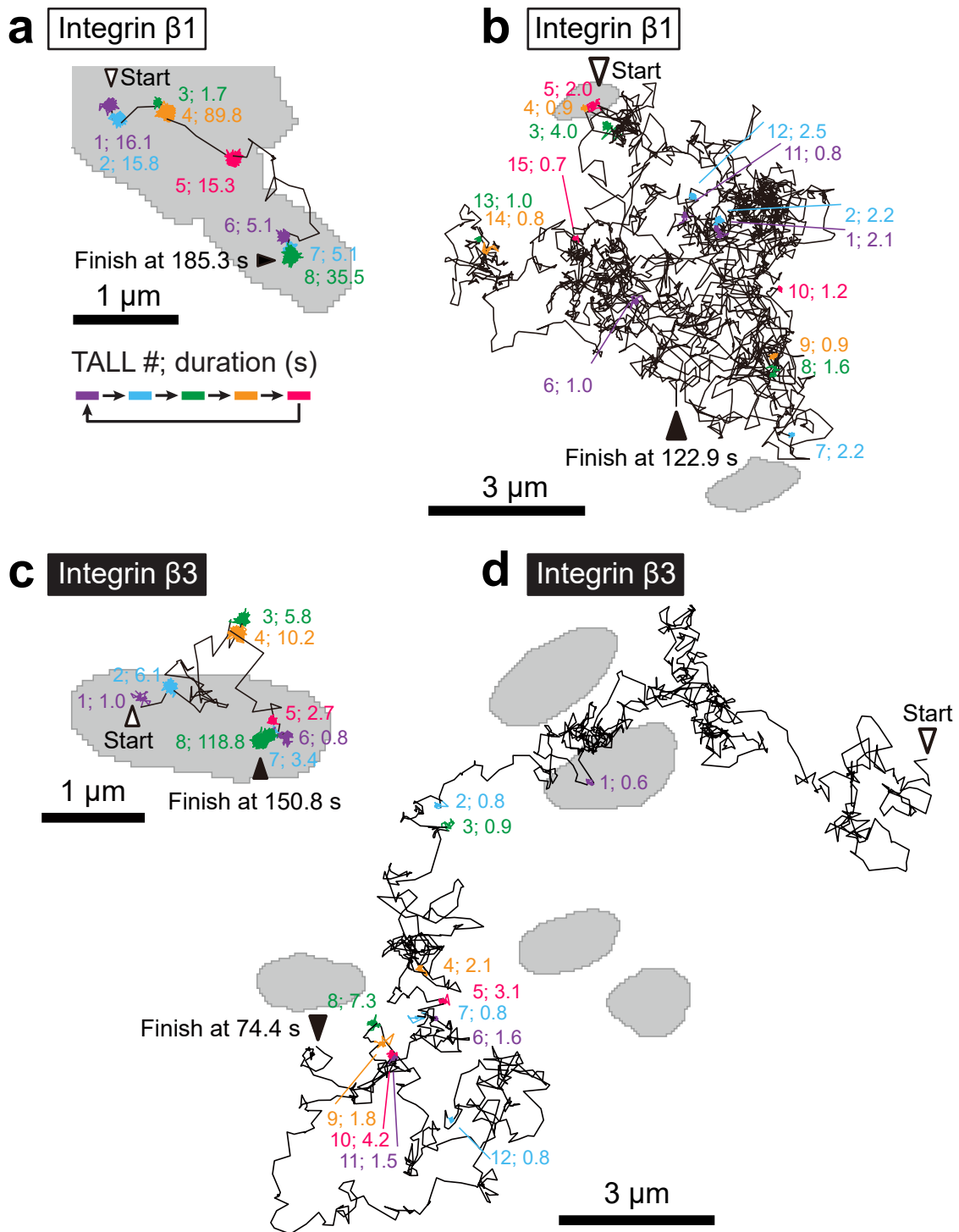
Supplementary Figure 21 | Typical trajectories (additional examples, among 1729 and 2714 trajectories for integrins β1 and β3, respectively) of ST647 bound to ACP-integrin β1 and ACP-integrin β3 using super-long single-molecule tracking under the conditions of 2%O₂+TQ20 in HeLa cells, showing that integrins move in and out of the FA zones, frequently exhibiting temporary immobilization (TALL) events both inside and outside the FA zone.

FA zones (grey areas) are shown as the binarized images of mGFP-paxillin. Trajectories shown in (**a and c**) and (**b and d**) represent those located mostly inside and outside the FA, respectively. The colored parts of the trajectories indicate TALL events, occurring in the order of purple, cyan, green, orange, magenta, and then back to purple. The sequence of TALL occurrences is also shown by the integer, and the number that follows the semicolon indicates the TALL duration in seconds.

Inside FA ☐ **Outside FA**

Integrin β1
$\tau_1 = 0.51 \pm 0.012$ s (6%)
$\tau_2 = 4.3 \pm 0.46$ s (12%)
$\tau_3 = 43 \pm 5.1$ s (82%)

Integrin β3
$\tau_1 = 0.66 \pm 0.016$ s (2%)
$\tau_2 = 9.4 \pm 1.5$ s (13%)
$\tau_3 = 79 \pm 10$ s (85%)

Integrin β1 + Mn^{2+}
$\tau_1 = 0.79 \pm 0.021$ s (8%)
$\tau_2 = 5.2 \pm 0.82$ s (16%)
$\tau_3 = 40 \pm 6.4$ s (76%)

Integrin β3 + Mn^{2+}
$\tau_1 = 0.61 \pm 0.022$ s (2%)
$\tau_2 = 6.2 \pm 1.7$ s (4%)
$\tau_3 = 87 \pm 10$ s (94%)

Integrin β1(D130A)
$\tau_1 = 0.65 \pm 0.060$ s (27%)
$\tau_2 = 5.7 \pm 0.15$ s (73%)
$\tau_3 =$ Non existent

Integrin β3 (N305T)
$\tau_1 = 0.66 \pm 0.016$ s (1%)
$\tau_2 = 8.3 \pm 1.1$ s (11%)
$\tau_3 = 99 \pm 11$ s (88%)

Integrin β1(Y783A/Y795A)
$\tau_1 = 0.48 \pm 0.0078$ s (33%)
$\tau_2 = 4.7 \pm 0.21$ s (67%)
$\tau_3 =$ Non existent

Integrin β1(D130A/Y783A/Y795A)
$\tau_1 = 0.24 \pm 0.012$ s (81%)
$\tau_2 = 1.3 \pm 0.073$ s (19%)
$\tau_3 =$ Non existent

Log % TALL events

TALL duration (s)

Supplementary Figure 22 | The distributions of the TALL durations of integrin β1 (WT, D130A exoplasmic mutant [no RGD binding], the Y783A/Y795A cytoplasmic mutant [no linkage to actin filaments], and the combination of the two [D130A/ Y783A/Y795A], as well as WT with the addition of Mn^{2+}) and integrin β3 (WT with the addition of Mn^{2+}, and the extracellular hybrid domain N305T constitutively active mutant).

(**Solid gray bars and red curves**) TALLs that occurred inside the FA.

(**Open black bars and green curves**) TALLs that occurred outside the FA.

The WT-integrin β1 and β3 histograms indicate that virtually all TALL durations last for less than 100 s, and could operationally be fitted by the sum of three exponential functions, providing three lifetimes for the TALLs that occurred in the FA areas, of (1) < 1 s (<10% of the entire TALL time), (2) several seconds (< 10 s; ~15% of the entire TALL time), and (3) ~40 s for integrin β1 and ~80 s for β3 (~80% of the entire TALL time). To avoid over-fitting, the number of exponential functions for the fitting was optimized with Bayesian and Akaike's information criteria (**Supplementary Table 3**). These data were obtained in the HeLa-cell-PM.

The time constant of each exponential component for the TALLs that occurred inside the FA (mean) with the SEM (estimated as the fitting error of the 68.3% confidence limit) is shown in each box (after correction for the photobleaching lifetime). %Time fraction against the total TALL duration is shown in the parenthesis (for the data of outside the FA, the total number of TALL events and the total number of cells, see **Supplementary Table 2**). The reduction of the bin size from 20 frames to 2 frames only slightly increased the τ_3 lifetime, but hardly affected τ_1 and τ_2 as well as the time fractions of individual components.

The addition of Mn^{2+}, an integrin activator, only slightly affected the TALL behaviors of integrin β1, but its effect on the TALL behaviors of integrin β3 was much greater.

The integrin β1 D130A exoplasmic mutant (no RGD binding) and the Y783A/Y795A cytoplasmic mutant (no linkage to actin filaments due to the lack of binding to talin, tensin, filamin, or kindling) exhibited no τ_3-component. The double mutant combining these two mutations (D130A/Y783A/Y795A) exhibited no τ_3-component and only a small fraction of the τ_2-component. These results suggest that the longest τ_3-component was mainly induced by integrin β1's binding to both the extracellular matrix and actin filaments (via cytoplasmic FA components). The integrin β3 (N305T), the N305T hybrid domain swing-out mutant of integrin β3, exhibited a slightly elongated τ_3, (and an increased time fraction for the τ_3 component, as shown in **Fig. 4b; Supplementary Fig. 24; Supplementary Table 2**), suggesting that the hybrid domain swing-out conformational change is important for inducing the longest TALL events of integrin β3.

■ Inside FA ☐ Outside FA

Integrin β1
$\tau_1 = 0.51 \pm 0.012$ s (6%)
$\tau_2 = 4.3 \pm 0.46$ s (12%)
$\tau_3 = 43 \pm 5.1$ s (82%)

Integrin β3
$\tau_1 = 0.66 \pm 0.016$ s (2%)
$\tau_2 = 9.4 \pm 1.5$ s (13%)
$\tau_3 = 79 \pm 10$ s (85%)

Integrin β1 + 2 µM Y27632 (1 h)
$\tau_1 = 0.40 \pm 0.018$ s (8%)
$\tau_2 = 2.3 \pm 0.16$ s (15%)
$\tau_3 = 19 \pm 1.9$ s (77%)

Integrin β3 + 2 µM Y27632 (1 h)
$\tau_1 = 0.67 \pm 0.015$ s (6%)
$\tau_2 = 7.7 \pm 1.4$ s (16%)
$\tau_3 = 67 \pm 12$ s (78%)

Integrin β1 + 10 µM Y27632 (1 h)
$\tau_1 = 0.52 \pm 0.0070$ s (25%)
$\tau_2 = 4.3 \pm 0.10$ s (75%)
$\tau_3 = $ Non existent

Integrin β3 + 10 µM Y27632 (1 h)
$\tau_1 = 0.46 \pm 0.010$ s (17%)
$\tau_2 = 6.9 \pm 0.27$ s (83%)
$\tau_3 = $ Non existent

Log % TALL events

TALL duration (s)

Supplementary Figure 23 | The distributions of the TALL durations of integrin β1 and β3 before and after the addition of the ROCK inhibitor Y27632.

The figure arrangements and keys are the same as those of **Supplementary Fig. 22**. The treatment of cells with the ROCK inhibitor Y27632 greatly reduced the τ_3 component of integrin β3 in a concentration-dependent manner, just as it did to the τ_3 component of integrin β1 (**Fig. 4c**), suggesting the necessity of the myosin II-induced traction force by way of the actin filament for inducing integrin-based long-term (τ_3 periods) links between the extracellular matrix and the cytoplasmic actin filaments.
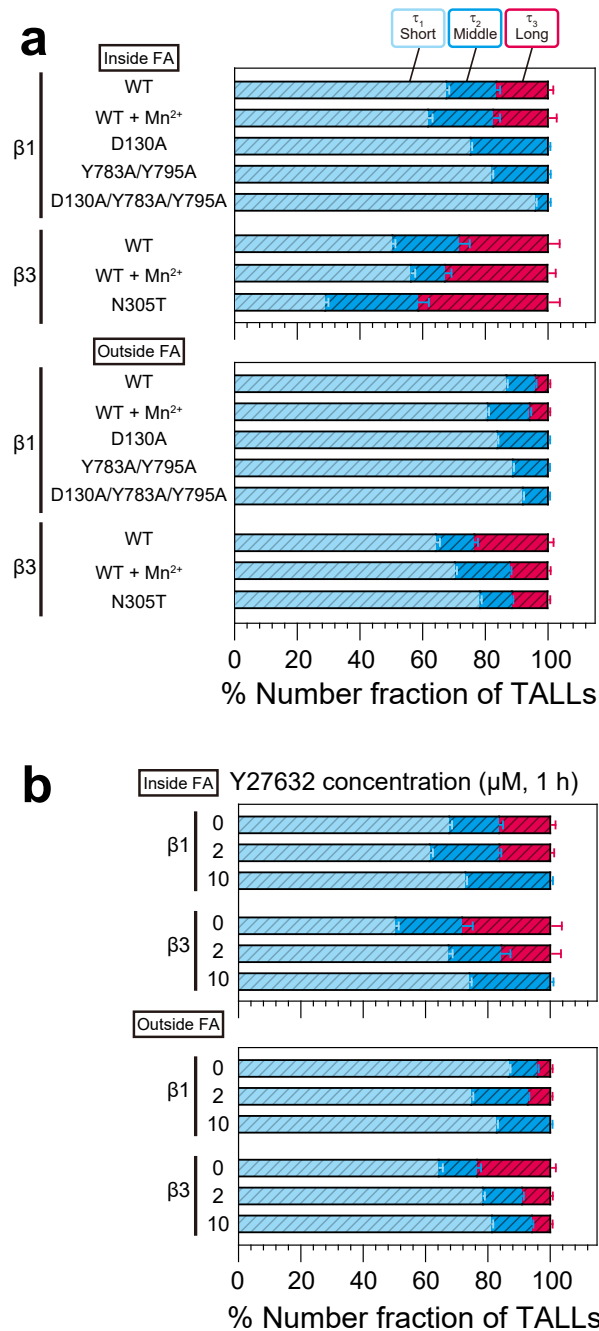
Supplementary Figure 24 | The *number* fractions (in contrast to the *time* fractions shown in **Fig. 4b, c**) of TALL occurrences (rather than TALL periods), of the short, middle, and long TALL events (τ_1, τ_2, and τ_3, components, respectively), determined from the fitting of three exponential functions (**Supplementary Figs. 22 and 23**), showing that shorter TALLs occur very frequently, whereas the time fraction of the entire TALL time is dominated by the τ_3-component (see **Fig. 4b, c**). Mean ± SEM, *n* = 21-45 cells (for *n* for each condition, see **Supplementary Table 2)**. Based on these observations, we propose that single integrin molecules are continually brought to their working sites (*i.e.*, their binding sites on

actin filaments and the ECM) one after another and work as a component for both the force sensor and clutch (partially consistent with previous proposals[38,66-70]); during the short-periods of integrin binding which occurs very often, the integrin-containing molecular complexes work as a sensor for the myosin II-induced tension (as shown later) and when the integrin-containing molecular complexes sense the tension, they start working as a clutch by letting integrin undergo long-term binding to both the ECM and actin filaments for periods on the order of several 10s of seconds. The reason why many integrin molecules must be brought to the binding sites one after another is probably because keeping a single or a few molecules of unbound integrin in small areas proximal to the binding sites would be difficult.
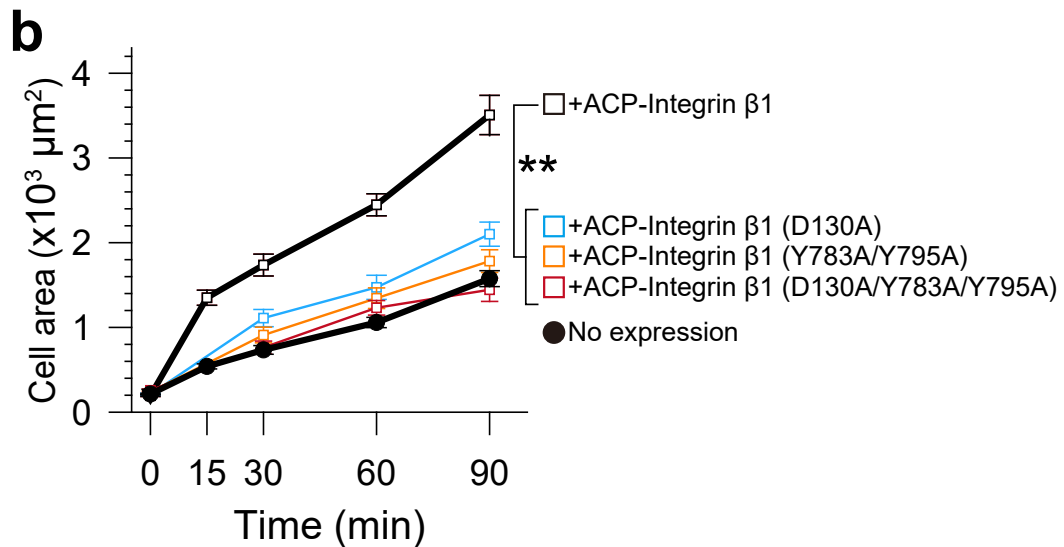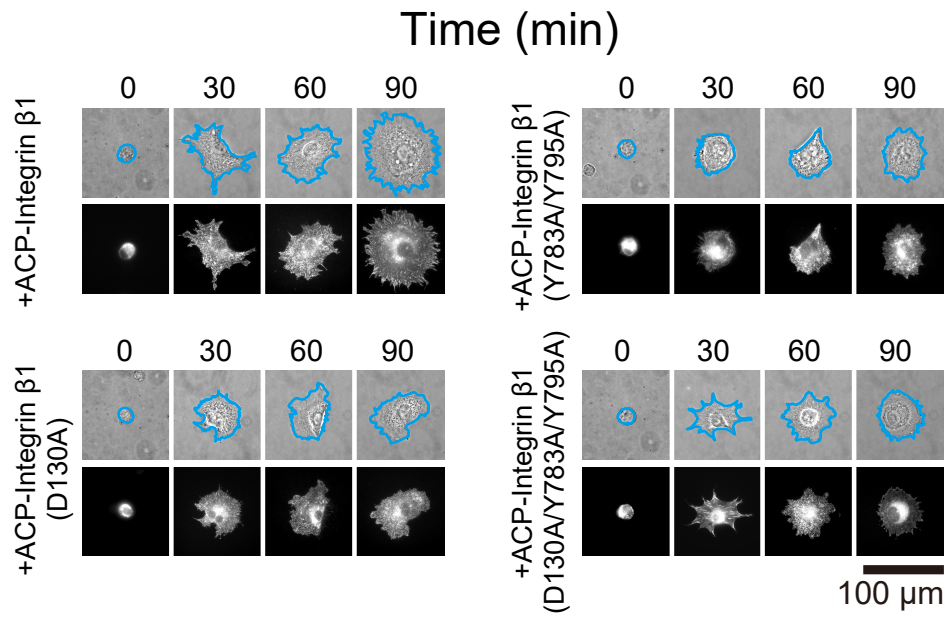
Supplementary Figure 25 | Time courses of the spreading of integrin β1-KO MEF cells after transfection-expression of ACP-integrin β1 and its mutants that fail to bind to the extracellular RGD domain (D130A) and the cytoplasmic FA components, talin, tensin, filamin, and kindling (and thus no binding to actin filaments) (Y783A/Y795A), or that binding to neither of the two (D130A/Y783A/Y795A), showing that none of these mutants aided cell spreading.

(a) Representative (among 20 examined cells) phase-contrast (**top**) and anti-integrin β1 immunofluorescence (epi-fluorescence, **bottom**) images of integrin β1-KO MEFs with or

without transfection-expression of ACP-integrin β1, at 0, 15, 30, 60 and 90 min after plating on FN-coated glass-base dishes. The anti-integrin β1 monoclonal antibody used here (K20) can bind to both active and inactive integrin β1. The cells with similar ACP-integrin β1 (or its mutant) expression levels were selected for comparing the effects of expressing these molecules. Cyan lines in the phase-contrast images indicate cell peripheries, and by measuring the area within the cyan line, the cell area attached to the glass was evaluated (see **b**). Non-transfected integrin β1-KO MEF cells spread more slowly than transfected cells (see **Supplementary Fig. 14**).

(b) Time courses of cell spreading after plating, as measured by the cell area attached to the glass observed by phase-contrast microscopy (mean cell area ± SEM, n = 20 cells). Expression of integrin β1 or ACP-integrin β1 at similar levels enhanced cell spreading after plating, to similar extents (**Supplementary Fig. 14**). Meanwhile, the mutant ACP-integrin β1 molecules failed to aid cell spreading (like the integrin β1 mutants without ACP). **$P <$ 0.01 (two-sided Mann–Whitney U-test; for the actual P values, see **Supplementary Table 5**). Integrin β1-KO MEF cells (control) without additional expression of integrin β1-related molecules can still spread (although slowly) probably due to the presence of other integrins, such as integrin β3[43]).
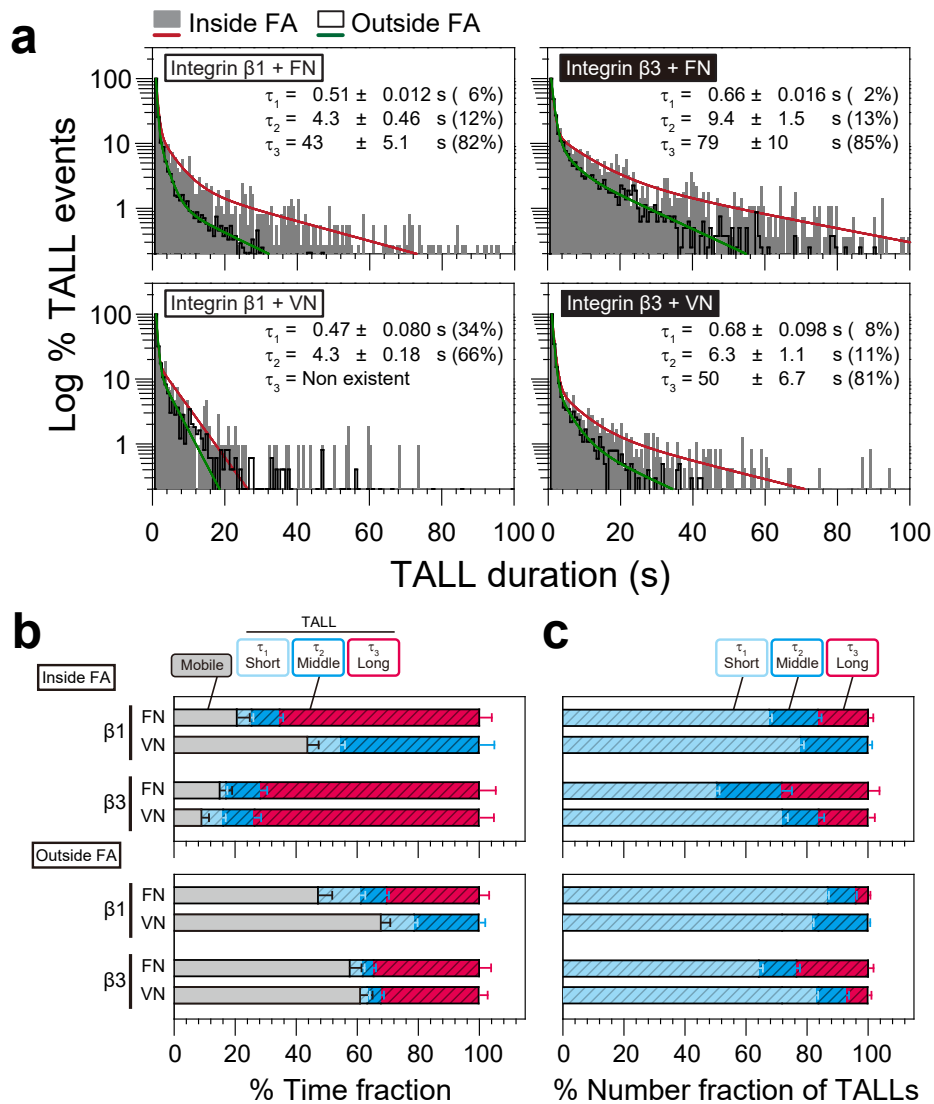
Supplementary Figure 26 | Differences between fibronectin and vitronectin coating for the TALL behaviors of integrins β1 and β3, in terms of **(a)** the distributions of the TALL durations, **(b)** the time fractions and **(c)** the *number* fractions of mobile periods and the three TALL periods (mean ± SEM, n = 21-45 cells (for n for each experiment, see **Supplementary Table 2**). For detailed data, see **Supplementary Note 1** and **Supplementary Tables 2-4**.
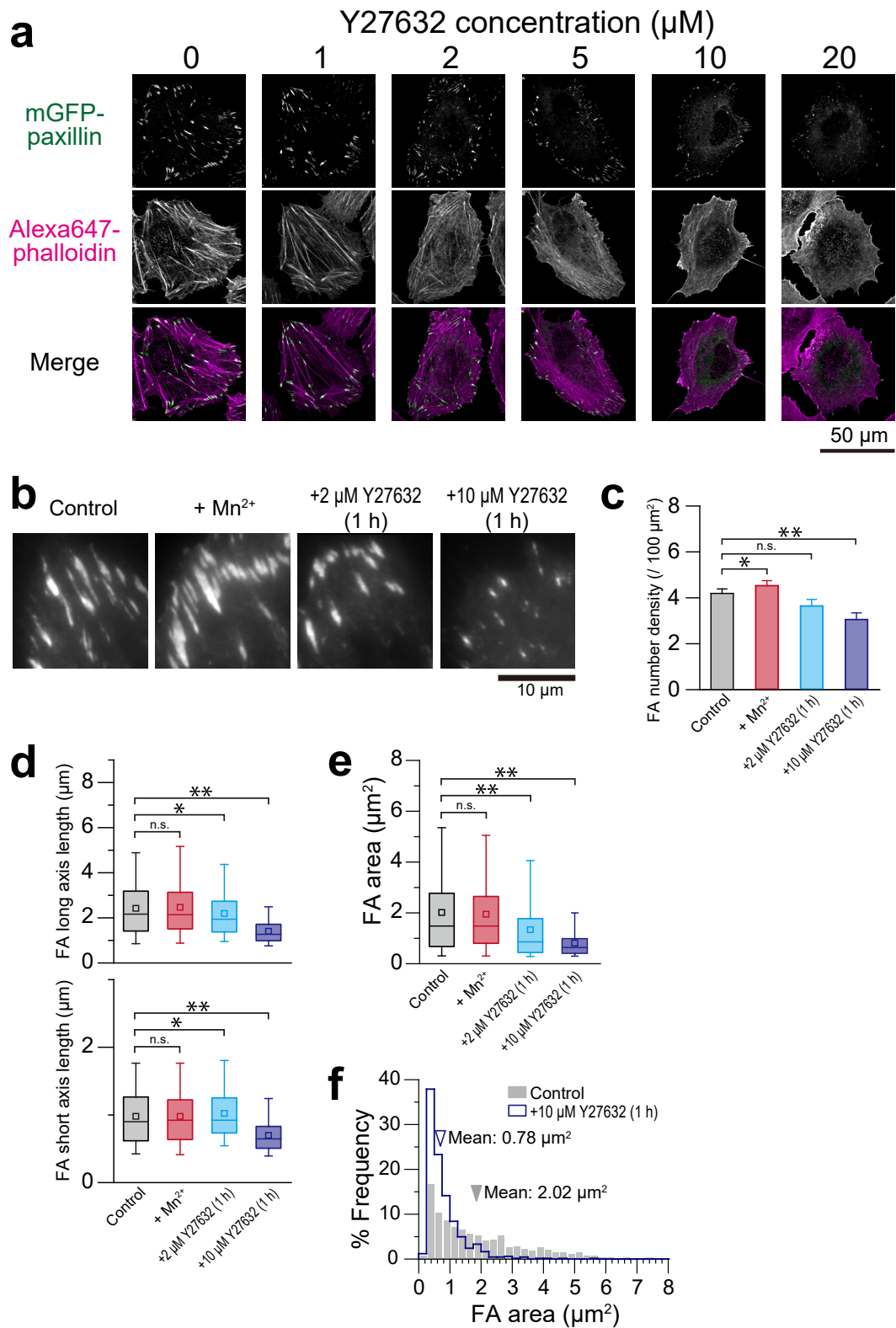
Supplementary Figure 27 | Treatments with Y27632, the ROCK inhibitor, leading to the blockage of myosin II function. Y27632 reduced the number density and the size of larger FAs (> 0.25 µm²) and modified the actin organization.

(a) Representative (among 15 images) confocal images of HeLa cells expressing mGFP-paxillin (as an FA marker) incubated in T-HBSS containing 0, 1, 2, 5, and 10 μM Y27632 for 1 h, followed by 4%-paraformaldehyde fixation, permeabilization, and staining with Alexa647-phalloidin (labeling actin stress fibers).

(b) Representative (among 30 images) TIRF images of mGFP-paxillin in HeLa cells incubated with 1 mM Mn^{2+}, or 2 or 10 μM Y27632 for 1 h.

(c) The number density of larger FAs (> 0.25 $μm^2$) evaluated from the TIRF images of mGFP-paxillin (Mean ± SEM, n = 30 cells). Incubation with Mn^{2+} slightly increased the FA density, whereas incubation with Y27632 slightly decreased it. The statistical tests were performed using the two-sided Welch's T test: [P for control vs. +Mn^{2+}, 2 μM Y27632, and 10 μM Y27632, respectively] = 0.048, 0.34, and 1.3 x 10^{-4}. *: P < 0.05, **: P < 0.01, n.s.: P > 0.05 (the same for **d** and **e**).

(d) Box plots of the FA long-axis (top) and short-axis (bottom) of the FAs larger than 0.25 $μm^2$ (Mean ± SEM: n = 828, 926, 659, and 665 FAs for control, +Mn^{2+}, 2 μM Y27632, and 10 μM Y27632, respectively). Boxes extend from the 25th to 75th percentiles, with a line at the median and an internal box at the mean. Whiskers extend from the 5th to 95th percentiles. The incubation with 10 μM Y27632 for 1 h significantly decreased both the long and short axes of the FA. The statistical tests were performed using the two-sided Mann–Whitney U test: P for control vs. [+Mn^{2+}, 2 μM Y27632, 10 μM Y27632] = [0.75, 0.018, 4.8 x 10^{-10}] for the long-axis, and [0.96, 0.011, 9.0 x 10^{-15}] for the short-axis.

(e) Box plots of the areas of larger FAs (> 0.25 $μm^2$) after 1-h incubations with 1 mM Mn^{2+}, or 2 or 10 μM Y27632 for 1 h (the keys and the numbers of inspected FAs are the same as those in (**d**)). The statistical tests were performed using the two-sided Mann–Whitney U test: P for control vs. [+Mn^{2+}, 2 μM Y27632, 10 μM Y27632] = [0.96, 1.4 x 10^{-12}, 3.6 x 10^{-18}].

(f) Distributions of individual FA areas (FAs with areas > 0.25 $μm^2$) with (grey bars) and without (open blue bars) an incubation with 10 μM Y27632 for 1 h.
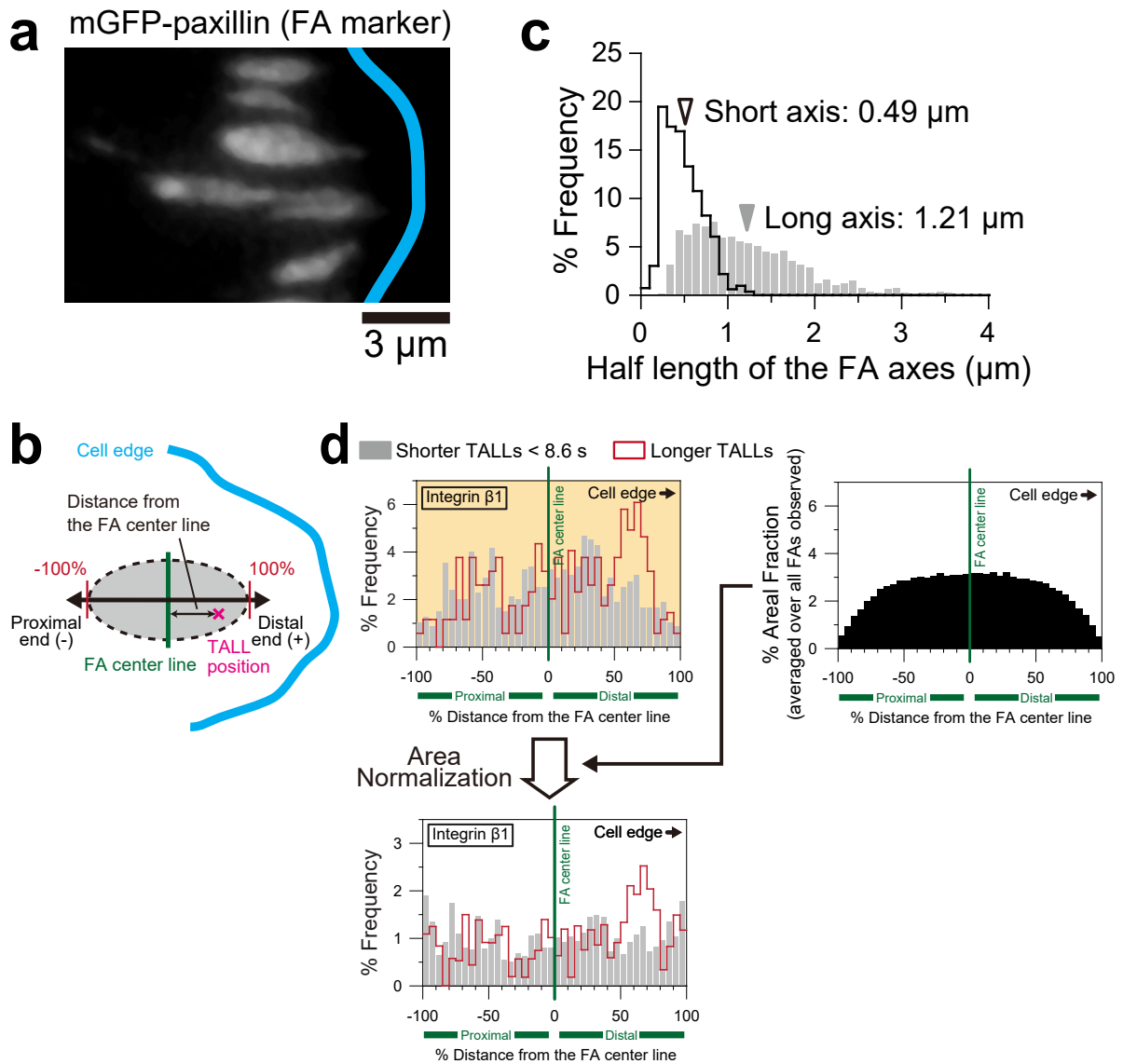
Supplementary Figure 28 | The method to describe the spatial distributions of the TALL locations along the FA long axis (relative to the half-axis length).

(a) A representative TIRF image of FA marked by mGFP-paxillin. The cyan curve represents the cell edge.

(b) Schematic drawing of the FA zone (the grey area surrounded by the black dashed curve) modeled as an ellipse with the short and long axes, shown together with the cell periphery (cyan curve). In the following analysis of TALL locations in FAs, each FA region was modeled as an ellipse. For this purpose, the binarized images of FAs (**Supplementary Fig. 20**) were imported into Matlab. Ellipses were fit to each isolated FA region using the "BWLABEL and REGIONPROPS" functions of Matlab, and the major and minor axes were determined[71,72].

The position where an integrin molecule undergoes TALL is shown by a magenta cross, and its distance to the short axis (along the long axis) is shown by the smaller black arrow. The positive (negative) sign before the distance indicates that the TALL location is on the distal (proximal) side in the FA.

(c) Distributions of the half-lengths of FAs' long and short axes. Triangles indicate mean values. n = 821.

(d) (**top**) The spatial distribution of TALL frequency plotted as a function of the % distance along the long axis (relative to the half-length of the long axis, from the FA center line). Another useful display of the spatial TALL distribution employed here was the frequency per unit area in the FA (**bottom**), which was obtained by normalizing the original distribution (**top**) with the area size distributions (*i.e.*, against the spatially random TALL occurrences in the FA region modeled as in **b**; **right**).

In the present report, we show the histograms both before normalization (proportional to the actual TALL frequency at a given distance from the center line) and after normalization (proportional to the TALL frequency in a unit area at a given distance).

Shorter TALLs < 8.6 s (Integrin β1) or 18.8 s (Integrin β3) ▢ **Longer TALLs**

a TALL spatial distribution (relative location) without area normalization

b TALL spatial distribution (relative location) after area normalization

c TALL spatial distribution (real distance) without area normalization
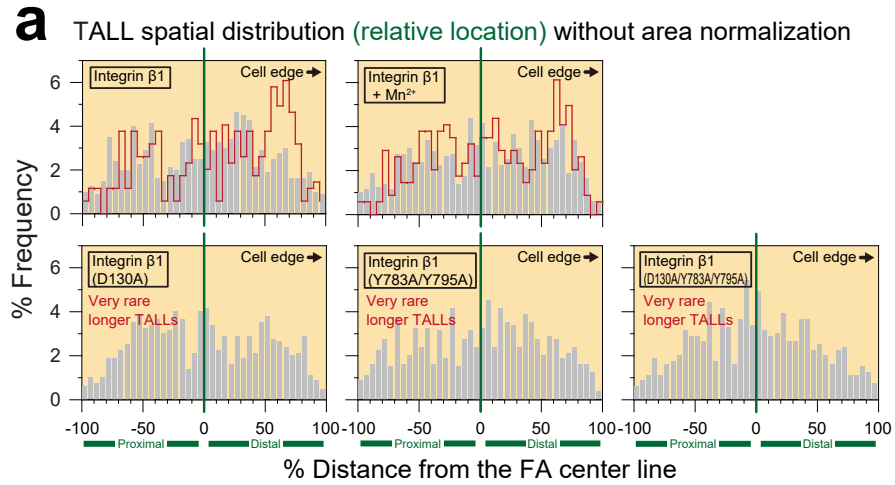
d TALL spatial distribution (real distance) after area normalization
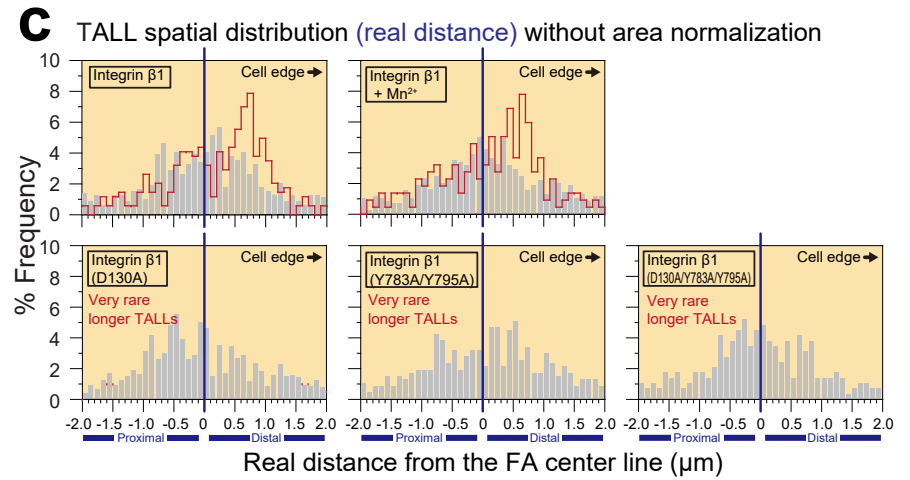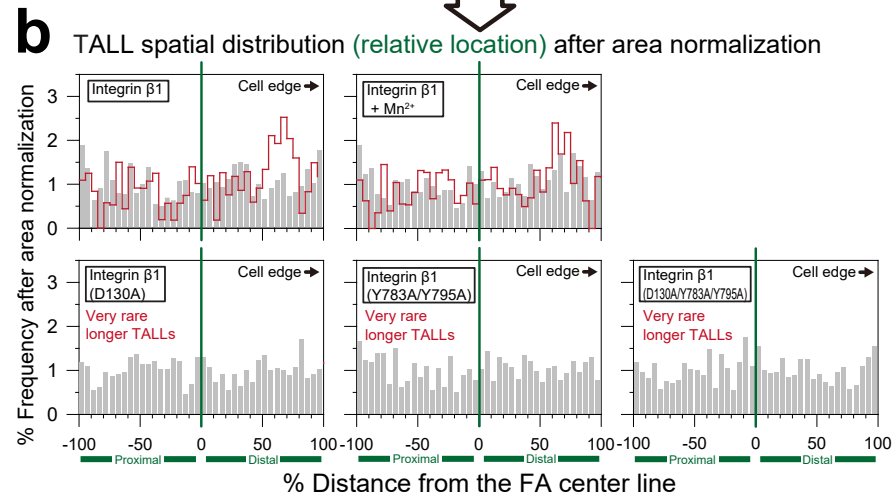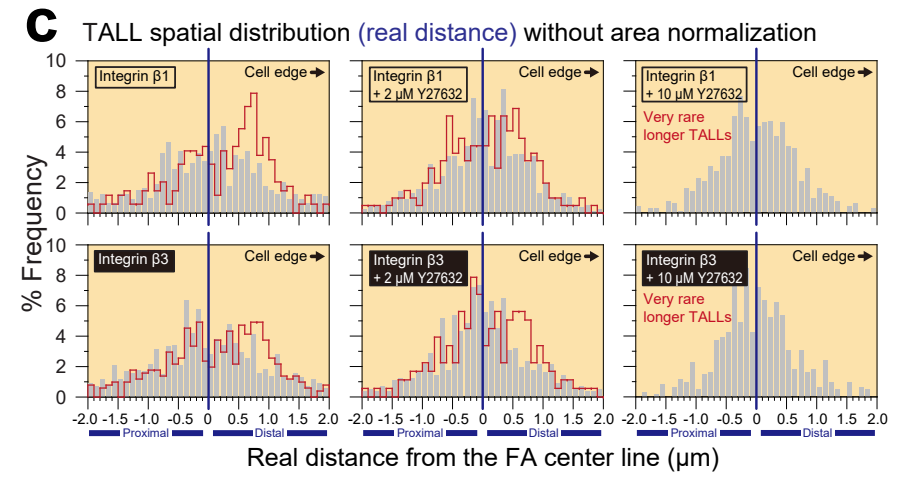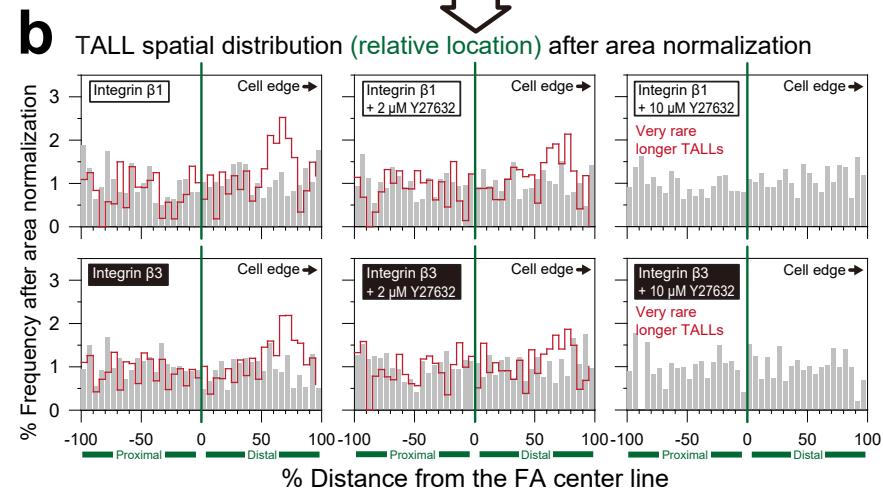
Area normalization

Supplementary Figure 29 | Longer TALLs of integrin β1 most frequently occurred two-thirds of the distance away from the FA center toward the distal end, whereas three integrin β1 mutants (no RGD binding and/or no linkage to actin filaments) rarely exhibited longer TALLs.

Frequency of TALLs of integrins in the FA, plotted as a function of the location along the FA long axis. The distributions without area normalization are shown in **a** and **c**, whereas **b** and **d** show the distributions after area normalization (the frequency per unit area). The x-axes in **a** and **b** indicate the distance relative to the half-length of the long axis, whereas those in **c** and **d** indicate the actual distances (with positive and negative signs) from the short axes. For the total number of TALLs examined for each molecule, see **Supplementary Table 2**.

The spatial distributions of longer TALLs of WT integrin β1 (also after the addition of Mn^{2+}) showed a clear peak around two-thirds of the distance away from the FA center toward the distal end (or ~0.7 μm away from the FA center toward the distal end). Note that these peaks were found even in the distributions without area normalization. For integrin β1's D130A, Y783A/Y795A, and D130A/Y783A/Y795A mutants, data of longer TALLs could not be plotted, because they hardly exhibited longer TALLs.

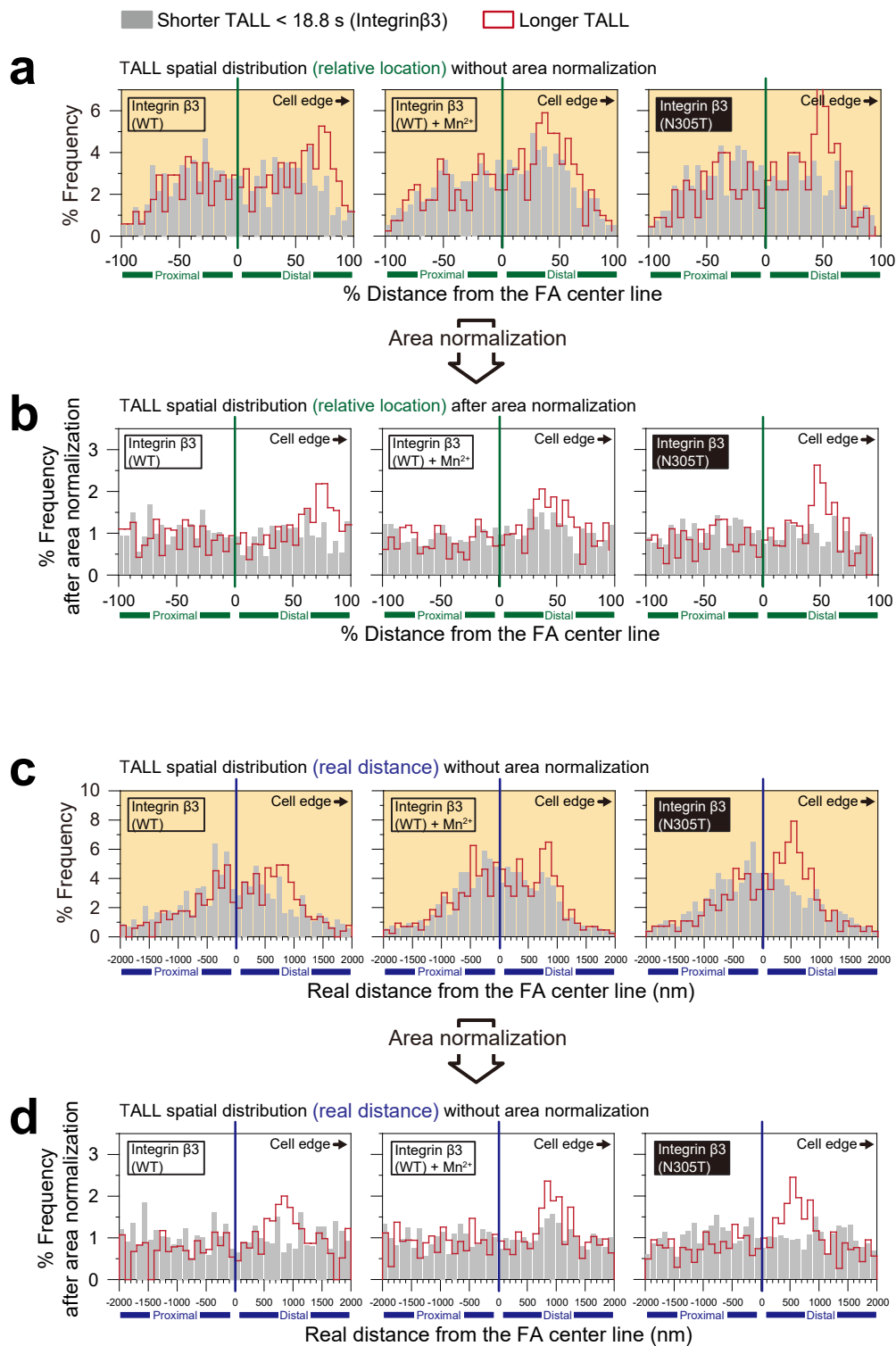**Supplementary Figure 30 |** The effect of the Y27632 addition on the spatial distributions of TALLs in the FA for integrin β1 and β3.

Frequencies of TALLs of integrins in the FA are plotted as a function of the location along the FA long axis. For four displays **a** - **d**, see the descriptions in the caption to **Supplementary Fig. 29**. For the total number of TALLs examined for each molecule, see **Supplementary Table 2**. The spatial distributions of longer TALLs of integrin β3 showed peaks similar to those of integrin β1. The addition of 10 µM Y27632 almost entirely eliminated the longer TALLs.
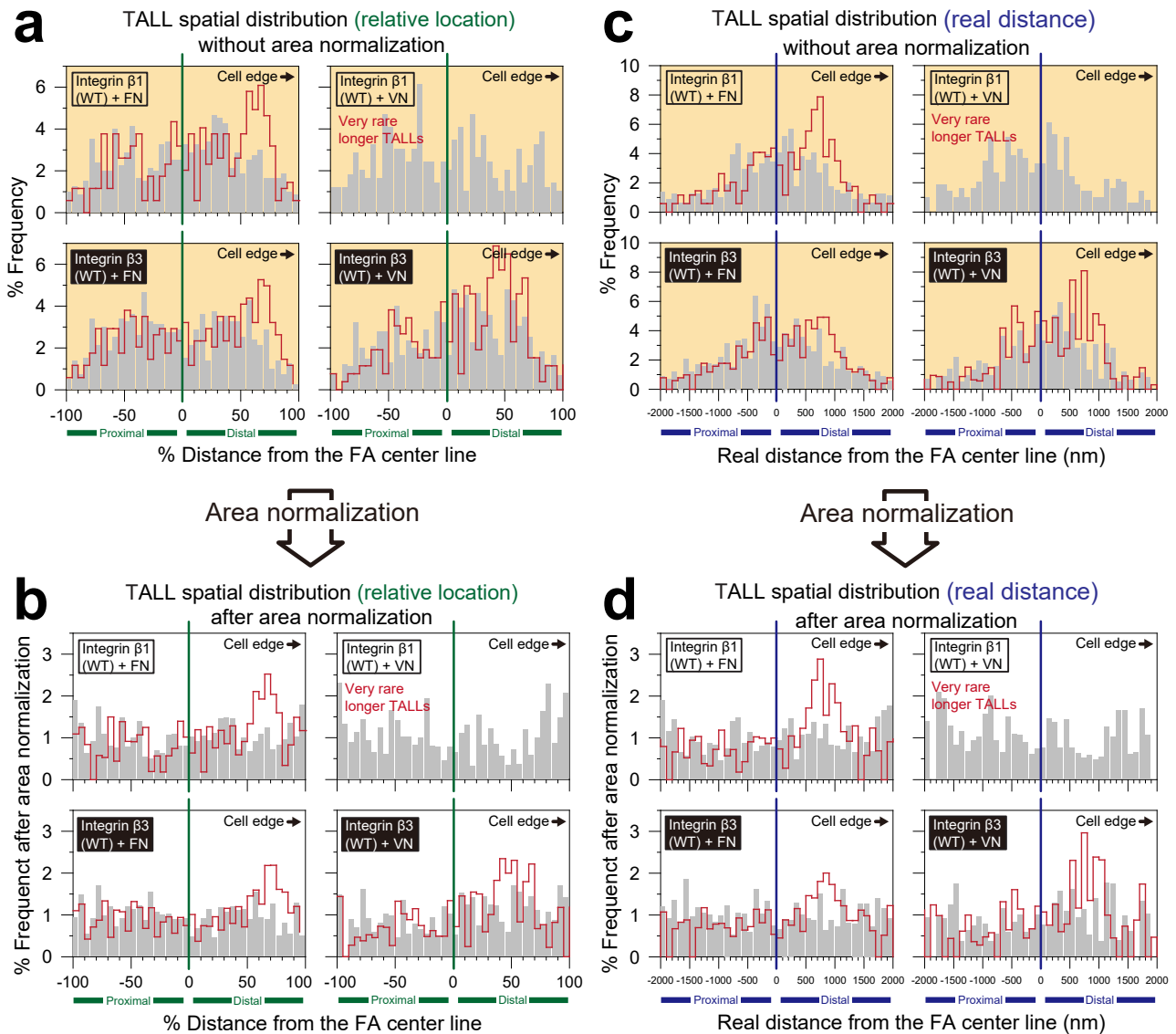
Supplementary Figure 31 | Differences between fibronectin and vitronectin coating for the TALL behaviors of integrins β1 and β3, in terms of the spatial distribution of integrin's longer and shorter TALLs in the FA. For four displays **a** - **d**, see the descriptions in the caption to **Supplementary Fig. 29**. For the total number of TALLs examined for each molecule, see **Supplementary Table 2**.
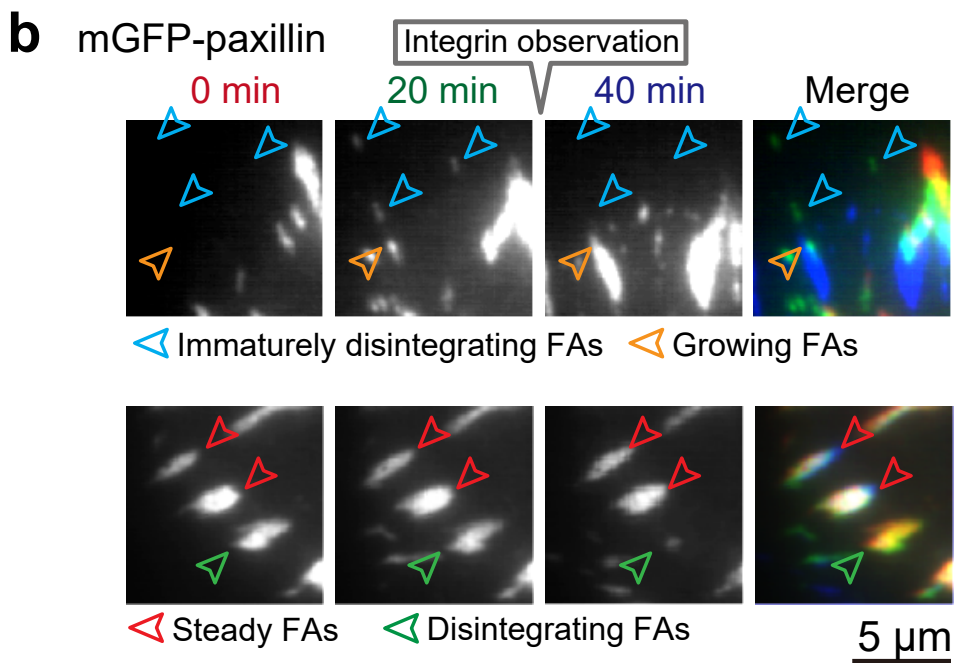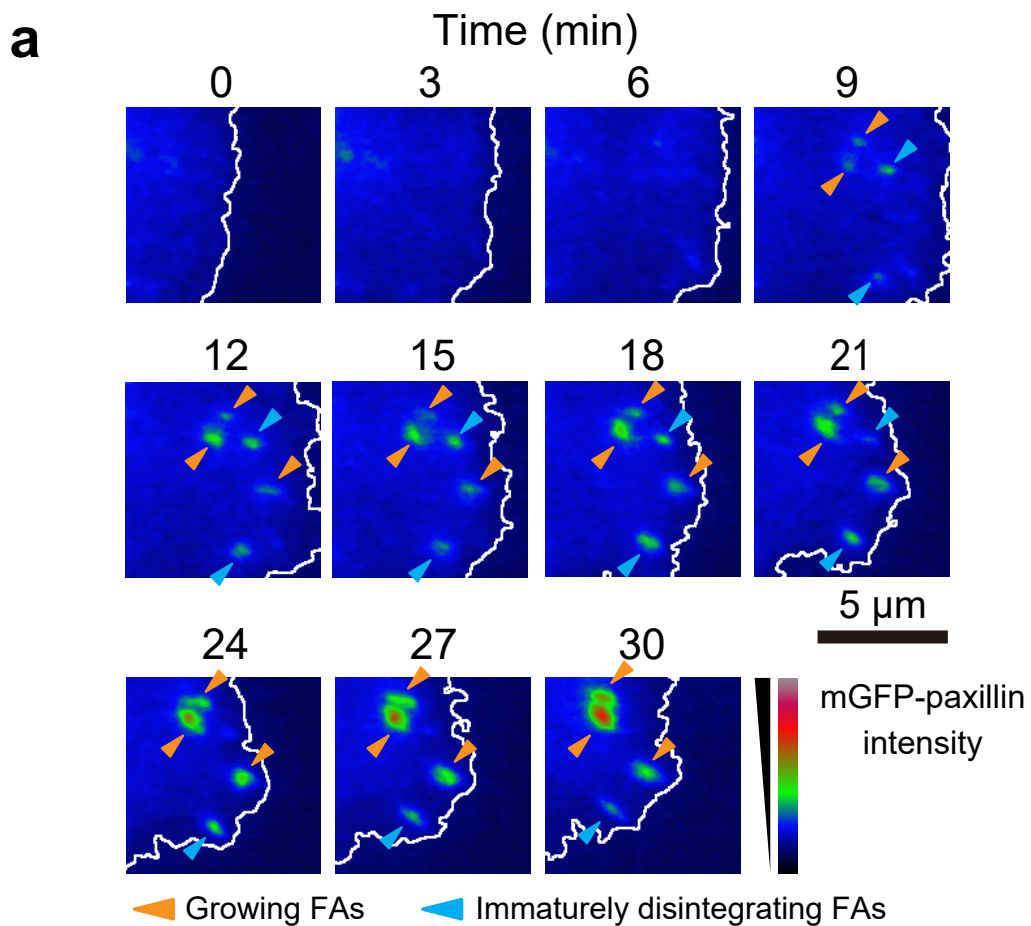
Supplementary Figure 32 | The effect of the Mn²⁺ addition and the constitutively active N305T mutation on the spatial distributions of longer and shorter TALLs in the FA for integrin β3. For four displays **a - d**, see the descriptions in the caption to **Supplementary Fig. 29**. For the total number of TALLs examined for each molecule, see **Supplementary Table 2**.
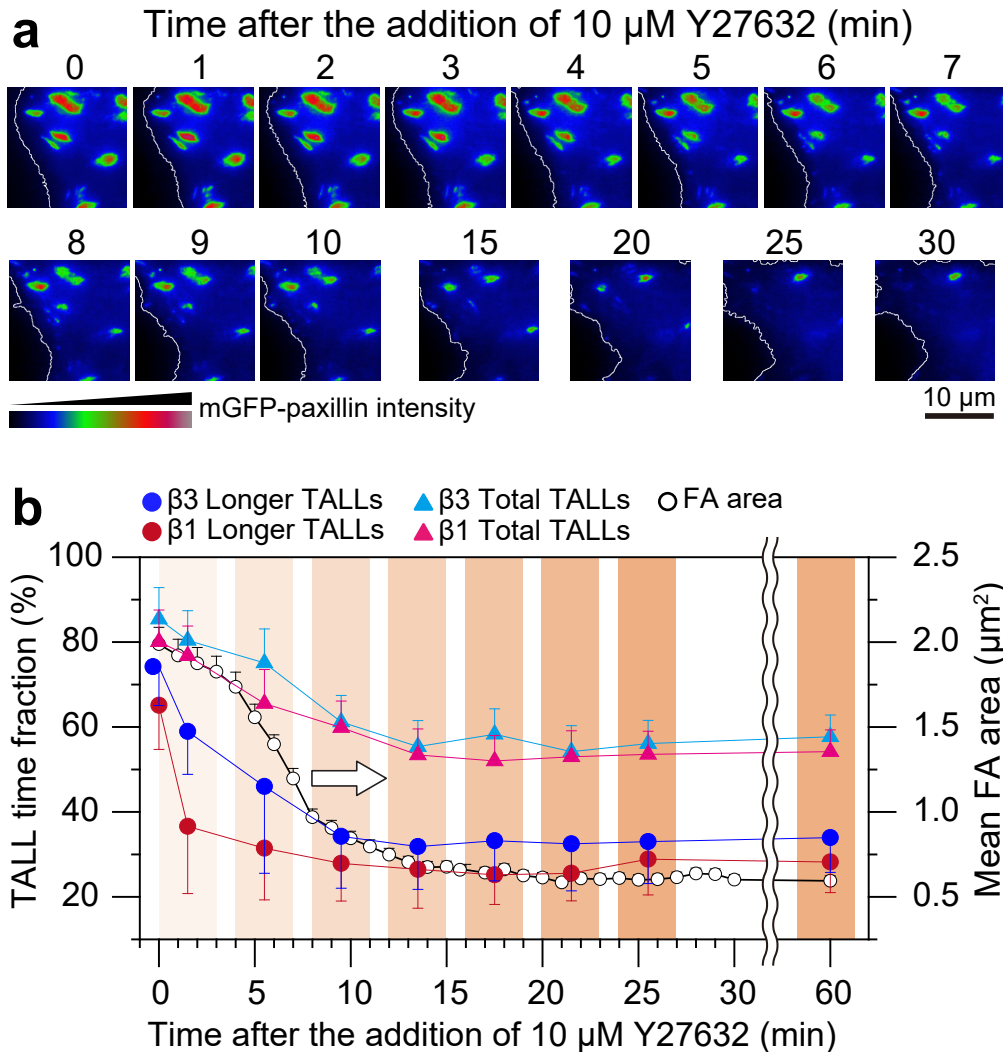
Supplementary Figure 33 | The cell treatment with 10 µM Y27632 induced a prompt and large reduction in the time fraction of integrin's longer TALLs (against the entire trajectory length), followed by a decrease of the mean FA area (visualized with mGFP-paxillin). These results suggest that integrins' longer TALLs might be important for maintaining the FA architecture.

(a) Representative time series of TIRF images of FAs visualized with mGFP-paxillin after the addition of 10 µM Y27632 (representative among 32 independent experiments). White curves represent the cell edges. See also **Supplementary Video 6**.
(b) The time courses of the time fractions of integrins' longer TALLs and total TALLs (against the entire trajectory length; see the y-axis on the left), as well as the mean FA area after the addition of 10 µM Y27632 (see the y-axis on the right). FA images were obtained every 1 min. Individual FA areas were first averaged within one cell, and then further

averaged over the results obtained from all of the observed cells (mean ± SEM, number of cells = 32). Integrin's trajectories were obtained during 3 min, starting from time 0, 4, 8, 12, 16, 20, 24 and 59.5 min after Y27632 addition, and the TALL time fractions were evaluated (mean ± SEM, n = 10 cells). For clarity, error bars (SEMs) are shown in only one direction.

a

Time (min)

0 3 6 9

12 15 18 21

5 μm

24 27 30

mGFP-paxillin intensity

◀ Growing FAs ◀ Immaturely disintegrating FAs

b mGFP-paxillin

Integrin observation

0 min 20 min 40 min Merge

◁ Immaturely disintegrating FAs ◁ Growing FAs

◁ Steady FAs ◁ Disintegrating FAs

5 μm

Supplementary Figure 34 | FA turnover and dynamics.

(a) Representative (among 10 independent experiments) time-dependent changes of FAs on the basal PM visualized with mGFP-paxillin, showing that FAs form, disassemble, and slowly migrate continually in a matter of 30 min. White curves represent the cell edges. The original video is shown in **Supplementary Video 7**.

(b) Representative (among 10 independent experiments) time-lapse images of mGFP-paxillin-marked FAs. FAs were classified into larger or smaller ones, based on sizes larger or smaller than 0.25 μm^2, respectively (**Supplementary Fig. 20**). The four phases from the formation to the disintegration of FAs were defined as follows, based on the observations of FAs for 40 min: (1) growing FA, the FA that grew from a smaller FA to a larger FA (orange); (2) steady FA, the FA that was a larger FA at time 0, and remained as a larger FA (red); (3) disintegrating FA, FA that was a larger FA at time 0, and became a smaller FA or disappeared later (green); and (4) immaturely disintegrating FA, the FA that was a smaller FA at time 0, and disappeared later (blue). FAs that were smaller FAs at time 0 and remained as smaller FAs for 40 min scarcely existed, and therefore these FAs were ignored in this definition of the four phases of FA formation and disintegration.
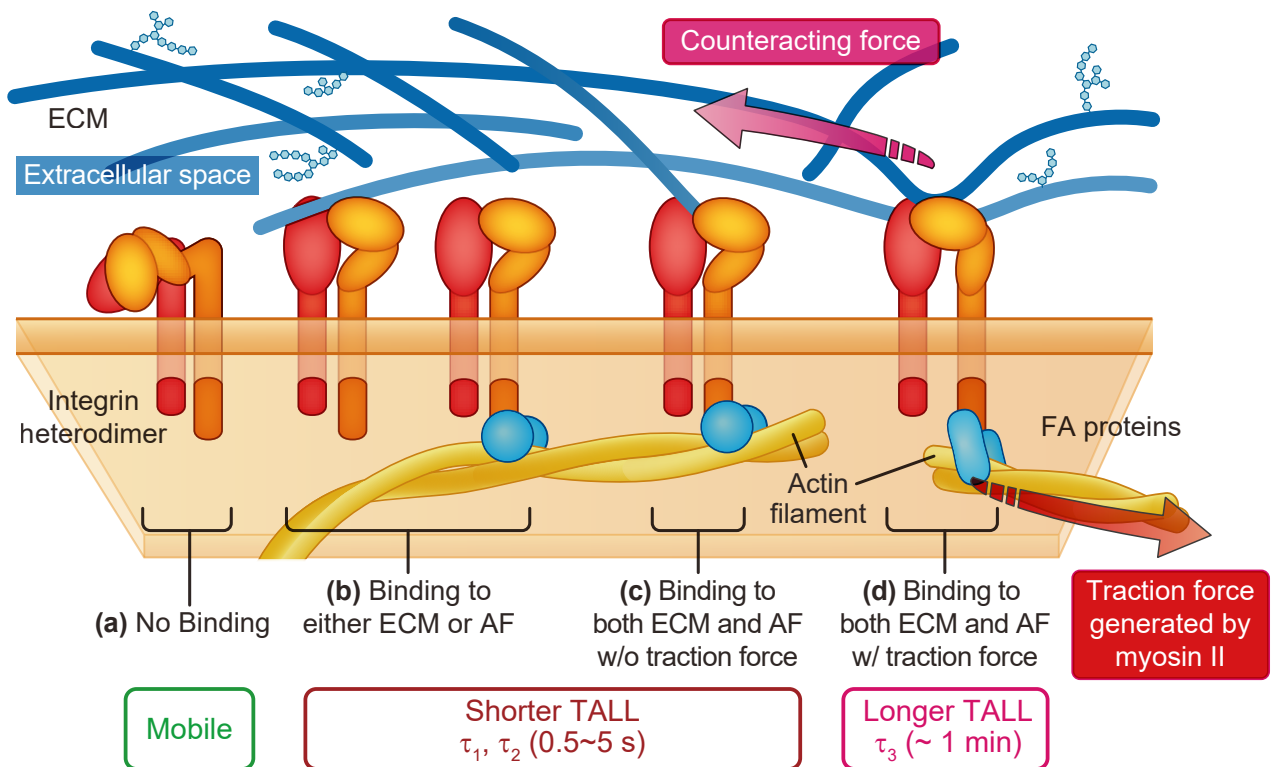
Supplementary Figure 35 | Schematic figure showing how integrin heterodimers (α + β subunit; red and orange, respectively) link the ECM and the intracellular actin filaments.

(a) Integrins undergo diffusion in the PM, both outside and inside the FA, when they do not bind to the ECM or actin filaments (AF). **(b)** When integrins bind to either the ECM or AF, shorter TALLs of integrins (with lifetimes on the order of 0.5 - 5 s) take place. **(c)** Even when integrins bind to both the ECM and AF, the TALL lifetime do not change appreciably (the experiments employing a ROCK inhibitor Y27632). **(d)** When integrins bind to both the ECM and AF and traction force is exerted on the bound integrins, longer TALLs (with a lifetime of ~1 min) are induced. Namely, when each integrin dimer enters the FA region and binds to both the ECM and AF, and if it senses the force generated by myosin II, it mechanically couples the ECM and AF for ~1 min, and then departs from the binding site. These results indicate that the longer TALLs found in this study are the key molecular events for cell binding to the ECM.

  We found that longer TALLs occur most often two-thirds of the distance away from the FA center toward the distal end. Larger traction forces would involve more frequent recruitment of integrin dimers; they would arrive one after another, each linking the ECM

and AF for periods on the order of 1 min. Since many integrin molecules would participate in crosslinking the ECM and AF, overall, the long-term linking of the ECM and AF could be achieved. This way, regulating the cell's binding to the ECM would be regulated more readily, rather than depending on long-term binding of much smaller numbers of integrin molecules. The spatial variations within the FA, in terms of the biochemical activation levels and the dynamics of vinculin and paxillin, as well as vinculin's z-axis distribution (spread toward the cytoplasm), have been reported[73-75].

In this figure, note the three major conformations of an integrin molecule (dimers). **(a)** When integrin is not bound by ECM or AF and non-activated, the integrin dimer takes the "bent" conformation. **(b, c)** The ECM binding[76,77], cytoplasmic FA-protein binding (leading to the binding to AF[78]), or Mn^{2+} addition[76,79] induces conformational changes to the "stand (extended)" conformation. **(d)** When traction force is exerted on integrin, integrin further undergoes conformational changes in the hybrid head domain, from "closed" to "open" conformational changes, due to the swing out of the β subunit[33-35,44]. Namely, two major conformational changes are required to fully activate integrins; from the inactive "bent-closed" conformation to the semi-active "stand-closed" conformation, and then to the fully active "stand-open" conformation[33-35,44,80-82].

pOStet15T3-SP(CD47)-SG-CD47

Kozack · Signal peptide from CD47 · ACP · SG linker · CD47 without signal peptide

| | | | M | … | A | V | D | T | G | M | … | A | S | G | G | G | G | S | T | S | C | T | Q | … | * | |
| gg | cgc | gcc | ggt | acc | ATG | … | GCT | gtc | gac | acc | ggt | ATG | … | GCG | AGC | GGA | GGA | GGA | GGA | AGC | act | agt | tgt | aca | CAG | … | TAG | ctg | cag |

AscI · KpnI · SalI · AgeI · SpeI · BsrGI · PstI

pOStet15T3-SP(IL6)-Halo7-SGX3-CD47

Kozack · Signal peptide from interleukin6 · Halo7 · SGX3 linker · CD47 without signal peptide

M … P V D M … G S G G G G S G G G G S G G G G T S C T Q … *
gg cgc gcc acc ATG … CCA acc ggt ATG … GGC TCT GGT GGC GGA GGG AGT GGC GGA GGT GGG TCA GGA GGT GGA GGC act agt tgt aca CAG … TAG ctg cag

AscI · AgeI · SpeI · BsrGI · PstI

pOStet15T3-CD47-SGX3-Halo7, pEGFPN1-integrin β1-SGX3-Halo7

Kozack · CD47 or Integrin β1 · SGX3 linker · Halo7

M … X E F C T T S S G G G G S G G G G S G G G G M … *
ggt acc ATG … XXX gaa ttc tgt aca act agt TCT GGT GGC GGA GGG AGT GGC GGA GGT GGG TCA GGA GGT GGA GGC ATG … TAA GCG GCC GC

KpnI · EcoRI · BsrGI · SpeI · NotI

**pOSte15T3-CD47-SG-mEGFP, pEGFPN1-integrin β1-SG-mEGFP**

Kozack · CD47 or Integrin β1 · SG linker · mEGFP

M … X E F C T T S S G G G G S M … *
ggt acc ATG … XXX gaa ttc tgt aca act agt AGC GGA GGA GGA GGA AGC ATG … TAA GCG GCC GC

KpnI · EcoRI · BsrGI · SpeI · NotI

pEGFPN1-SP(CD8)-ACP-SG-integrins

Kozack · Signal peptide from CD8 · ACP · SG linker · Integrins without singal peptide

M … A T G M … A S G G G G S T S R S X … *
gg tac cgg cgc gcc agc ATG … GCC acc ggt ATG … GCG TCT GGT GGC GGA GGG AGT act agt aga tct XXX … TAG gat atc gcg gcc gc

KpnI · AscI · AgeI · SpeI · BglII · EcoRV · NotI

Supplementary Figure 36 | Schematic structures of the parts of the cDNA constructs used in this study, showing the multiple cloning sites, inserted tag proteins, linkers, and the target proteins. See **Online Methods**.
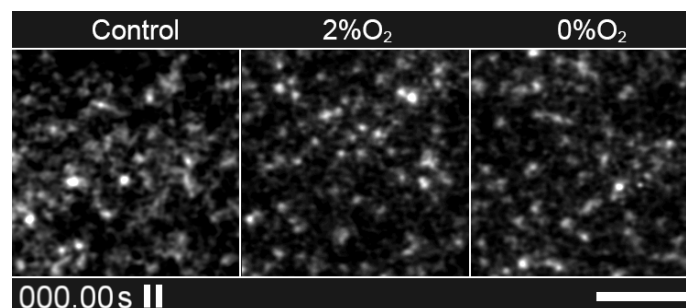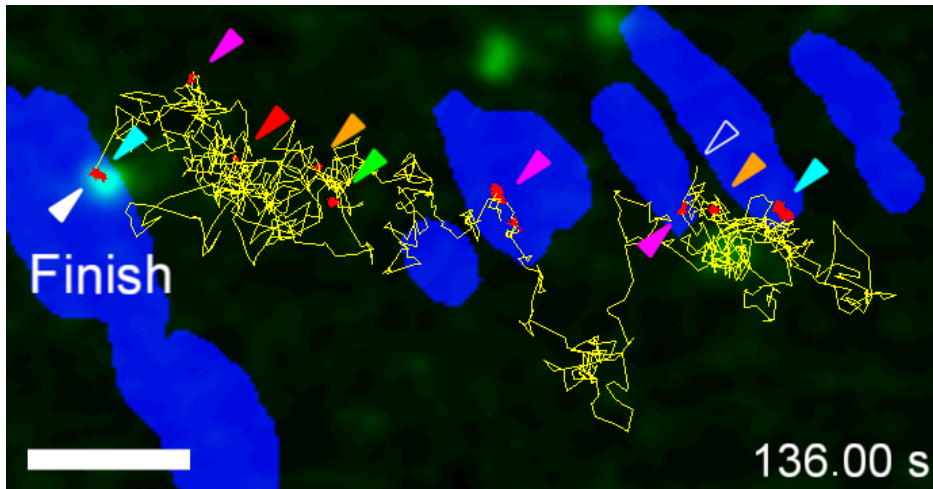
Supplementary Video Legends
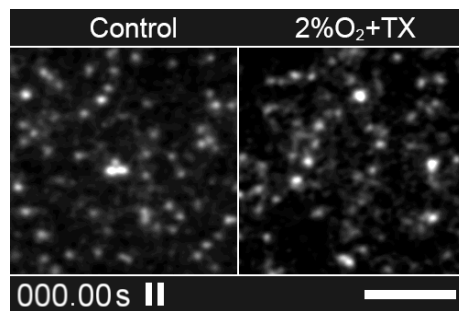
Supplementary Video 1 | Photobleaching of single TMR molecules attached to Halo-CD47 on the live-cell surface: control *vs*. 2%O_2+TX. Recorded at video rate (30 Hz) and replayed at 4x real time (the raw data for **Fig. 1a top**).
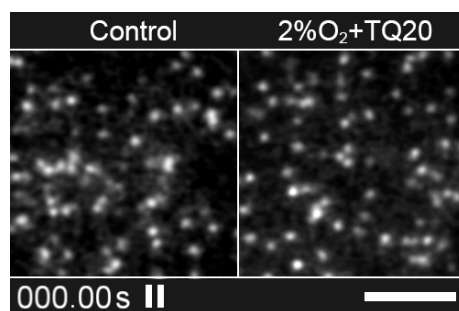

Supplementary Video 2 | Photobleaching of single ST647 molecules attached to ACP-CD47 on the live-cell surface: control *vs*. 2%O_2+TQ20. Recorded at video rate (30 Hz) and replayed at 4x real time (the raw data for **Fig. 1a bottom**).


Supplementary Video 3 | Photobleaching of single Cy5-TX molecules attached to Halo-CD47 on the live-cell surface under control, 2%O_2, and 0%O_2 conditions. Recorded at video rate (30 Hz) and replayed at 4x real time (the raw data for **Supplementary Fig. 18a bottom**).

Supplementary Video 4 | Single molecules of ST647-labeled ACP-integrin β1 (green spots) moved in and out of several FAs (blue binarized images of mGFP-paxillin), exhibiting alternating periods of TALL and thermal diffusion, both inside and outside the FAs (the raw data for **Fig. 4a left**), under 2%O_2+TQ20. A trajectory is overlaid for one of the ACP-integrin β1 molecules.
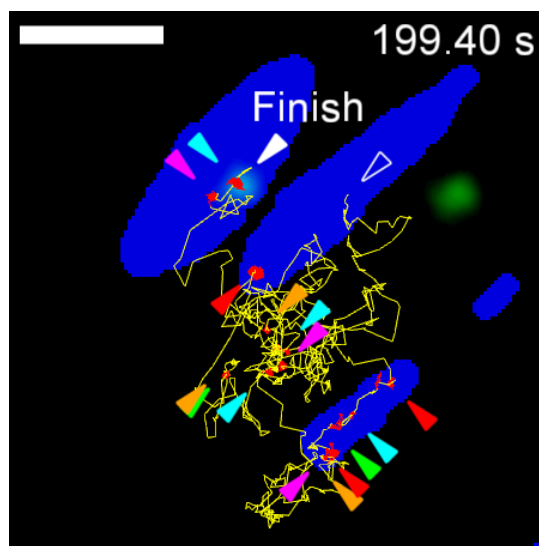
Supplementary Video 5 | Single molecules of ST647-labeled ACP-integrin β3, exhibiting intermittent TALLs similar to those of ACP-integrin β1 (the raw data for **Fig. 4a right**).
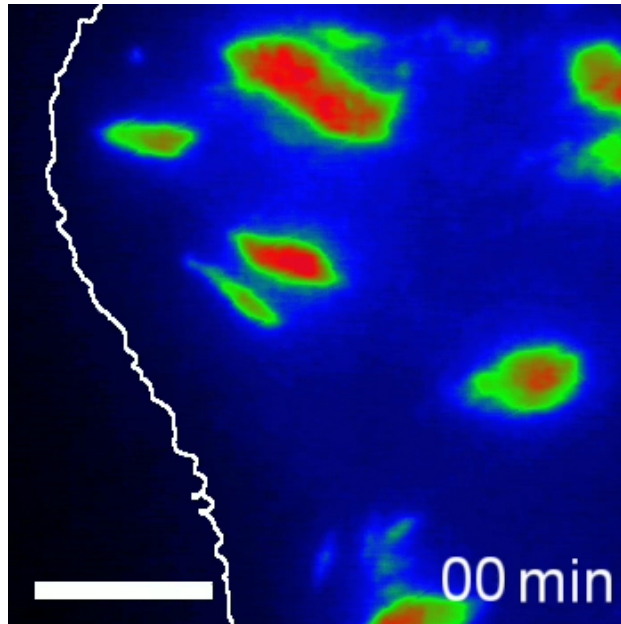
Supplementary Video 6 | Time-course of FA diminution (visualized by mGFP-paxillin with color coding) after the addition of 10 μM ROCK inhibitor Y26732 (see **Supplementary Fig. 32a** for the color scale).
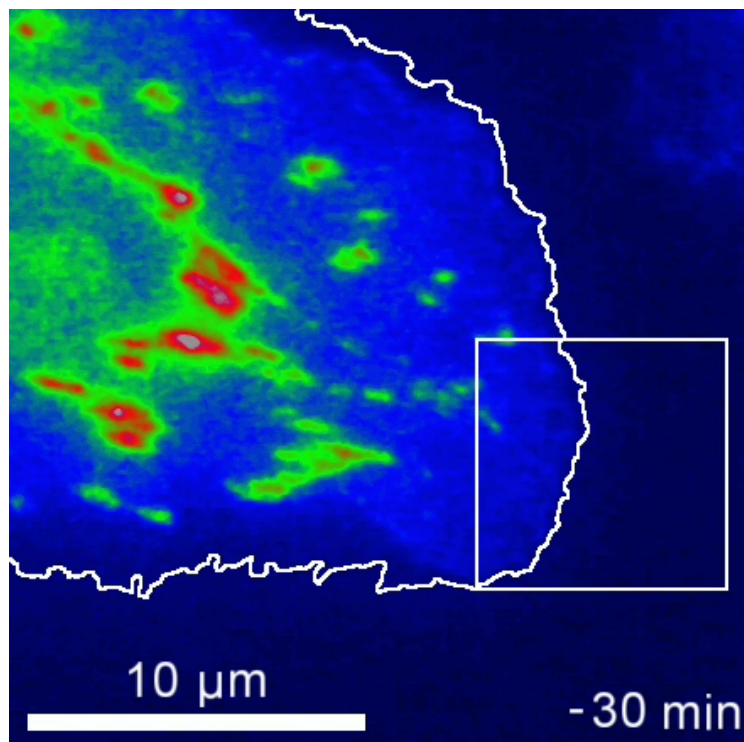
Supplementary Video 7 | Time-lapse observation of FA formation and its termination near the cell periphery. FAs were labeled by mGFP-paxillin, and its signal intensity is color-coded (see **Supplementary Fig. 33a** for the color scale).

Supplementary References

(Continued from Main Text and Methods)

54. Wehrle-Haller, B. Analysis of integrin dynamics by fluorescence recovery after photobleaching. *Methods Mol. Biol.* **370,** 173–202 (2007).

55. Goetz, J. G. *et al.* Concerted regulation of focal adhesion dynamics by galectin-3 and tyrosine-phosphorylated caveolin-1. *J. Cell Biol.* **180,** 1261–1275 (2008).

56. Chen, L., Vicente-Manzanares, M., Potvin-Trottier, L., Wiseman, P. W. & Horwitz, A. R. The integrin-ligand interaction regulates adhesion and migration through a molecular clutch. *PLoS ONE* **7,** e40202–e40202 (2011).

57. Chibisov, A. K. Triplet states of cyanine dyes and reactions of electron transfer with their participation. *J. Photochem.* **6,** 199–214 (1976).

58. Korobov, V. E. & Chibisov, A. K. Primary processes in the photochemistry of rhodamine dyes. *J. Photochem.* **9,** 411–424 (1978).

59. Wagner, P. J. & Hammond, G. S. Properties and reactions of organic molecules in their triplet states. *Adv. Photochem.* **5,** 21 (1968).

60. Zondervan, R., Kulzer, F., Orlinskii, S. B. & Orrit, M. Photoblinking of Rhodamine 6G in Poly(vinyl alcohol): Radical Dark State Formed through the Triplet. *J. Phys. Chem. A* **107,** 6770–6776 (2003).

61. Yeow, E. K. L., Melnikov, S. M., Bell, T. D. M., De Schryver, F. C. & Hofkens, J. Characterizing the Fluorescence Intermittency and Photobleaching Kinetics of Dye Molecules Immobilized on a Glass Surface. *J. Phys. Chem. A* **110,** 1726–1734 (2006).

62. Widengren, J., Chmyrov, A., Eggeling, C., Löfdahl, P.-Å. & Seidel, C. A. M. Strategies to Improve Photostabilities in Ultrasensitive Fluorescence Spectroscopy. *J. Phys. Chem. A* **111,** 429–440 (2007).

63. Mutch, S. A. *et al.* Deconvolving single-molecule intensity distributions for quantitative microscopy measurements. *Biophys. J.* **92,** 2926–2943 (2007).

64. Meckel, T., Semrau, S., Schaaf, M. J. M. & Schmidt, T. Robust assessment of protein complex formation in vivo via single-molecule intensity distributions of autofluorescent proteins. *J. Biomed. Opt.* **16,** 076016–076016–13 (2011).

65. Zhang, Y. *et al.* HaloTag protein-mediated site-specific conjugation of bioluminescent proteins to quantum dots. *Angew. Chem. Int. Ed.* **45,** 4936–4940 (2006).

66. Hu, K., Ji, L., Applegate, K. T., Danuser, G. & Waterman-Storer, C. M. Differential transmission of actin motion within focal adhesions. *Science* **315,** 111–115 (2007).

67. Yamashiro, S. & Watanabe, N. A new link between the retrograde actin flow and focal adhesions. *J. Biochem.* **156,** 239–248 (2014).

68. Hirata, H., Chiam, K.-H., Lim, C. T. & Sokabe, M. Actin flow and talin dynamics govern rigidity sensing in actin-integrin linkage through talin extension. *J R Soc Interface* **11,** (2014).

69. Liu, J. *et al.* Talin determines the nanoscale architecture of focal adhesions. *Proc. Natl. Acad. Sci. USA* **112,** E4864–E4873 (2015).

70. Rossier, O. & Giannone, G. The journey of integrins and partners in a complex interactions landscape studied by super-resolution microscopy and single protein tracking. *Exp. Cell Res.* **343,** 28–34 (2016).

71. Legant, W. R. *et al.* Multidimensional traction force microscopy reveals out-of-plane rotational moments about focal adhesions. *Proc. Natl. Acad. Sci. USA* **110,** 881–886 (2013).

72. Haralick, R. M. & Shapiro, L. G. *Computer and robot vision*. (Prentice Hall, New Jersey, USA, 1993).

73. Zaidel-Bar, R., Milo, R., Kam, Z. & Geiger, B. A paxillin tyrosine phosphorylation switch regulates the assembly and form of cell-matrix adhesions. *J. Cell Sci.* **120,** 137–148 (2007).

74. Wolfenson, H. *et al.* A role for the juxtamembrane cytoplasm in the molecular dynamics of focal adhesions. *PLoS ONE* **4,** e4304 (2009).

75. Case, L. B. *et al.* Molecular mechanism of vinculin activation and nanoscale spatial organization in focal adhesions. *Nat. Cell Biol.* **17,** 880–892 (2015).

76. Takagi, J., Petre, B. M., Walz, T. & Springer, T. A. Global conformational rearrangements in integrin extracellular domains in outside-in and inside-out signaling. *Cell* **110,** 599–511 (2002).

77. Lefort, C. T. *et al.* Outside-in signal transmission by conformational changes in integrin Mac-1. *J. Immunol.* **183,** 6460–6468 (2009).

78. Shattil, S. J., Kim, C. & Ginsberg, M. H. The final steps of integrin activation: the end game. *Nat. Rev. Mol. Cell Biol.* **11,** 288–300 (2010).

79. Nagae, M. *et al.* Crystal structure of α5β1 integrin ectodomain: atomic details of the fibronectin receptor. *J. Cell Biol.* **197,** 131–140 (2012).

80. Kinashi, T. Intracellular signalling controlling integrin activation in lymphocytes. *Nat. Rev. Immunol.* **5,** 546–559 (2005).

81. Campbell, I. D. & Humphries, M. J. Integrin Structure, Activation, and Interactions. *Cold Spring Harb. Perspect. Biol.* **3,** a004994–a004994 (2011).

82. Zhu, J., Zhu, J. & Springer, T. A. Complete integrin headpiece opening in eight steps. *J. Cell Biol.* **201,** 1053–1068 (2013).

Super-long single-molecule tracking reveals dynamic-anchorage-induced integrin function

Taka A. Tsunoyama, Yusuke Watanabe, Junri Goto, Kazuma Naito, Kenichi G.N. Suzuki, Takahiro K. Fujiwara and Akihiro Kusumi

— Supplementary Note 1 —

Theory for obtaining the correct distributions for the durations

of single-molecule events and the kinetic rate constants

in the presence of photobleaching and

under the conditions of limited recording durations

In experiments using single fluorescent-molecule imaging and tracking, we often encounter interesting single molecule events, such as temporary arrest of lateral diffusion (TALL). To clarify and simplify the idea, in this theory part, we deal with the case where all molecules repeatedly undergo temporary simple-Brownian diffusion and TALL in the PM of living cells.

When we encounter TALL events, we often hope to evaluate the TALL lifetime or the distributions of the TALL durations by single-molecule tracking. Since we can see the behaviors of each single molecule, this evaluation might appear to be simple. However, the TALL-duration distribution measurements are often hampered by two problems: the photobleaching lifetime of the probe dye molecules and the limited durations of the image sequence recordings (from the initiation of the observation until the end of the recording of the image of the same view field, T_{rec}). In this **Supplementary Note 1** section, we develop a theory for obtaining the correct duration distributions of TALL events, by correcting the direct experimental results for photobleaching lifetimes and T_{rec} durations.

Consider many single fluorescent molecules in the PM undergoing repeated TALL events; *i.e.*, the molecules of interest are either mobile (undergoing simple-Brownian diffusion) or immobile (undergoing TALL), and they go back and forth between the mobile and immobile states. A molecule in the mobile (immobile) state can either transit to the immobile (mobile) state or become photobleached, as shown in the scheme in **Supplementary Fig. 2**. To simplify the theory, we assume that the rate of every transition between any two states is described by a single kinetic rate constant (single exponential lifetime). This was shown to be correct for the photobleaching rates (k_B), for all of the fluorescent organic dye molecules examined in this study. Simply put, the aim of this theory is to obtain the rate constant for the transition from the immobile state to the mobile state, k_M, using single-molecule tracking. For this scheme to be adequate, we assume that the immobilizing domain is very small and all molecules in the immobilizing domain can face the PM bulk region within the image integration time (camera frame time). Under these conditions, we can also assume that a single rate constant for the transition from the mobile state to the immobile state (k_I) can be defined, which depends on the average time until the

molecules encounter the immobilizing small domains (and thus depends on the diffusion coefficient during the mobile period).

If no photobleaching of the fluorescent probes occurred and if the observation periods were much longer than the TALL durations, then the experimentally obtained TALL duration distribution would require no corrections. However, under the normal single-molecule observation conditions employed for live cells, photobleaching commonly occurs on the orders of 1-10 s, and the total duration of single-molecule observations on a single view field, T_{rec}, is quite limited, and normally less than a few 100 s.

First, we will explain how photobleaching affects the experimentally-observed distribution of individual TALL durations. The photobleaching of an ensemble of molecules quite often follows an exponential time course, as shown for all of the molecules employed in this study. Therefore, the photobleaching of each single molecule occurs stochastically, following the exponential time course. This means that in single-molecule tracking, the time window provided by each molecule will have a single exponential distribution, and thus when molecular events are observed by single-molecule tracking, it means that the events are observed through various time windows with single-exponential lifetime distributions. Therefore, to obtain the correct duration distribution of TALL events, this skewed lifetime distribution viewed through the looking glass of single molecules must be corrected.

Second, we will explain how the limited recording (observation) period, T_{rec}, influences the experimentally-observed distribution of individual TALL durations (**Supplementary Fig. 37**). This is because a large fraction of observed molecules might already be undergoing TALL at time 0, and those that start undergoing TALL during the observation period might still be undergoing TALL at the end of the observation period. Namely, the observed TALL events would include those with truncations at the beginning and ending portions of the TALL events, and this would prevent us from directly evaluating the TALL periods from the single-molecule tracking data.

In the following, we consider how these two effects can be taken into account for correctly obtaining the TALL duration distributions and the rate constants for the transition

from the immobile state to the mobile state, k_M. We also show that this evaluation is possible in the presence of an additional long-term immobilized component, with a lifetime much longer than T_{rec}.

Experimentally, we evaluate the TALL durations in the following way. First, we choose the field of view of the cell, using minimum irradiation to avoid photobleaching. Then, we start (time 0) recording a single-molecule movie, which often includes ~100 fluorescent spots. The observation lasts for a period called T_{rec}, which we simply call the "observation duration". In this definition, T_{rec} represents the time at which a single observation (a recording of consecutive images) ends.

Second, these recordings are repeated many times (M times), and each time, we select a different view field (in the same cell culture dish or in a different cell culture dish), but we assume that the recording (observation) duration T_{rec} is the same for all of the recording sets. The observed duration for each molecule could be much shorter due to photobleaching, but T_{rec} simply represents the period in which a series of consecutive images (a movie) on a single view field is recorded. Therefore, the total time spent to finish a series of experiments will be $M \times T_{rec}$.

Third, we track all of the observed fluorescent spots and obtain their trajectories (neglecting fluorescent spots observed for periods shorter than 21 frames, this value is represented as T_{min} [in the case of video-rate observations, this time is 0.70 s]) and extract all of the TALL events found in all of the trajectories. This minimal length of the trajectory (21 frames) is required to define a TALL event. Here, we define another parameter, T_{total}, as "the sum of the time lengths of all of the trajectories (in time)" in an entire set of experiments. Note that $M \times T_{rec}$ should not be confused with T_{total}, as the former simply represents the total time of observations spent for a set of experiments, whereas the latter represents the length of all single-molecule trajectories obtained in an entire set of experiments (in the unit of seconds).

Fourth, we measure the duration of every TALL event and obtain the experimental histogram of TALL durations, without correction for photobleaching and the limited T_{rec} effect.

In this theory, we describe a method for correcting this raw distribution skewed by the limited photobleaching lifetime and T_{rec}, and for obtaining k_M, following the scheme shown in **Supplementary Fig. 2**.

(1) The equilibrium between mobile molecules and molecules undergoing TALL

In the scheme shown in **Supplementary Fig. 2**, a molecule in the mobile (immobile) state can either transit to the immobile (mobile) state or become photobleached. The time-dependent changes of the numbers of molecules in the immobile and mobile states, $N_I(t)$ and $N_M(t)$, respectively, are described by using the rate constants for the transition to the mobile and immobile states and photobleaching, k_M (= $1/\tau$, where τ is the TALL lifetime), k_I, and k_B (= $1/\tau_B$, where τ_B is the photobleaching lifetime), respectively, as

$$\frac{\mathrm{d}N_I(t)}{\mathrm{d}t} = -(k_M + k_B)N_I(t) + k_I N_M(t) \tag{1}$$

$$\frac{\mathrm{d}N_M(t)}{\mathrm{d}t} = -(k_I + k_B)N_M(t) + k_M N_I(t) . \tag{2}$$

Note that, in the present report, the numbers of molecules are not natural numbers, but the real numbers. In each recording, the numbers of molecules were counted, but after repeating the experiments M times, the average number will become the real number.

In the present report, time 0 ($t = 0$) is set at the time when the observation was initiated. We describe the numbers of fluorescent molecules in the immobile and mobile states at time 0 as N_{I0} and N_{M0}, respectively, and the total number of fluorescent molecules as N_0 i.e.,

$$N_I(0) = N_{I0} \tag{3}$$

$$N_M(0) = N_{M0} \tag{4}$$

$$N_0 = N_{I0} + N_{M0} . \tag{5}$$

Eqs. 1 and 2 are solved and $N_I(t)$ and $N_M(t)$ are written as

$$N_I(t) = \frac{k_I N_{M0} + k_I N_{I0}}{k_I + k_M} \exp(-k_B t) - \frac{k_I N_{M0} - k_M N_{I0}}{k_I + k_M} \exp\left[-(k_I + k_M + k_B)\cdot t\right] \qquad (6)$$

$$N_M(t) = \frac{k_M N_{M0} + k_M N_{I0}}{k_I + k_M} \exp(-k_B t) + \frac{k_I N_{M0} - k_M N_{I0}}{k_I + k_M} \exp\left[-(k_I + k_M + k_B)\cdot t\right] . \qquad (7)$$

At $t = 0$, the numbers of molecules in the mobile and immobile states are considered to be in equilibrium, i.e.,

$$k_M N_{I0} = k_I N_{M0} . \qquad (8)$$

Combining Eqs. 5 and 8, N_{I0} and N_{M0} can be expressed as

$$N_{I0} = N_0 k_I / (k_I + k_M) \qquad (9)$$

$$N_{M0} = N_0 k_M / (k_I + k_M) . \qquad (10)$$

Using this relationship, Eqs. 6 and 7 can be written as

$$N_I(t) = \frac{k_I N_0}{k_I + k_M} \exp(-k_B t) \qquad (11)$$

$$N_M(t) = \frac{k_M N_0}{k_I + k_M} \exp(-k_B t) . \qquad (12)$$

Therefore, the following important relationship is obtained:

$$k_M N_I(t) = k_I N_M(t) . \qquad (13)$$

Namely, if the numbers of molecules in the mobile and immobile states are in equilibrium at $t = 0$, and if the photobleaching rates are the same for both mobile and immobile molecules (which will generally be true), then the numbers of molecules that are still fluorescent (non-photobleached) at (any) time t in the mobile and immobile states are also in equilibrium.

(2) New definitions of the end of a TALL event and the TALL lifetime

In this report, the end of a TALL event is defined as either when a molecule in the immobile state transits to the mobile state (when it resumes diffusion) or when it is photobleached. Note that in this definition, the end of TALL is determined by either the molecule's restarting of motion or photobleaching, whichever occurred first, and that therefore this definition is different from our previous definition. In our previous reports, the end of a TALL event was solely defined by the restarting of the molecule's motion, and when photobleaching occurred before diffusion resumed, we did not measure the immobile duration. The effect of not including such TALL events was corrected, by using the photobleaching lifetime. However, as shown later, this correction method is only correct when the photobleaching lifetime and the TALL lifetime are much shorter than the recording (observation) duration (T_{rec}). In the present research, because we succeeded in substantially prolonging the photobleaching lifetime, the recording duration T_{rec} might not be much longer than the photobleaching lifetime. Therefore, to obtain the correct distribution of TALL durations and thus to evaluate the rate constant for the transition from the immobile state to the mobile state, k_M, we had to explicitly include both the effects of the photobleaching kinetics (with the kinetic constant k_B) and the limited recording duration (T_{rec}) in the theory. For this purpose, experimentally, we should measure the durations of all TALL events, regardless of whether they ended by photobleaching or by the resumption of thermal diffusion. The final conclusion is that the previous treatment is correct when the photobleaching lifetime is substantially shorter than the recording duration ($1/k_B < T_{rec}/2.4$), and that even when $1/k_B \sim T_{rec}$, if the TALL lifetime is substantially (~3x) shorter than the photobleaching lifetime $1/k_B$, then the influence of the limited recording time (T_{rec}) is limited.

(3) The distribution of TALL durations (probability density function)
Using the new definition of the end of a TALL event, the probability density function of TALL duration [$P(\delta)$] is described using k_M and k_B (δ represents the TALL duration; $P(\delta)$ represents the probability density function without considering T_{rec} and T_{min}).

$$P(\delta) \propto \exp\left[-\left(k_{\mathrm{B}} + k_{\mathrm{M}}\right) \cdot \delta\right] . \tag{14}$$

The proportionality coefficient for this function is determined by normalization (because it is a probability density function)

$$P(\delta) = \left(k_{\mathrm{B}} + k_{\mathrm{M}}\right)\exp\left[-\left(k_{\mathrm{B}} + k_{\mathrm{M}}\right) \cdot \delta\right] . \tag{15}$$

Since the observation duration in which single-molecule imaging-tracking is conducted is limited (T_{rec} is not infinitely long), we consider the number of molecules that start TALL events (become immobile) at time t, $F_{\mathrm{S}}(t)$. $F_{\mathrm{S}}(t)$ is described by k_{I} and $N_{\mathrm{M}}(t)$ as

$$F_{\mathrm{S}}(t) = k_{\mathrm{I}} N_{\mathrm{M}}(t) . \tag{16}$$

Using Eq. 12, Eq. 16 is expressed as

$$F_{\mathrm{S}}(t) = \frac{k_{\mathrm{I}} k_{\mathrm{M}} N_0}{k_{\mathrm{I}} + k_{\mathrm{M}}} \exp\left(-k_{\mathrm{B}}t\right) . \tag{17}$$

The TALL events that occur during the observation duration between $t = 0$ and T_{rec} are classified into three cases, because TALLs might (a) be totally included within the observation period, but they also might (b) start after time 0 (at $t > 0$) and continue after the observation period, and (c) start at $t \leq 0$ before the observation period (see **Supplementary Fig. 37**). For simplicity, we neglect the TALLs that started before the observation and did not end during the observation period. If this frequently occurs, then the observation duration should be extended, perhaps by using time-lapse observations.

(Case a) For TALLs that were totally included within the observation period ($0 < t \leq T_{\mathrm{rec}}$); the probability density function $G_{\mathrm{a}}(\delta)$

Here we consider the duration (δ) distribution of TALLs (probability density function of δ) that started after $t = 0$ and ended before $t = T_{\mathrm{rec}}$ (defined as $G_{\mathrm{a}}(\delta)$; see "Case a" in **Supplementary Fig. 37**). When T_{rec} is very long, the number of TALL events that last for a duration δ can be expressed as

$$G(\delta) = \int_0^\infty F_{\mathrm{S}}(t) \cdot \mathrm{d}t \cdot P(\delta) . \tag{18}$$

Note that G is expressed as the number of TALLs/time, providing the distribution as a function of time δ (the height of each bar [the y-axis] in the histogram provides the number of occurrences per the bin size (in time), and so the dimensions of Eq. 18 are correct. This will apply to all of the histograms shown here). In the analysis of the experimental results, we usually obtain a histogram of the duration (δ), which we generally define as $H(\delta)$. $H(\delta)$ is simply a function obtained by multiplying the histogram's bin size Δt with $G(\delta)$.

Here we consider the case where T_{rec} is limited, and the molecules are mobile at $t = T_{\text{rec}}$. In this case, the upper end of the integration must be limited to $T_{\text{rec}} - \delta$; *i.e.*,

$$G_{\text{a}}(\delta) = \int_0^{T_{\text{rec}} - \delta} F_{\text{S}}(t) \cdot \mathrm{d}t \cdot P(\delta) . \tag{19}$$

Using Eqs. 15 and 17, followed by integration, G_{a} is expressed as

$$\begin{aligned} G_{\text{a}}(\delta) &= \frac{k_{\text{I}} k_{\text{M}} (k_{\text{B}} + k_{\text{M}}) N_0}{k_{\text{B}} (k_{\text{I}} + k_{\text{M}})} \exp\left[-(k_{\text{B}} + k_{\text{M}}) \cdot \delta\right] \\ &\quad - \frac{k_{\text{I}} k_{\text{M}} (k_{\text{B}} + k_{\text{M}}) N_0}{k_{\text{B}} (k_{\text{I}} + k_{\text{M}})} \exp(-k_{\text{B}} T_{\text{rec}}) \exp(-k_{\text{M}} \delta) . \end{aligned} \tag{20}$$

(Case b) For TALLs that started after time 0 (at $t > 0$) and continued after the observation period; the probability density function $G_{\text{b}}(\delta)$

Here, we consider the TALLs that initiated after $t = T_{\text{rec}} - \delta$ and did not end by $t = T_{\text{rec}}$ (*i.e.*, the TALL duration must be longer than δ; see "Case b" in **Supplementary Fig. 37**). The duration (δ) distribution of the TALLs for this case (probability density function of δ), defined as $G_{\text{b}}(\delta)$, can be calculated as

$$G_{\text{b}}(\delta) = F_{\text{S}}(T_{\text{rec}} - \delta) \cdot \int_\delta^\infty P(\tau) \cdot \mathrm{d}\tau . \tag{21}$$

Using Eqs. 15 and 17, followed by integration, $G_{\text{b}}(\delta)$ is expressed as

$$G_{\text{b}}(\delta) = \frac{k_{\text{I}} k_{\text{M}} N_0}{k_{\text{I}} + k_{\text{M}}} \exp(-k_{\text{B}} T_{\text{rec}}) \exp(-k_{\text{M}} \delta) . \tag{22}$$

(Case c) For TALLs that started at $t \leq 0$; the probability density functions G_c and $G_{AATI}(\delta)$

See "Case c" in **Supplementary Fig. 37**. First, we derive the duration (δ) distribution of TALLs (probability density function $G_c(\delta)$) in the case where a fluorescent molecule is immobile at $t = 0$ and becomes mobile at time δ (one of the cases of Case c). For this purpose, we consider the number of fluorescent molecules that are immobile at $t = 0$ and are still immobile at time t, and call it $N_I^0(t)$. The time-dependent changes of $N_I^0(t)$ are expressed as

$$\frac{dN_I^0(t)}{dt} = -(k_B + k_M)N_I^0(t) .$$
(23)

With the initial value N_{I0} (Eq. 3), the solution of Eq. 23 can be expressed as

$$N_I^0(t) = N_{I0} \exp\left[-(k_B + k_M)\cdot t\right] .$$
(24)

$$N_I^0(t) = \frac{k_I N_0}{k_I + k_M} \exp\left[-(k_B + k_M)\cdot t\right] .$$
(25)

$G_c(\delta)$ can be written as

$$G_c(\delta) = k_M N_I^0(\delta) .$$
(26)

Using Eq. 25, $G_c(\delta)$ can be expressed as

$$G_c(\delta) = \frac{k_M k_I N_0}{k_I + k_M} \exp\left[-(k_B + k_M)\cdot \delta\right] .$$
(27)

Second, we derive the duration (δ) distribution of TALLs (probability density function) in the case where a fluorescent molecule is immobile at $t = 0$ and becomes photobleached at time δ ($G_{AATI}(\delta)$; the other case of Case c; AATI represents Apparent All-Time Immobile). However, since some molecules might be totally immobilized during periods much longer than T_{rec}, which would represent alternative cases outside the scope of the TALL events considered here (see "Alternative case" in **Supplementary Fig. 37**), we will consider this in a later subsection "**(4) Estimating the time fraction of**

apparently-all-time-immobile molecules and dealing with molecules immobile for periods much longer than T_{rec}".

(The full equation) The function to describe the TALL duration distribution; $G_{TALL}(\delta)$

Taking the results for cases a, b, and c together, the duration (δ) distribution of all observed TALL events $G_{TALL}(\delta)$ is given by

$$G_{TALL}(\delta) = G_a(\delta) + G_b(\delta) + G_c(\delta) \tag{28}$$

$$\begin{aligned} G_{TALL}(\delta) = &\frac{k_I k_M (2k_B + k_M) N_0}{k_B (k_I + k_M)} \exp[-(k_B + k_M) \cdot \delta] \\ &- \frac{k_I k_M{}^2 N_0}{k_B (k_I + k_M)} \exp(-k_B T_{rec}) \exp(-k_M \delta) \ . \end{aligned} \tag{29}$$

Namely, the distribution is given by the sum of two exponential functions, with rate constants of k_M and $k_B + k_M$. As stated (right after Eq. 18), in the analysis of the experimental results, we generally obtain a histogram of the durations (δ), which we define as $H_{TALL}(\delta)$. $H_{TALL}(\delta)$ can be obtained by multiplying the histogram's bin size Δt with $G_{TALL}(\delta)$ (because $G_{TALL}(\delta)$ is a distribution function with the dimensions of count/time).

$$\begin{aligned} H_{TALL}(\delta) = &\frac{k_I k_M (2k_B + k_M) N_0 \cdot \Delta t}{k_B (k_I + k_M)} \exp[-(k_B + k_M) \cdot \delta] \\ &- \frac{k_I k_M{}^2 N_0 \cdot \Delta t}{k_B (k_I + k_M)} \exp(-k_B T_{rec}) \exp(-k_M \delta) \ . \end{aligned} \tag{30}$$

Since k_B can be determined independently, and T_{rec} is an experimental parameter that the operator can determine, k_M can be determined by fitting the experimentally-obtained $H_{TALL}(\delta)$ by the sum of two exponential functions. The determination precision depends on the ratio of k_B *vs.* k_M, which will be further discussed in a later subsection "**(6) An approximate expression of the TALL duration distribution function under the experimental conditions employed here; $G_{fit}(\delta)$**"

These results indicate that k_M can be determined by observing either one of the cases

of a, b, or c. For example, one could only observe molecules that are immobile at $t = 0$, and by simply measuring the times at which they become mobile, one could evaluate k_M using Eq. 27 (the bin size Δt should be multiplied for its histogram, as stated before for any probability density functions). This approach would be convenient if one could repeat many such experiments easily. Meanwhile, if repeating many experiments is difficult or too time consuming (for example, when repeatedly preparing specimens is difficult), one could observe all of the cases a, b, and c for the same viewfield (this way, the number of molecules observed for a single recording can be increased), and obtain k_M using Eq. 30.

When T_{rec} is infinitely long, Eq. 29 becomes

$$G_{\mathrm{TALL}}(\delta, T_{\mathrm{rec}} \to \infty) = \frac{k_I k_M (2k_B + k_M) N_0}{k_B (k_I + k_M)} \exp[-(k_B + k_M) \cdot \delta] \,, \tag{31}$$

which is consistent with the equation previously used to correct for photobleaching[83],

$$k_M = k_{\mathrm{Observed}} - k_B \,, \tag{32}$$

or

$$1/\tau_M = 1/\tau_{\mathrm{Observed}} - 1/\tau_B \,, \tag{33}$$

where k_{Observed} is a value determined by single-exponential fitting using Eq. 31, and τ_x is the inverse of k_x.

In the unlikely case of $k_B = 0$ (when no photobleaching occurs), Eqs. 15 and 17 become

$$P(\delta) = k_M \exp[-k_M \cdot \delta] \,. \tag{34}$$

$$F_S(t) = \frac{k_I k_M N_0}{k_I + k_M} \,. \tag{35}$$

respectively. Applying these equations to evaluate Eqs. 19 and 21, and directly using $k_B = 0$ in Eq. 27, the following equations are obtained

$$G_a(\delta) = (T_{\mathrm{rec}} - \delta) \frac{k_I k_M N_0}{(k_I + k_M)} \exp[-k_M \delta] \,, \tag{36}$$

$$G_{\mathrm{b}}(\delta) = \frac{k_{\mathrm{M}} k_{\mathrm{I}} N_0}{k_{\mathrm{I}} + k_{\mathrm{M}}} \exp[-k_{\mathrm{M}} \delta] \,, \qquad (37)$$

$$G_{\mathrm{c}}(\delta) = \frac{k_{\mathrm{M}} k_{\mathrm{I}} N_0}{k_{\mathrm{I}} + k_{\mathrm{M}}} \exp[-k_{\mathrm{M}} \delta] \,. \qquad (38)$$

respectively.

(4) Estimating the time fraction of apparently-all-time-immobile molecules and dealing with molecules immobile for periods much longer than T_{rec}

In the scheme shown in **Supplementary Fig. 37**, consider the case in which there are molecules that are immobile and coexist for periods much longer than T_{rec}, and therefore cannot be considered to undergo TALL ($k_{\mathrm{M}} \sim 0$), which we call an "Alternative case", as shown in **Supplementary Fig. 37**. When such molecules coexist in the viewfield of the microscope, it is difficult to differentiate these "alternative" molecules from those that undergo intermittent TALL events and are immobile at t = 0 (Case c), and then become photobleached before restarting their motion (see the bottom case of Case c in the scheme shown in **Supplementary Fig. 37**), which we call "apparently-all-time-immobile (AATI) molecules".

Previously, such AATI molecules were simply called "all-time-immobile molecules" (for example, see **Refs. 53 and 83**). However, they are often a subfraction of the molecules that exhibit alternating mobile and immobile periods, and were incidentally and temporarily immobilized at time 0, and not molecules that are immobile for periods much longer than T_{rec}.

Here, we developed a method to evaluate the time fraction in which the molecules are expected to exhibit the AATI behavior (f_{AATI}) from the parameters determined by $G_{\mathrm{TALL}}(\delta)$ (or $G_{\mathrm{a}}(\delta)$, $G_{\mathrm{b}}(\delta)$, or $G_{\mathrm{c}}(\delta)$) (namely, assuming the absence of alternative molecules undergoing immobilization for periods much longer than T_{rec}). Once f_{AATI} is determined, we can experimentally determine the fraction of alternative molecules (which are immobile for

periods much longer than T_{rec}; f_{MLI}, MLI represents "Much Longer Immobilization"), using the equation,

$$f_{\text{MLI}} = f_{\text{ExpATI}} - f_{\text{AATI}} \quad , \tag{39}$$

where f_{ExpATI} represents the fraction of molecules that were experimentally and directly determined to be immobile at time 0 and photobleached before starting motion.

The number of TALL events that end at time δ (duration δ, because the molecule is already immobile at time 0) due to photobleaching (the second case of Case c, G_{AATI}) can be expressed as

$$G_{\text{AATI}}(\delta) = k_{\text{B}} N_{\text{I}}^{\ 0}(\delta) \ . \tag{40}$$

By using the expression for $N_{\text{I}}^0(\delta)$ given in Eq. 25, Eq. 40 can be rewritten as

$$G_{\text{AATI}}(\delta) = \frac{k_{\text{B}} k_{\text{I}} N_0}{k_{\text{I}} + k_{\text{M}}} \exp[-(k_{\text{B}} + k_{\text{M}}) \cdot \delta] \ . \tag{41}$$

The histogram for the duration (δ) of AATI molecules, $H_{\text{AATI}}(\delta)$, can be obtained by multiplying the histogram's bin size Δt with $G_{\text{AATI}}(\delta)$, as we did to obtain Eq. 30. Namely,

$$H_{\text{AATI}}(\delta) = \frac{k_{\text{B}} k_{\text{I}} N_0 \cdot \Delta t}{k_{\text{I}} + k_{\text{M}}} \exp[-(k_{\text{B}} + k_{\text{M}}) \cdot \delta] \ . \tag{42}$$

The time fraction f_{AATI} can be obtained by the following equation,

$$f_{\text{AATI}} = 1 / T_{\text{total}} \cdot \int_{T_{\text{min}}}^{T_{\text{rec}}} \delta \cdot H_{\text{AATI}}(\delta) \cdot \mathrm{d}\delta \ . \tag{43}$$

After integration, the following equation is obtained:

$$f_{\text{AATI}} = \frac{k_{\text{B}} k_{\text{I}} N_0 \cdot \Delta t}{T_{\text{total}}(k_{\text{I}} + k_{\text{M}})} \left[\begin{array}{l} -\dfrac{1}{(k_{\text{B}} + k_{\text{M}})^2} \exp[-(k_{\text{B}} + k_{\text{M}}) \cdot \delta] \\[4mm] -\dfrac{1}{k_{\text{B}} + k_{\text{M}}} \cdot \delta \cdot \exp[-(k_{\text{B}} + k_{\text{M}}) \cdot \delta] \end{array} \right]_{T_{\text{min}}}^{T_{\text{rec}}} . \tag{44}$$

As such, f_{AATI} can be obtained from experimentally determined parameters, and then by using Eq. 30, f_{MLI} can be determined. In other words, if f_{ExpATI} is close to f_{AATI}, then it indicates that the molecules undergoing immobilization for periods that are much longer than T_{rec} will not exist, as discussed in the subsection "Each TALL event of integrins ....." in

-13-

the main text.

(5) Testing the function $G_{TALL}(\delta)$ using Monte Carlo simulations of particles undergoing repeated intermittent TALL events

In the experiments conducted in the present research, under the conditions optimized for the lowest photobleaching rate (ST647, 2%O_2+TQ20), k_B was ~1/83.5 s^{-1}, and our standard observation duration of integrin molecules (T_{rec}) was 200 s. We performed Monte Carlo simulations with transitions to mobile, immobile, or photobleaching states with probabilities given by their rate constants (T_{rec} = 200 s or 70 s: k_B = 1/83.5 s^{-1} or 1/4.3 s^{-1}; k_M = 1/0.5, 1/5, 1/50, 1/70, 1/167 or 1/500 s^{-1}; and k_I = 1/1, respectively; since k_I does not affect the exponential lifetimes, it is assumed to be 1), and obtained the TALL duration distributions. The simulation was conducted until TALL occurred 10^8 times (**Supplementary Figs. 38 and 39, left-top**).

These distributions were fitted by using $G_{TALL}(\delta)$ (Eq. 29, red solid line). The fits were excellent over the full ranges of δ (up to 200 s = T_{rec}) and the % frequency (y axis, in 4 x log$_{10}$ cycles), suggesting that the $G_{TALL}(\delta)$ obtained here is correct. Next, we simulated the case where T_{rec} was changed from 200 s to 70 s, which was close to 1/k_B (with the same k_B = 1/83.5 s^{-1}; using the same six k_M values) (**Supplementary Fig. 39, left-bottom**). The fits using $G_{TALL}(\delta)$ were excellent. As the next step, we simulated the case where the photobleaching rate was ~20x larger (k_B = 1/4.3 s^{-1}) and T_{rec} was either 70 s or 200 s. Even under these conditions, the fits using $G_{TALL}(\delta)$ were excellent (**Supplementary Fig. 39, right boxes**), further supporting the proposal that $G_{TALL}(\delta)$ is the correct distribution function. Taken together, these results indicate that $G_{TALL}(\delta)$ in Eq. 29 represents the correct function for the TALL duration distribution.

(6) An approximate expression of the TALL duration distribution function (approximate probability density function of δ) under the experimental conditions employed here; $G_{fit}(\delta)$

Under actual experimental conditions, the attainable signal-to-noise ratios and the number of experiments that can be performed might be quite limited. Therefore, precisely fitting the TALL duration distribution histogram using $G_{TALL}(\delta)$ (or $H_{TALL}(\delta)$), as given in Eq. 29, might often be impractical, and thus one might want to fit the histogram using only the first term of $G_{TALL}(\delta)$, $G_{fit}(\delta)$. Namely,

$$G_{fit}(\delta) = \frac{k_I k_M (2k_B + k_M) N_0}{k_B (k_I + k_M)} \exp\left[-(k_B + k_M) \cdot \delta\right] \ , \tag{45}$$

which is the same as Eq. 30, meaning that it would be more practical to employ a long T_{rec} so that the second term in Eq. 30 could be neglected. In this subsection, we examine the cases where the corrections for T_{rec} could be neglected (*i.e.*, where $G_{fit}(\delta)$ could safely replace $G_{TALL}(\delta)$). For this purpose, we employed the somewhat standard experimental conditions of T_{rec} = 200 s and k_B = 1/83.5 s^{-1}, as described in the previous subsection (5).

As the first test, we examined the goodness of the fit when $G_{fit}(\delta)$ was used to replace $G_{TALL}(\delta)$ to fit the histograms shown in **Supplementary Figs. 38 and 39.** The best-fit curves obtained for $G_{TALL}(\delta)$ and $G_{fit}(\delta)$ are shown in these figures.

Under our standard conditions of T_{rec} = 200 s and k_B = 1/83.5 s^{-1} (**Supplementary Figs. 38 and 39, top left**), the fit appeared to be quite good, particularly in the δ interval between 0 and ~83.5 s for all of the k_M values employed here, consistent with the concept in which the durations of the events shorter than the photobleaching time could be measured with good precision. The largest deviation appeared to occur for $k_M \sim 1/70$; *i.e.*, when the k_B and k_M values were close to each other (**Supplementary Fig. 39, bottom left**), showing that under these conditions, $G_{TALL}(\delta)$, rather than $G_{fit}(\delta)$, should be employed.

To quantify the goodness of fit for various k_M values (which are the parameters we hope to obtain in these experiments), the deviation (χ^2) was plotted against $1/k_M$ for various values of T_{rec} (200 s, which was our standard value, and 70 s) and k_B (1/83.5 s^{-1}, which was our standard value, and 1/4.3 s^{-1}) (**Supplementary Fig. 40**). Under our standard observation conditions of k_B = 1/83.5 s^{-1} and T_{rec} = 200 s, the difference between the results using these two fit functions became the largest when $k_M \sim 1/70$ s^{-1}; *i.e.*, when k_M became

close to k_B. Compare this result with the $G_{TALL}(\delta)$ functions given in **Supplementary Fig. 38**. For $k_M << 1/70$ s^{-1}, the decay lifetime in the second term was quite different from that in the first term, but the pre-exponential coefficient was small. For $k_M >> 1/70$ s^{-1}, the pre-exponential coefficient of the second term was large, but the decay lifetime in the second term became quite similar to that of the first term, and the pre-exponential coefficient was small. When $k_M \sim 1/70$ s^{-1} (*i.e.*, when $k_M \sim k_B$), such compensations were inoperative.

For the cases where the photobleaching rate was ~20x larger ($k_B = 1/4.3$ s^{-1}) and T_{rec} was either 70 s or 200 s, the fits using $G_{fit}(\delta)$ were excellent for virtually all of the k_M values employed here (**Supplementary Figs. 39, right boxes and 40**). Taken together, these results indicate that when T_{rec} is greater than $1/k_B$ by a factor of 2.4 (200/83.5) or more, $G_{fit}(\delta)$, rather than $G_{TALL}(\delta)$, could be used.

However, note that we have discussed only the systematic differences between $G_{TALL}(\delta)$ and $G_{fit}(\delta)$ under the conditions where the durations of 10^8 TALLs were determined. In practical experimental situations, where generally the durations of only a few hundred TALLs could be determined, the experimental errors in evaluating k_M values are expected to be much greater, as compared with the value evaluated after observing 10^8 TALLs (which must be close to the correct k_M value). Particularly, correctly determining the k_M value smaller than the k_B value (TALL durations longer than the photobleaching lifetime), using the approximate function $G_{fit}(\delta)$, could be extremely difficult. That is, in these situations, one might wonder how close the k_M value estimated by an approximate function $G_{fit}(\delta)$ would come to those obtained using the correct function $G_{TALL}(\delta)$. In unfavorable conditions for determining the k_M value, the error will become much larger, even when the correct function $G_{TALL}(\delta)$ is used for the fitting. However, if one employs $G_{fit}(\delta)$, rather than $G_{TALL}(\delta)$, will the deviation from the correct k_M value be greater than that when $G_{TALL}(\delta)$ is used?

To address this question, and also as the second test for replacing $G_{TALL}(\delta)$ with $G_{fit}(\delta)$, we examined the difference in the estimation of k_M, between the cases where $G_{TALL}(\delta)$ and $G_{fit}(\delta)$ were used as fitting functions, under the conditions where the Monte Carlo

simulations were conducted until 500 TALLs were observed (as compared to 10^8 TALLs for previous figures) for each parameter set of k_M, k_B, and T_{rec}, to simulate the experimental conditions. Then, the fitting using $G_{TALL}(\delta)$ and $G_{fit}(\delta)$ to evaluate k_M was performed. This process was repeated 1,000 times, to obtain the mean ± SEM of k_Ms using these two functions.

The $1/k_M$ values obtained by the correct function $G_{TALL}(\delta)$ were plotted against those determined by using the approximate function $G_{fit}(\delta)$ (**Supplementary Figs. 41-44**). Interestingly and quite impressively, for virtually all combinations of the k_M, k_B, and T_{rec} values, both the mean and SEM values obtained by fitting with $G_{TALL}(\delta)$ and $G_{fit}(\delta)$ were similar to each other. Even when the obtained mean values were quite different from the correct $1/k_M$ value and/or when the SEMs were very large, their values obtained by using $G_{TALL}(\delta)$ and $G_{fit}(\delta)$ were quite similar to each other (except for the very unusual case shown in the bottom right box in **Supplementary Fig. 42**). These results support the proposal that $G_{fit}(\delta)$ can replace $G_{TALL}(\delta)$ well, virtually under all of the conditions examined here. Therefore, $G_{fit}(\delta)$ was employed to evaluate k_M for integrins in the present research. Furthermore, these results support the intuitive expectation that for measuring k_M correctly, the relationship of $1/k_M < 1/k_B < T_{rec}$ must be satisfied. When this condition is satisfied, the $1/k_M$ values determined by $G_{TALL}(\delta)$ and $G_{fit}(\delta)$ coincided within a 5% difference (**Supplementary Figs. 41- 44**).

(7) Practical ways of applying the theory to obtain k_M and the time fraction in which molecules exhibit the AATI behavior, f_{AATI}

In the ideal cases discussed within the previous subsections, N_0 is known. However, in experiments, due to the presence of f_{MLI} (alternative case), N_0 is unknown. Meanwhile, k_B can be determined independently, using the same set of trajectories. Under these conditions, k_M, the parameter we hope to determine most, can be determined in the following manner.

If we define C as

$$C = \frac{k_{\mathrm{I}} k_{\mathrm{M}} N_0}{k_{\mathrm{B}}\left(k_{\mathrm{I}} + k_{\mathrm{M}}\right)} \quad , \tag{46}$$

then Eq. 30 and Eq. 42 can be rewritten as

$$
\begin{aligned}
H_{\mathrm{TALL}}(\delta) &= C\Delta t\left(2k_{\mathrm{B}} + k_{\mathrm{M}}\right)\exp\left[-\left(k_{\mathrm{B}} + k_{\mathrm{M}}\right)\cdot\delta\right] \\
&\quad - C\Delta t \cdot k_{\mathrm{M}}\exp\left(-k_{\mathrm{B}} T_{\mathrm{rec}}\right)\exp\left(-k_{\mathrm{M}}\delta\right) \; .
\end{aligned}
\tag{47}
$$

$$H_{\mathrm{AATI}}(\delta) = C\Delta t \frac{k_{\mathrm{B}}^{\,2}}{k_{\mathrm{M}}}\exp\left[-\left(k_{\mathrm{B}} + k_{\mathrm{M}}\right)\cdot\delta\right] \; . \tag{48}$$

By fitting the histogram (distribution) using Eq. 47 or Eq. 48 (using C and k_{M} as free parameters), C and k_{M} can be determined. The time fraction in which molecules exhibit the AATI behavior, f_{AATI} (Eq. 44), can now be calculated using all of the determined values as

$$f_{\mathrm{AATI}} = \frac{C\Delta t \cdot k_{\mathrm{B}}^{\,2}}{T_{\mathrm{total}} k_{\mathrm{M}}} \cdot \left[\begin{array}{c} -\dfrac{1}{\left(k_{\mathrm{B}} + k_{\mathrm{M}}\right)^2}\exp\left[-\left(k_{\mathrm{B}} + k_{\mathrm{M}}\right)\cdot\delta\right] \\[2ex] -\dfrac{1}{\left(k_{\mathrm{B}} + k_{\mathrm{M}}\right)}\cdot\delta\cdot\exp\left[-\left(k_{\mathrm{B}} + k_{\mathrm{M}}\right)\cdot\delta\right] \end{array}\right]_{T_{\mathrm{min}}}^{T_{\mathrm{rec}}} \; . \tag{49}$$

Supplementary Note 1 Figures
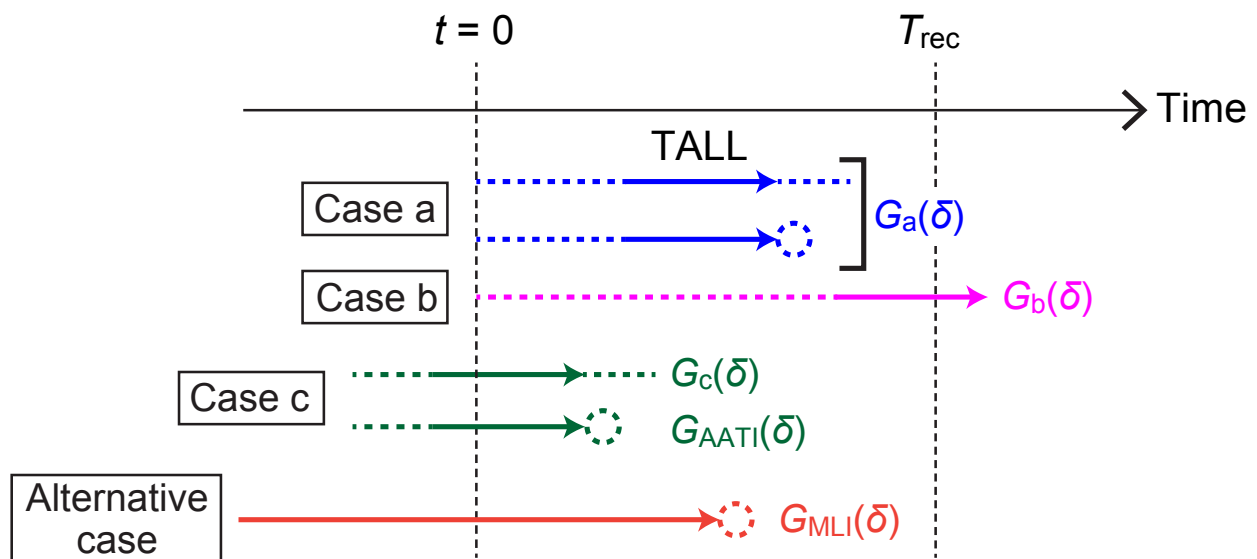
Supplementary Figure 37 | Timing diagram of TALL events (arrows) relative to the recording (observation) period, starting from $t = 0$ and ending at $t = T_{rec}$. Arrows indicate the TALL periods. TALLs can end by either restarting diffusion or photobleaching (dashed circles).

TALLs are classified into three categories, in terms of the temporal relationship with the beginning and the end of each recording of a single viewfield ($t = 0$ and T_{rec}, respectively). TALLs might be totally included within the recording period ($0 < t \leq T_{rec}$, Case a; $G_a(\delta)$), might start after time 0 (at $t > 0$) and continue after the recording period (Case b; $G_b(\delta)$), and might start at $t \leq 0$ (Case c; $G_c(\delta)$). The TALLs of Case c that ended by photobleaching have often been called "all-time immobile" events, as the molecules showing this behavior are immobilized throughout the recording period, because they are immobile at $t = 0$ and photobleached before restarting diffusion.

There might be some molecules in the viewfield that exhibit "much longer immobilization (MLI)", as compared with T_{rec} (and thus with the TALL periods exhibited by the large majority of observed molecules), called "alternative molecules" (Alternative case). These molecules will be considered separately.
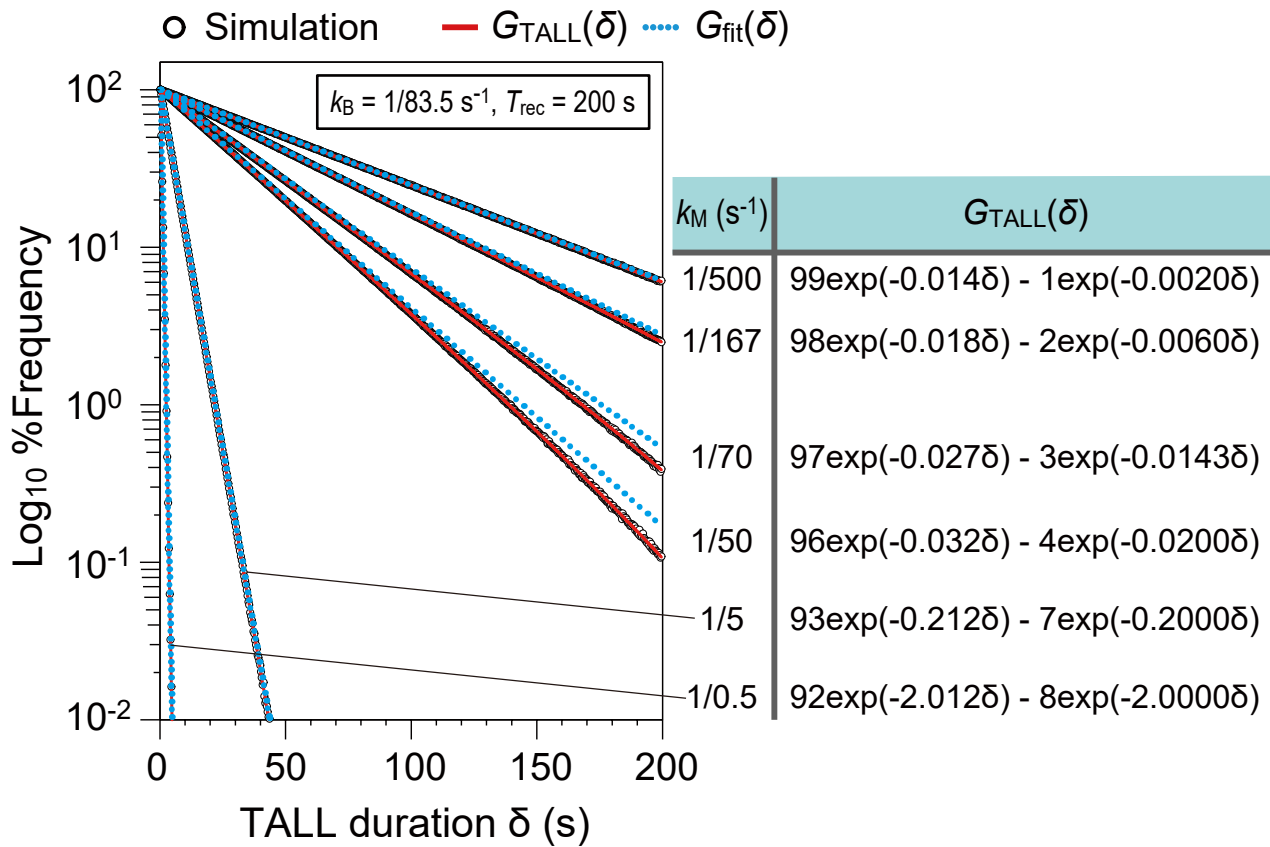
Supplementary Figure 38 | The distributions of TALL durations when k_B = 1/83.5 and T_{rec} = 200 s, obtained by Monte Carlo simulations of Brownian particles undergoing repeated TALL events and the best fit functions for the distributions using $G_{TALL}(\delta)$ (red curves) and $G_{fit}(\delta)$ (blue curves). The actual functions of $G_{TALL}(\delta)$ are provided for each k_M value, and their first terms represent $G_{fit}(\delta)$. The k_M values employed here were 1/0.5, 1/5, 1/50, 1/70, 1/167 and 1/500 s^{-1}.
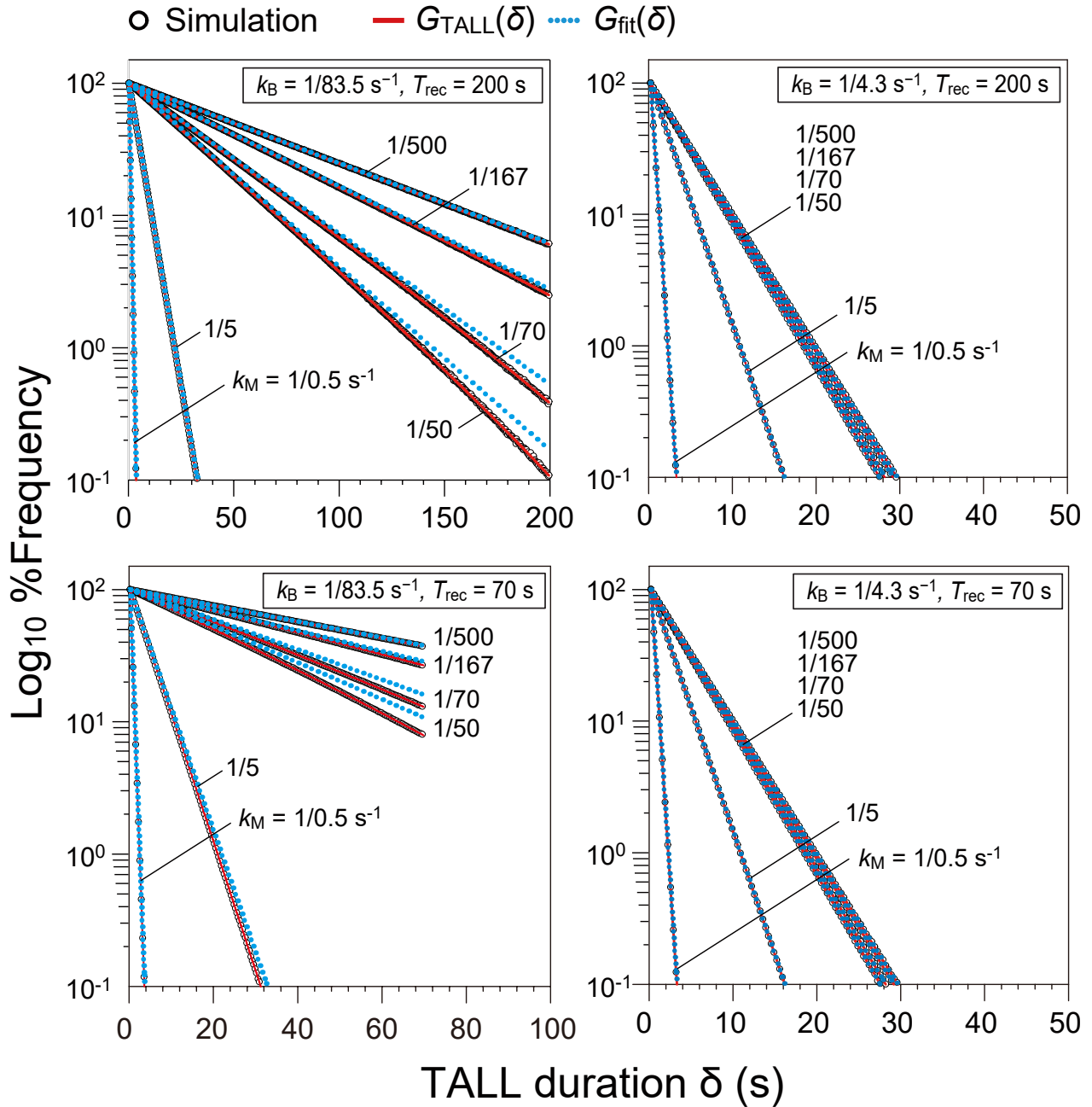
Supplementary Figure 39 | The distributions of TALL durations under four conditions of k_B (1/83.5 and 1/4.3 s^{-1}) x T_{rec} (200 and 70 s), obtained by Monte Carlo simulations of Brownian particles undergoing repeated TALL events and the best fit functions for the distributions using $G_{TALL}(\delta)$ (red curves) and $G_{fit}(\delta)$ (blue curves). The k_M values employed here were 1/0.5, 1/5, 1/50, 1/70, 1/167 and 1/500 s^{-1}. The box at the top left is the same as that in **Supplementary Fig. 38.**
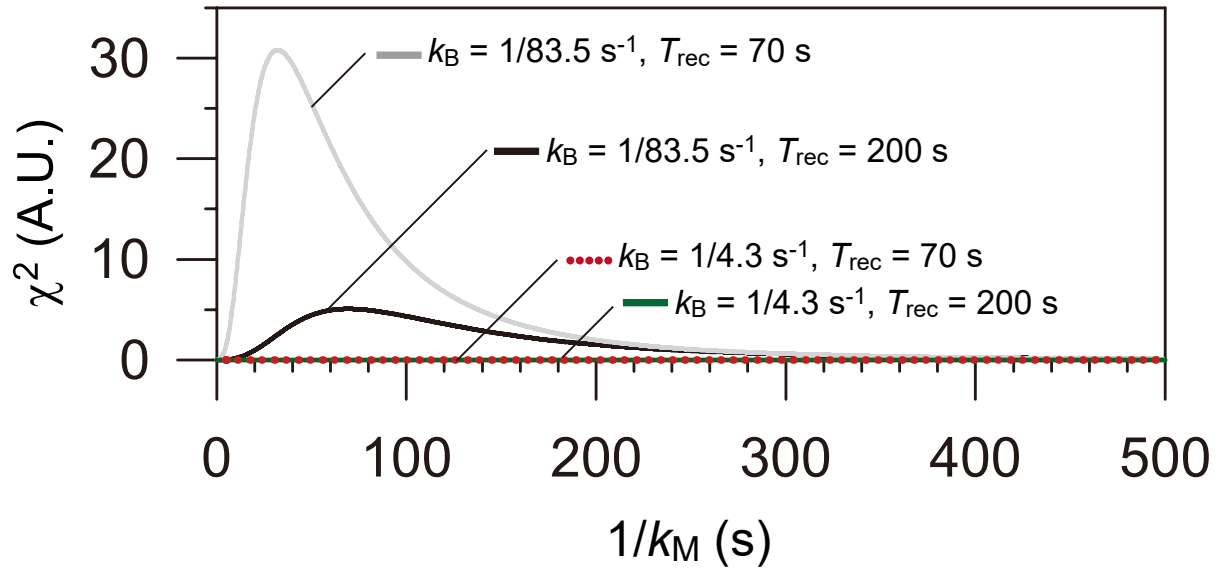
Supplementary Figure 40 | The difference between $G_{TALL}(\delta)$ and $G_{fit}(\delta)$ plotted against $1/k_M$, determined for the four conditions described in **Supplementary Fig. 39**. The difference was parameterized using χ^2, defined as

$$\chi^2(1/k_M) = \int_0^{t_{max}} \frac{[G_{all}(\delta) - G_{fit}(\delta)]^2}{G_{fit}(\delta)} \cdot d\delta$$

.
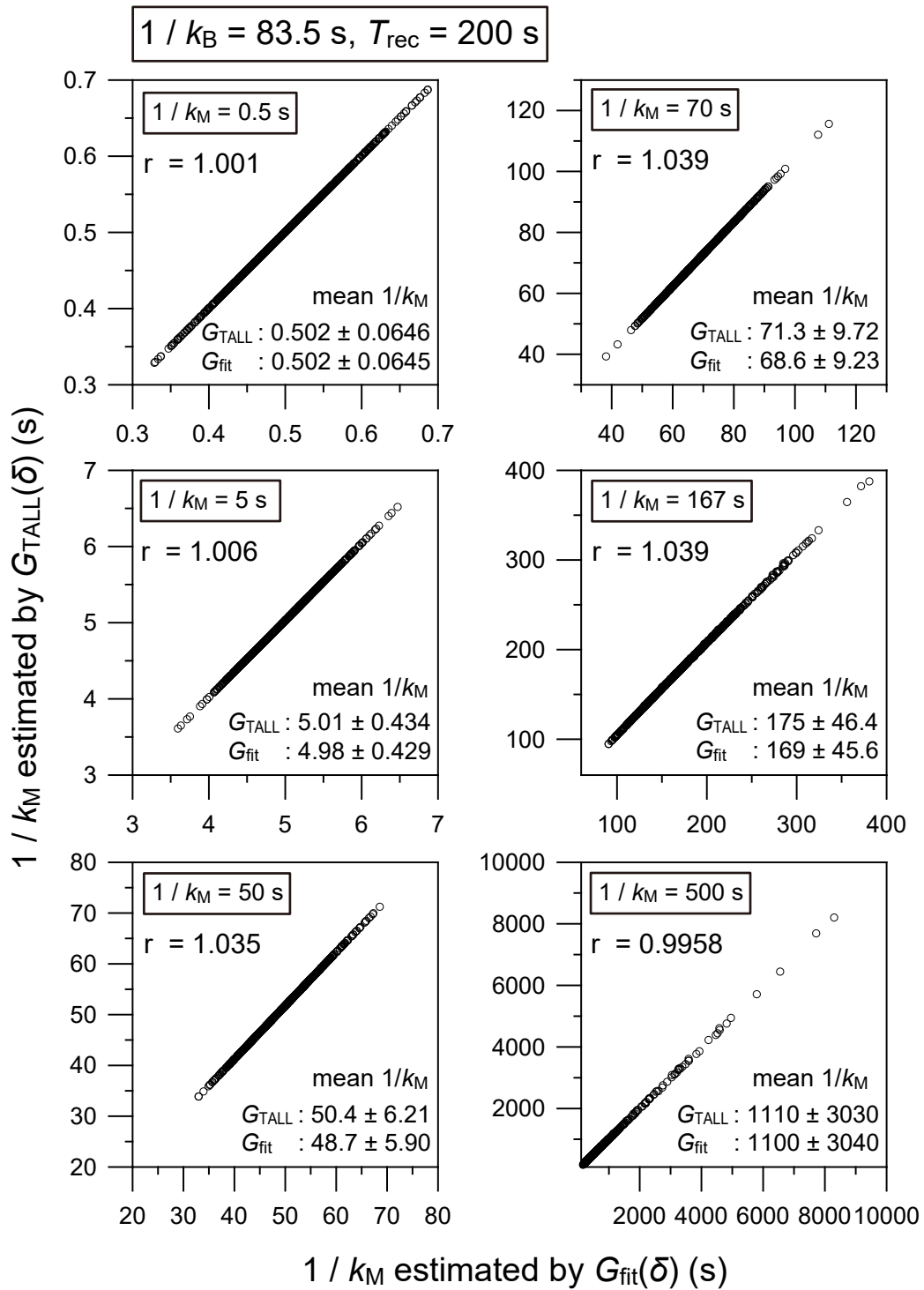
Supplementary Figure 41 | The correlation in the estimation of k_M between the cases where $G_{TALL}(\delta)$ and $G_{fit}(\delta)$ were used as fitting functions, for the histograms of TALL durations obtained by Monte Carlo simulations. The purpose of this examination is to determine whether $G_{fit}(\delta)$ can be used to replace $G_{TALL}(\delta)$ under practical experimental

conditions where only a limited number of TALL events can be examined. For this purpose, in this simulation, we generated only 500 TALL events (as compared to 10^8 events for the results shown in **Supplementary Figs. 38 and 39**) for each parameter set, and to obtain the distribution, this was repeated 1,000 times. See the text for further details. The k_M values obtained by the correct function $G_{TALL}(\delta)$ were plotted against the k_M values obtained by using the approximate function $G_{fit}(\delta)$ (therefore, each plot in a box shown above contains 1,000 spots). The parameters employed here were $k_B = 1/83.5$ and $T_{rec} = 200$ s, with six k_M values (1/0.5, 1/5, 1/50, 1/70, 1/167 and 1/500 s^{-1}).
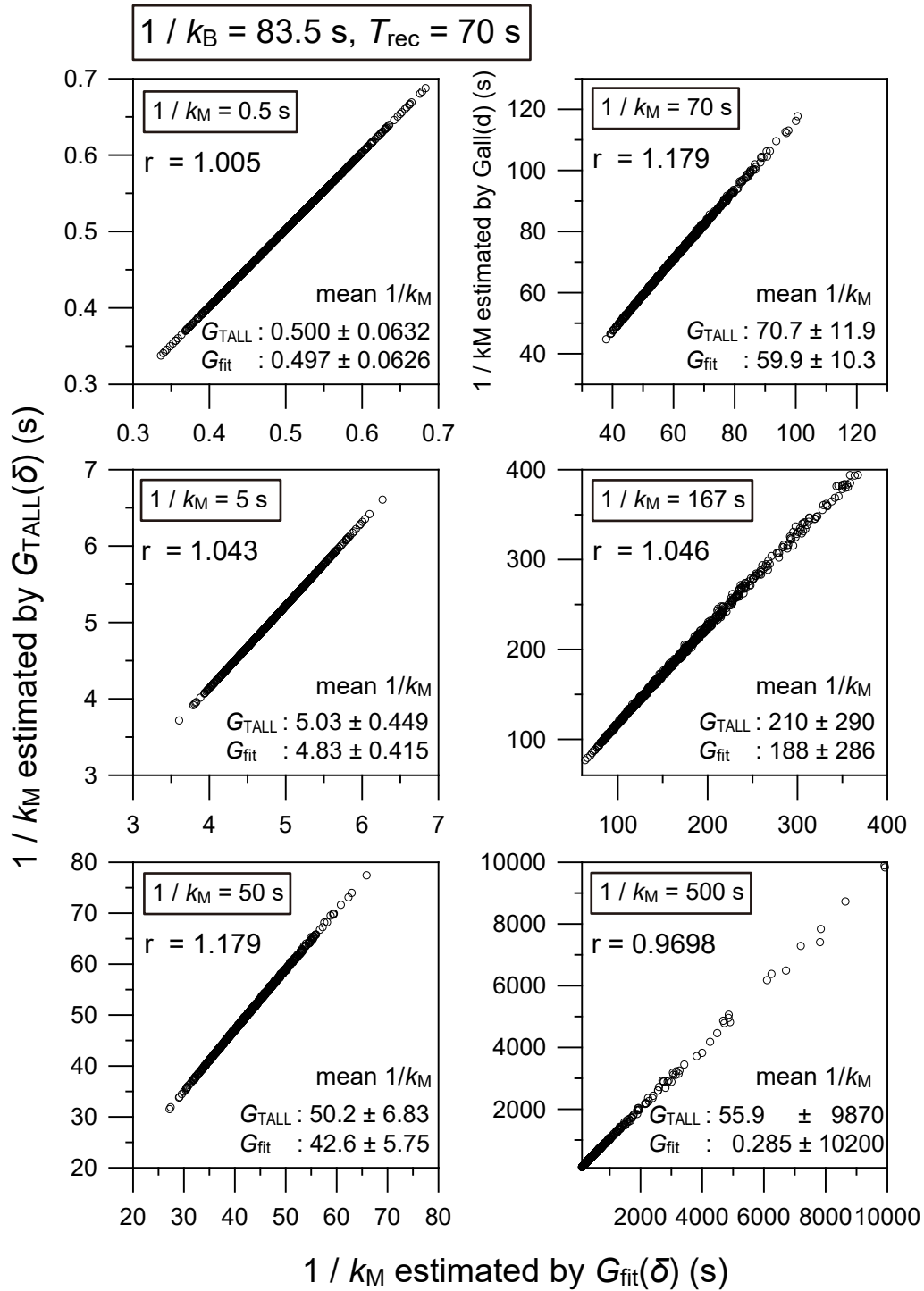
Supplementary Figure 42 | The same as **Supplementary Fig. 40**, but with a different pair of k_B and T_{rec} ($k_B = 1/83.5$ s^{-1} and $T_{rec} = 70$ s).
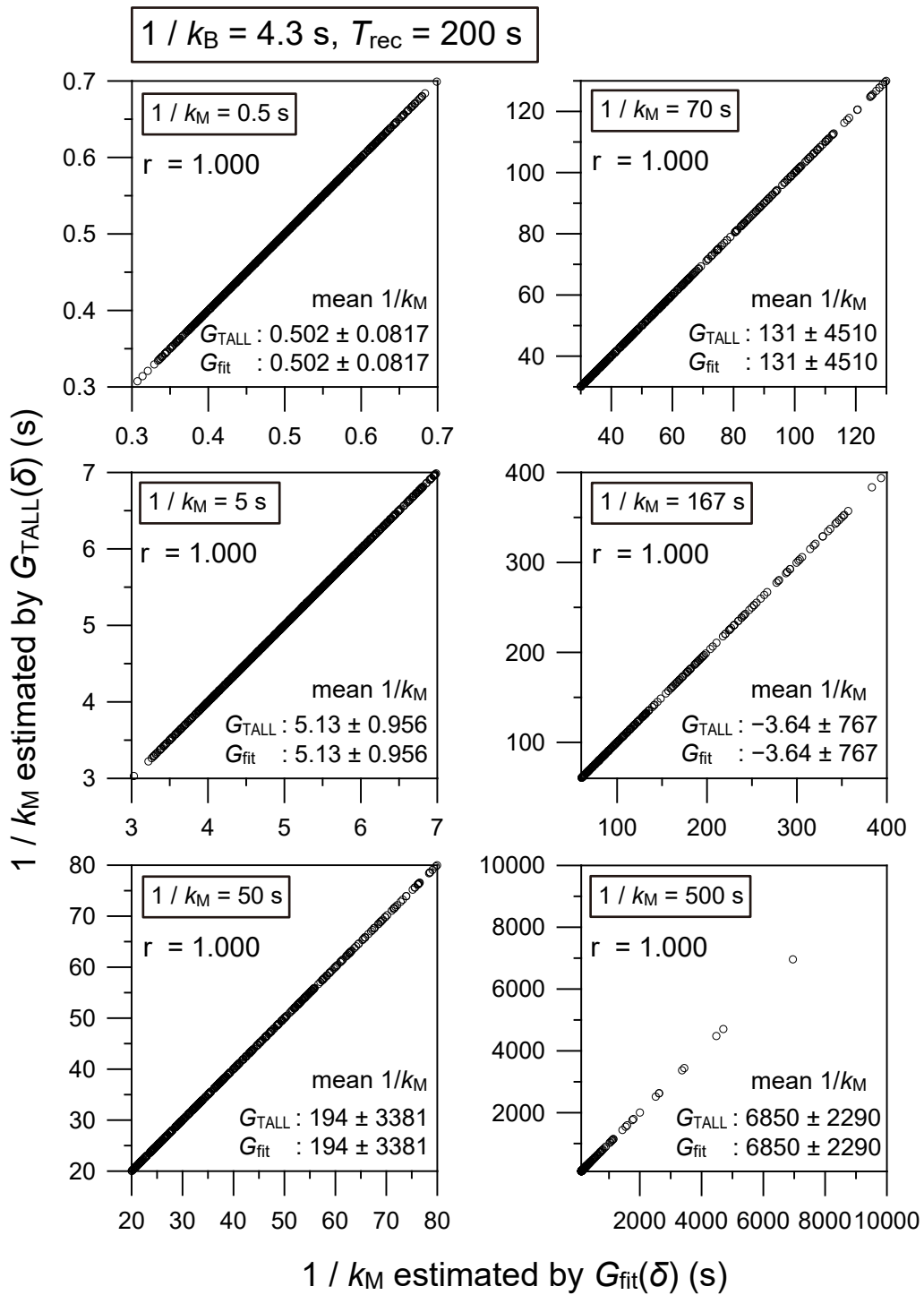
Supplementary Figure 43 | The same as **Supplementary Figs. 40 and 41**, but with a different pair of k_B and T_{rec} (k_B = 1/4.3 s^{-1} and T_{rec} = 200 s).
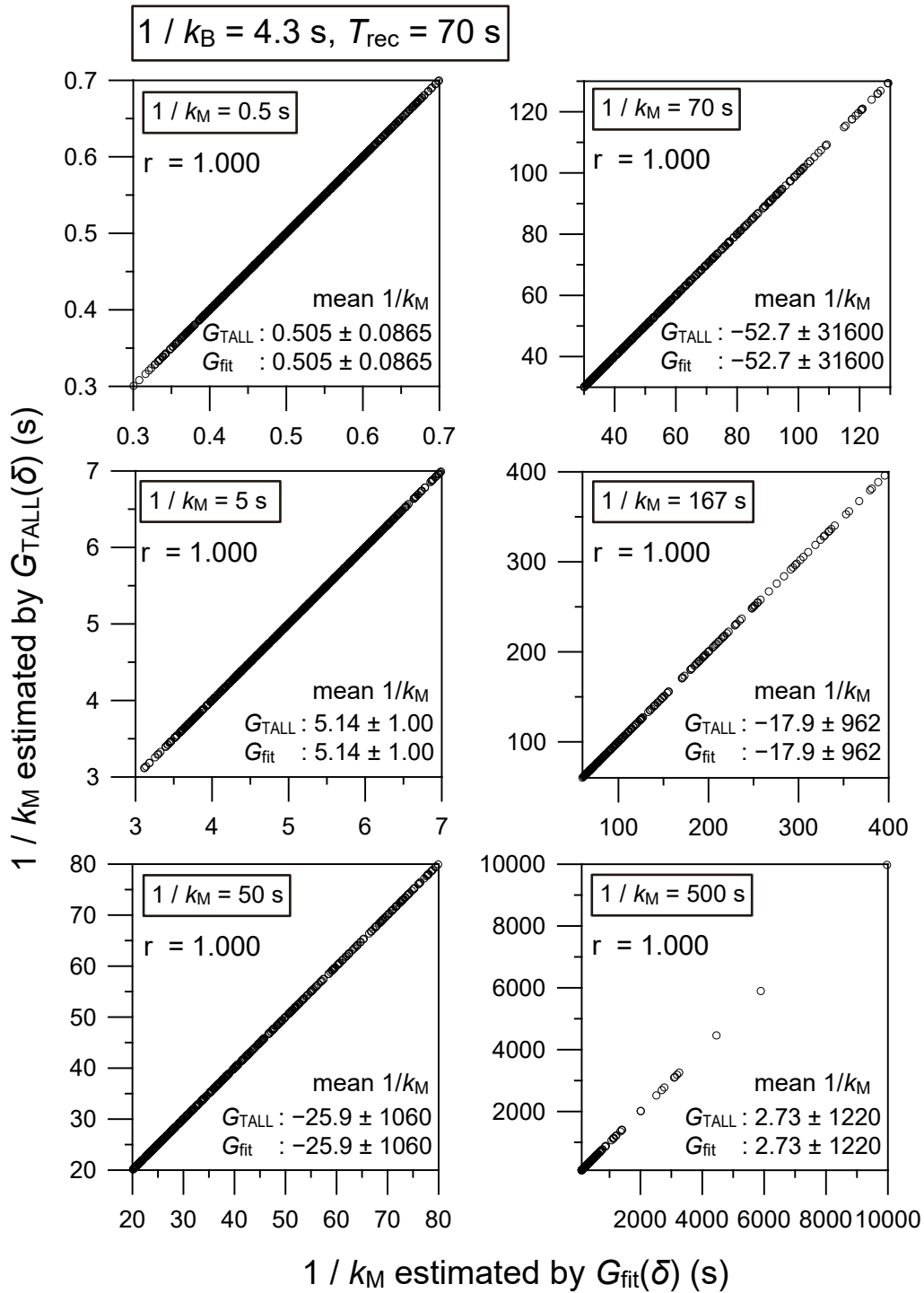
Supplementary Figure 44 | The same as **Supplementary Figs. 40-42**, but with a different pair of k_B and T_{rec} (k_B = 1/4.3 s^{-1} and T_{rec} = 70 s).

Supplementary Note 1 References

(Continued from Main Text, Methods and Supplementary Information)

83. Kasai, R. S. *et al.* Full characterization of GPCR monomer-dimer dynamic equilibrium by single molecule imaging. *J. Cell Biol.* **192,** 463–480 (2011).

Super-long single-molecule tracking reveals dynamic-anchorage-induced integrin function

Taka A. Tsunoyama, Yusuke Watanabe, Junri Goto, Kazuma Naito, Kenichi G.N. Suzuki, Takahiro K. Fujiwara and Akihiro Kusumi

— Supplementary Note 2 —
Synthetic procedures

TMR-, AT594-, AT647N- and ST647-CoA were synthesized by conjugating the maleimide derivatives of these dye compounds (Life Technologies, ATTO-TECH GmbH and SETA Biomedicals) with coenzymeA-SH (CoA-SH, New England Biolabs). Briefly, the maleimide derivatives of these fluorescent molecules were dissolved in *N,N*-dimethylformamide (DMF), followed by the addition of CoA-SH in a tris(hydroxymethyl)aminomethane (Tris)-buffered aqueous solution (pH 7.5), and then the reaction mixture was stirred at RT for 2 h. The Dye-CoA conjugates were purified by preparative reverse-phase high performance liquid chromatography (HPLC; LC-2010A HT/SPD-M20A, Shimadzu, with a Gemini-NX-5u 18C column for AT594- and AT647N-CoA and a Zorbax Eclipse XDB-C18 column for ST657- and TMR-CoA).

The NH$_2$-Halo ligand was synthesized from 2-(2-aminoethoxy)ethanol and 6-chloro-1-iodohexane, as described in **Ref. 65**. The AT594- and ST647-Halo ligands were synthesized by conjugating the NHS derivatives of these dye compounds (ATTO-TECH GmbH and SETA Biomedicals, respectively) with the NH$_2$-Halo ligand. These starting compounds were dissolved in dichloromethane (DCM), followed by the addition of triethylamine, and then the reaction mixture was stirred at RT overnight. The Dye-Halo ligand conjugates were purified by preparative reverse-phase HPLC, with a Phenomenex Gemini-NX-5u 18C column for the AT594-Halo ligand and a Phenomenex Kinetex C18 column for the ST647-Halo ligand.

For the syntheses of the Cy3- and Cy5-TX-Halo ligands (**Supplementary Figs. 17c, d and 45**), the method of Altman *et al.* was employed, with slight modifications[2,84]. Trolox was obtained from Sigma-Aldrich, and Cy3-bis-NHS and Cy5-bis-NHS were obtained from GE Healthcare. Briefly, compound **1** (trolox) was dissolved in DCM, followed by the addition of triethylamine (2.0 eq), ethylenediamine (10 eq), and BOP (1.5 eq), and then the reaction mixture was stirred at RT for 0.5 h. Compound **2** was obtained by silica gel column chromatography. To Compound **3** (Cy3-bis-NHS: n = 1, Cy5-bis-NHS: n = 2) dissolved in DCM, triethylamine (3.0 eq) was added, and to this mixture, compound **2** (0.8 eq) was slowly added, followed by an incubation with stirring at RT for 0.5 h to generate compound

4. Without purification, compound **5** (NH$_2$-Halo ligand, synthesized as described in a previous paragraph) was added, and the reaction mixture was further stirred at RT for 1 h to generate compound **6**, which was then purified by preparative reverse-phase HPLC with an Agilent Zorbax SB-C18 column (for Cy3-TX-Halo ligand) and a Phenomenex Kinetex5μ C18 column (for Cy5-TX-Halo ligand).

For the synthesis of AT594-TX-CoA (**Supplementary Figs. 17b and 46a**), first, compound **7** (trolox-NHS) was synthesized from compound **1** (trolox), following a previously published procedure[85]. Without purification, 9-fluorenylmethyloxycarbonyl (Fmoc)-Lys-OH (1.2 eq), DMF (2.2 eq), and *N,N*-diisopropylethylamine (DIPEA, 2.2 eq) were added, and then the reaction mixture was stirred at RT for 4 h. The resulting solution was diluted with ethylacetate, and then filtered. After concentration, compound **8** was purified by silica gel column chromatography (97% yield). Compound **8** (100 mg) and 33.4 mg *N*-(2-aminoethyl)maleimide hydrochloride (1.1 eq) were dissolved in prechilled dioxane (0˚C), followed by the addition of 32 μl DIPEA (1.1 eq) at 0˚C and then 38 mg of *N,N′*-dicyclohexylcarbodiimide (DCC, 1.1 eq) at 0˚C. The reaction mixture was stirred at RT overnight to generate compound **9**, which was then purified by silica gel column chromatography (final 59.3 mg, 99% yield). To compound **9** (59.3 mg) dissolved in DMF, 63 mg CoA-SH (1.0 eq) in 50 mM Tris (pH 7.5) was added, and the solution was stirred at RT for 4 h, and then the pH of the solution was adjusted to pH 8.0 by adding 1N NaOH. The resulting solution was further stirred at RT for 1 h, to generate compound **10**. Compound **10** was purified by preparative reverse-phase HPLC with an Agilent Zorbax SB-C18 column (80.6 mg, 66% yield). The Fmoc group of compound **10** was removed by dissolving 11.3 mg compound **10** in a water-DMF mixture (1:1 v/v), followed by the addition of 10 μl piperidine (15 eq) and an incubation at RT for 10 min. The solvent was then evaporated, and compound **11** was purified by preparative reverse-phase HPLC with an Agilent Zorbax SB-C18 column (9.5 mg, 99% yield). To 3.3 mg compound **11** dissolved in DMF, 3.6 mg AT594-NHS (1.0 eq) dissolved in DMF and 0.68 μl DIPEA (1.5 eq) were added, and then the reaction mixture was stirred at RT for 4 h, to generate compound **12**. Compound **12** was

purified by preparative reverse-phase HPLC with an Agilent Zorbax SB-C18 column (0.6 mg, 11% yield).
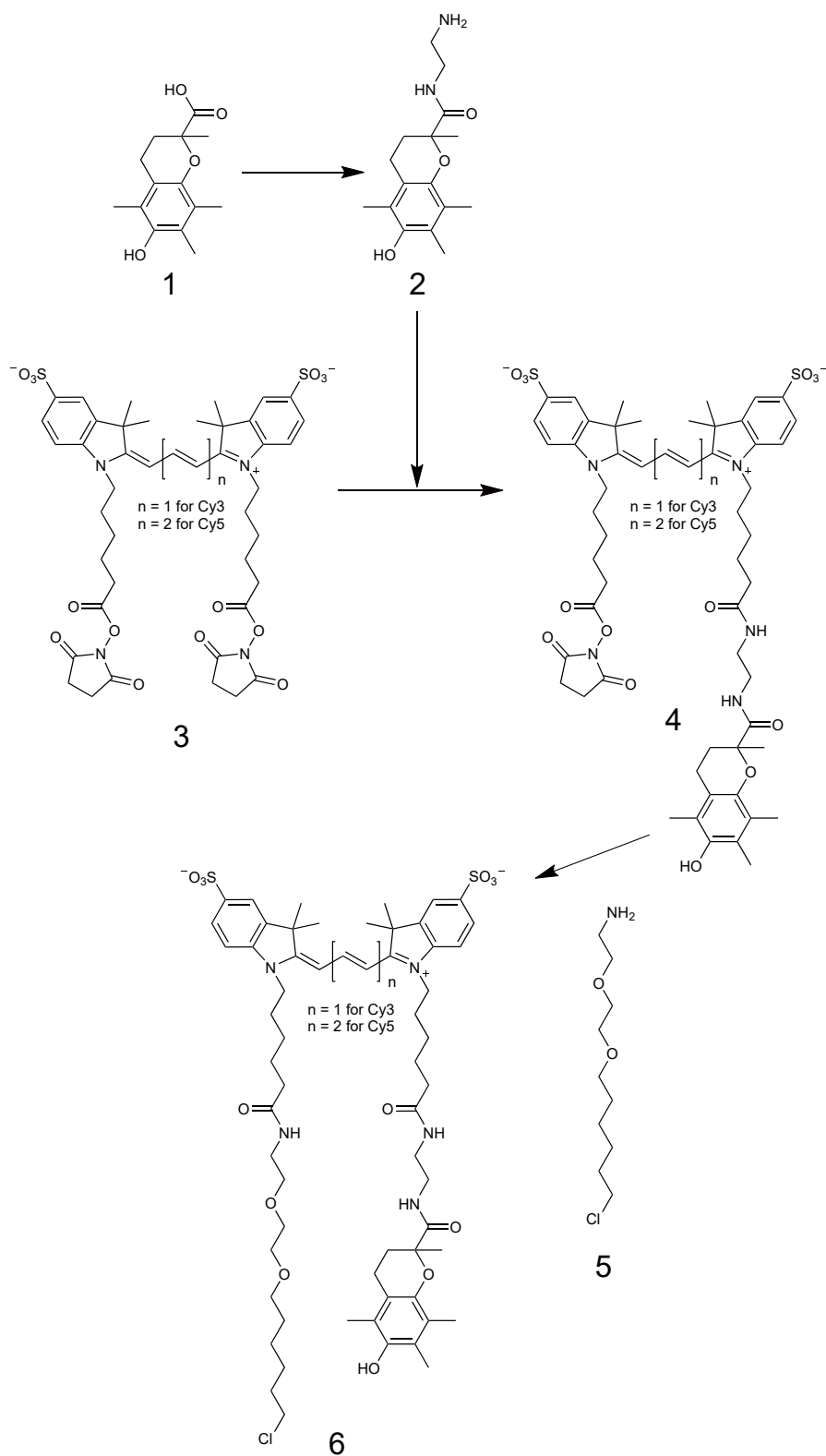
For the synthesis of the TMR-TX-Halo ligand (**Supplementary Figs. 17a and 46b**), 22.3 mg compound **5** and 29.3 mg compound **8** (1.0 eq) were dissolved in dioxane, and then 11 mg DCC (1.1 eq) and 9.4 µl DIPEA (1.1 eq) were added. The mixture was stirred at RT for 4 h to form compound **13**. Compound **13** was purified by silica gel column chromatography (10.7 mg, 27% yield). The Fmoc group of compound **13** was removed by dissolving 10.7 mg compound **13** in DMF, followed by the addition of 10 µl piperidine (1.2 eq) and an incubation with stirring at RT for 1 h. Compound **14** was purified by preparative reverse-phase HPLC with a Phenomenex Gemini NX column (2.6 mg, 33% yield), and then 2 mg TMR-NHS (1.2 eq) and 1.24 µl DIPEA (2.2 eq) were added. The reaction mixture was stirred at RT overnight, and then the generated compound **15** was purified by preparative reverse-phase HPLC with a Phenomenex Gemini NX column (2.9 mg, 90% yield).

The purities of the final compounds were 95.67, 99.54, 99.61, and 90.62 for TMR-, AT594-, AT647N- and ST647-CoAs; 99.77 and 99.56 for AT594- and ST647-Halo ligands; 99.65 and 99.98 for Cy3- and Cy5-TX-Halo ligands; and 99.05 and 99.53% for AT594-TX-CoA and TMR-TX-Halo ligands, respectively, as determined by liquid chromatography-mass spectrometry (LC-MS; LCMS-2010A EV, Shimadzu, **Supplementary Fig. 47**).

ACP-tagged CD47 and integrin wild-type and mutants expressed on the cell surface (ACP tag in the extracellular N-terminus) were covalently labeled with fluorescent dye compounds by incubating the cells with 50 nM dye-conjugated CoA and 2 µM ACP synthase (New England Biolabs), in complete growth medium (containing 10 mM $MgCl_2$ sufficient for activating the synthase) at 37°C for 15 min. The Halo7-tagged proteins expressed in the PM (both inside and outside the cell) were covalently conjugated by fluorescent organic molecules, by incubating the cells with 5 nM Halo ligands linked to TMR or AL488 in complete growth medium at 37°C for 15 min, or 5 nM R110-Halo ligand in complete growth medium at 37°C overnight. Under these conditions, 10~20% of the expressed proteins
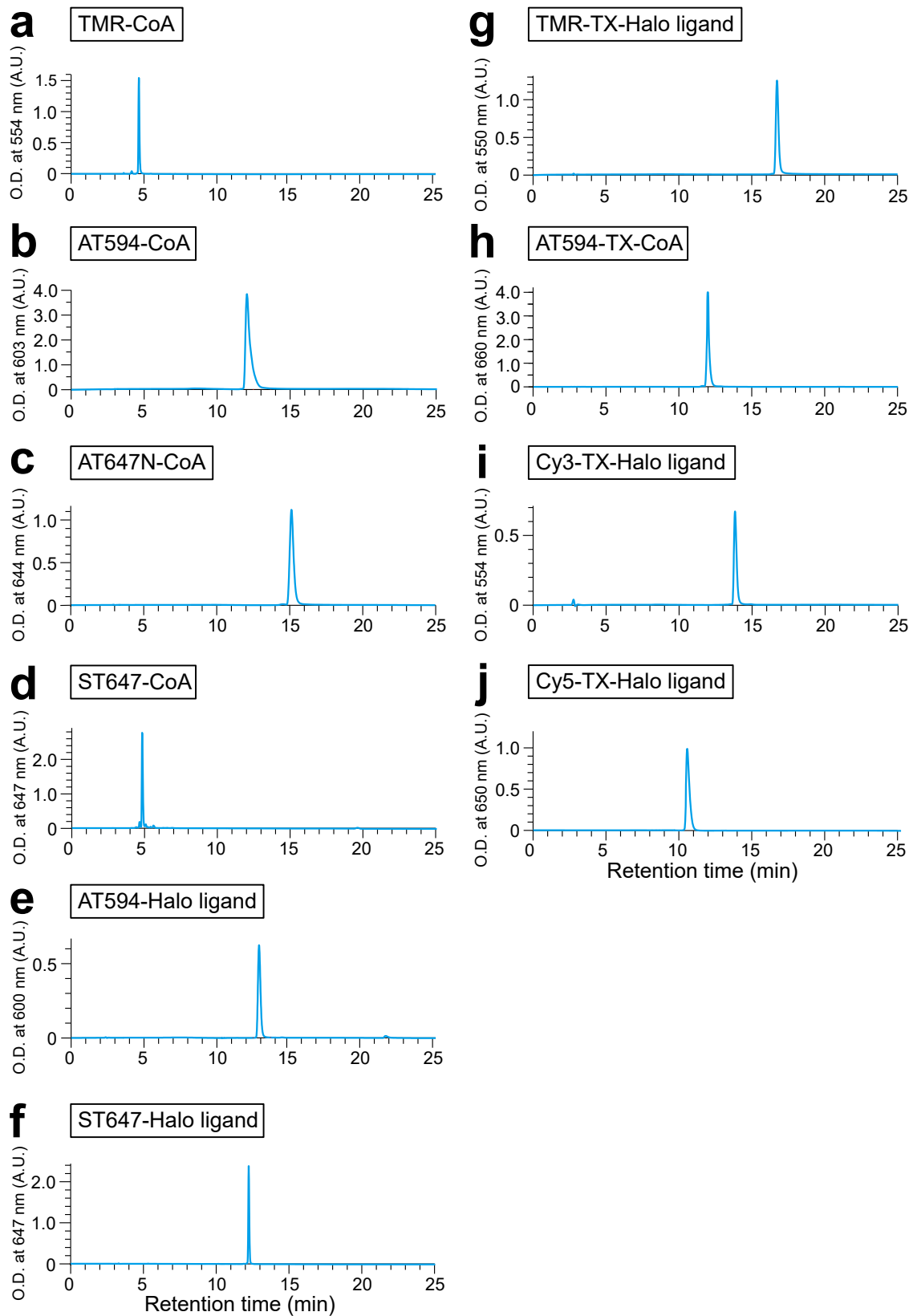
were fluorescently labeled.

Supplementary Note 2 Figures

Supplementary Figure 45 | The scheme for synthesizing the Cy3- and Cy5-TX-Halo ligands.
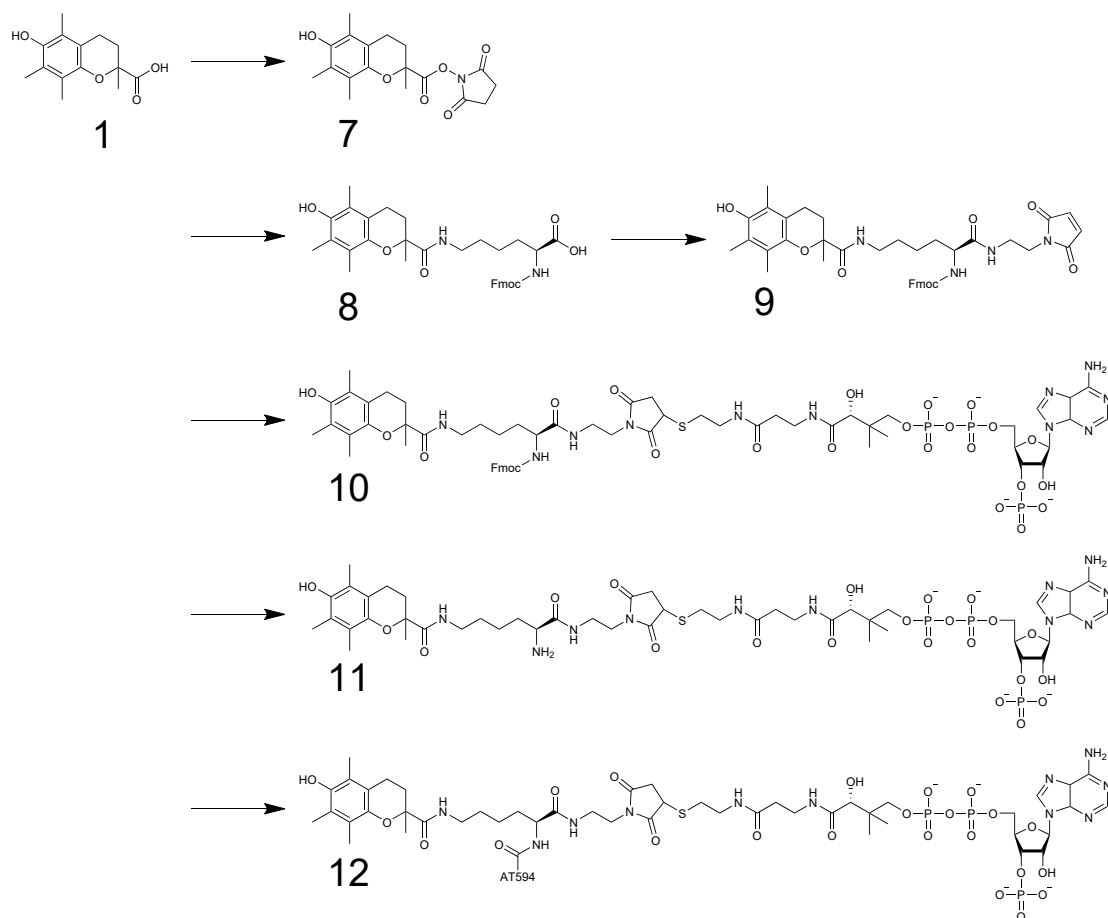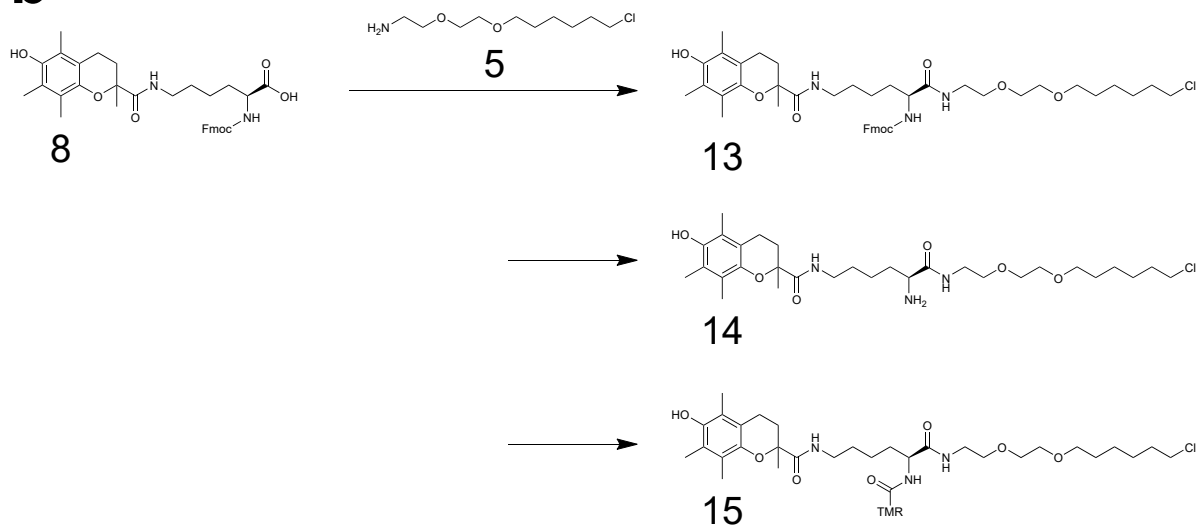
Supplementary Figure 46 | The schemes for synthesizing the AT594-TX-CoA (**a**) and TMR-TX-Halo (**b**) ligands.

Supplementary Figure 47 | LC-MS elution profiles of the final products synthesized in this study.

Supplementary Note 2 References

(Continued from Main Text, Methods, Supplementary Information, and Supplementary Note 1)

84. Fonge, H. *et al.* Necrosis avidity of (99m)Tc(CO)3-labeled pamoic acid derivatives: synthesis and preliminary biological evaluation in animal models of necrosis. *Bioconjug. Chem.* **18,** 1924–1934 (2007).

85. Koufaki, M. *et al.* Synthesis of chroman analogues of lipoic acid and evaluation of their activity against reperfusion arrhythmias. *Bioorg. Med. Chem.* **12,** 4835–4841 (2004).